

Πανεπιστήμιο Κρήτης
Σχολή Θετικών Επιστημών
Τμήμα Φυσικής

Μεταπτυχιακό πρόγραμμα «Μικροηλεκτρονικής - Οπτοηλεκτρονικής»

«*In vivo* απεικόνιση των δομικών χαρακτηριστικών και διεργασιών του
νηματώδους *C. elegans* με τη χρήση μη γραμμικής μικροσκοπίας
(TPEF, SHG, THG) »

Μερόπη Μαρή

Μεταπτυχιακή εργασία

Επιβλέπων: Καθ.Κ.Φωτάκης

Υπεύθυνος Εργασίας: Δρ.Γ.Φιλίπιδης

Ηράκλειο 2007

University of Crete
School of Natural and Technological Sciences
Physics Department

Postgraduate course in “Microelectronics – Optoelectronics”

“*In vivo* imaging of structural features and processes of *C. elegans* using
non-linear microscopy (TPEF, SHG, THG)”

Meropi Mari

Master Thesis

Supervisor: Prof. C. Fotakis

Advisor: Dr. G. Filippidis

Heraklion 2007

Chapter 6 Experimental results using scanning galvo-mirrors

6.1 Experimental apparatus.....	73
6.2 Experimental results.....	75
Posterior part.....	75
Anterior part.....	81

Chapter 7 In vivo monitoring of neuron degeneration

7.1 THG imaging microscopy measurements as a tool for the in vivo monitoring of neuron degeneration in C. elegans samples.	84
7.2 Experimental apparatus.....	88
7.3 Experimental results.....	89

<i>References</i>	97
--------------------------------	----

Acknowledgements – Πρόλογος

Η παρακάτω εργασία εκπονήθηκε στα πλαίσια του μεταπτυχιακού προγράμματος «Οπτοηλεκτρονική – Μικροηλεκτρονική» του Τμήματος Φυσικής του Πανεπιστημίου Κρήτης και είναι το αποτέλεσμα της συνεργασίας του μεταπτυχιακού προγράμματος του τμήματος Φυσικής και του Ινστιτούτου Ηλεκτρονικής Δομής και Λείζερ (ΙΗΔΛ - IESL) του Ιδρύματος Τεχνολογίας και Έρευνας (ΙΤΕ - FORTH) με διευθύνοντα τον Καθ.Κ.Φωτάκη. Αυτή η μεταπτυχιακή εργασία ολοκληρώθηκε μετά από προσπάθειες πολλών ενθουσιωδών ερευνητών.

Θα ήθελα αρχικά να ευχαριστήσω τον επιβλέποντα ερευνητή Δρ. Γιώργο Φιλιππίδη (υπεύθυνο της ομάδας Βιοϊατρικών Εφαρμογών του ΙΗΔΛ), ο οποίος ήταν ο τυπικά υπεύθυνος της πειραματικής διαδικασίας, για τη βοήθειά του στο σχεδιασμό και την οριοθέτηση των στόχων της εργασίας, για τη συνεχή καθοδήγηση και επίβλεψή του όλους αυτούς τους μήνες στο πειραματικό μέρος και την ανάλυση των αποτελεσμάτων, καθώς και για την ουσιαστική συνεισφορά στη διαμόρφωση του κειμένου.

Θα ήθελα να ευχαριστήσω τον Καθ.Κώστα Φωτάκη ο οποίος μου παρείχε τη δυνατότητα να εργαστώ σε ένα άρτιο ερευνητικό περιβάλλον και είχε τη γενικότερη επίβλεψη της εργασίας.

Ένα πολύ μεγάλο ευχαριστώ οφείλω στο Μεταδιδακτορικό ερευνητή Δρ.Emilio J.Gualda Manzano ο οποίος έπαιξε καθοριστικό ρόλο στην υλοποίηση της εργασίας μου. Επιμελήθηκε την προσαρμογή της πειραματικής διάταξης στα δεδομένα του ερευνητικού μας έργου και ταυτόχρονα μου παρείχε πολύ φιλικά όλη την προηγούμενη εμπειρία τόσο σε θεωρητικό όσο και σε τεχνολογικό επίπεδο εφαρμογής της. Χωρίς την πολύτιμη συνεισφορά του Emilio, λίγα από αυτά που παρουσιάζονται θα είχαν επιτευχθεί. Θα ήθελα να ευχαριστήσω τον κ. Χ. Κουλουμέντα καθώς και τον Σ.Ψιλοδημητρακόπουλο (πρώην μέλη της ομάδας Βιοϊατρικών Εφαρμογών του ΙΗΔΛ) των οποίων οι μεταπτυχιακές διατριβές μας παρείχαν τη βάση για το θεωρητικό κομμάτι αυτής της εργασίας καθώς και για ένα μέρος της ερμηνείας των αποτελεσμάτων.

Ένα μεγάλο ευχαριστώ οφείλω στον Δρ. Νεκτάριο Ταβερναράκη, ερευνητή Β' στο Ι.Μ.Β.Β. του Ι.Τ.Ε., για τη συνεισφορά στο συντονισμό της ερευνητικής προσπάθειας στα πλαίσια της οποίας εντάσσεται η παρούσα εργασία. Επιπλέον, θα ήθελα να

ευχαριστήσω ιδιαίτερα τον συνεργάτη του, υποψήφιο διδάκτορα Γιάννη Βόγλη, για τις πολύτιμες συμβουλές και διευκρινήσεις του, και για την βοήθεια που μας παρείχε στην επεξήγηση εννοιών και προβλημάτων της βιολογίας, καθώς και τον προπτυχικό φοιτητή Μανόλη Βλάχο για την προετοιμασία των βιολογικών δειγμάτων.

Τέλος, το πιο γλυκό ευχαριστώ θα ήθελα να πώ σε όλους τους ανθρώπους του meeting room, που έκαναν τόσο ευχάριστο το περιβάλλον εργασίας και ιδιαίτερα στην Gabriella Kecskemeti για την ηθική υποστήριξη και στην Αρετή Μούρκα που με τις μουσικές της επιλογές έκανε πιο ευχάριστη την ατμόσφαιρα και στο εργαστήριο.

Σας Ευχαριστώ όλους

Περίληψη

Ο Διφωτονικά Διεγείρομενος Φθορισμός η Παραγωγή Δεύτερης και Τρίτης Αρμονικής είναι νέα σχετικώς εργαλεία για την απεικόνιση σε μικροσκοπικό επίπεδο βιολογικών δομών και διαδικασιών. Ο συνδυασμός τους σε ένα κοινό απεικονιστικό σύστημα είναι δυνατόν να προσφέρει μοναδικές και το σπουδαιότερο, συμπληρωματικές πληροφορίες σχετικά με τη δομή τη μορφολογία και τη λειτουργία ιστών, αλλά και μεμονωμένων κυττάρων. Στα πλαίσια της παρούσας εργασίας αναπτύχθηκε μία εύχρηστη, αξιόπιστη, συμπαγής πειραματική διάταξη για την ταυτόχρονη *in vivo* απεικόνιση βιολογικών δειγμάτων, με χρήση των μη γραμμικών φαινομένων του Διφωτονικά Διεγείρομενου Φθορισμού και της Παραγωγής Δεύτερης και Τρίτης Αρμονικής. Χρησιμοποιώντας αυτήν τη διάταξη, εξήχθησαν πολύτιμες πληροφορίες σχετικά με τη δομή και τη λειτουργία των ιστών και των κυττάρων του νηματοειδούς *C. elegans*.

Μέσω της πειραματικής διάταξης που αναπτύξαμε, έγινε δυνατή η απεικόνιση του μπροστινού και του οπίσθιου μέρους του *C. elegans* με μεγάλη διακριτική ικανότητα (~200nm). Χρησιμοποιήθηκε ένας μεγάλος αριθμός βιολογικών δειγμάτων. Wild type, γενετικά μεταλλαγμένα που εκφράζουν *Green Fluorescent Protein (GFP)* (είτε στη μεμβράνη, ή στο κυτταρόπλασμα) στους νεύρωνες, γενετικά μεταλλαγμένα που εκφράζουν *GFP* στο κυτταρόπλασμα του φάρυγγα και *DsRed* στο κεφάλι και στους νεύρωνες. Επιπλέον, καθορίστηκαν οι βέλτιστες πειραματικές συνθήκες για την *in vivo* ανίχνευση σήματος Παραγωγής Τρίτης Αρμονικής από το *C. elegans*, το οποίο δίνει πολύτιμες πληροφορίες για τα ανατομικά και μορφολογικά χαρακτηριστικά και τις εσωτερικές δομές του νηματοειδούς. Αξίζει να σημειωθεί ότι είναι η

πρώτη φορά που επιτεύχθηκε η καταγραφή σήματος Παραγωγής Τρίτης Αρμονικής από το *C. elegans*.

Με τη βοήθεια των μετρήσεων Παραγωγής Τρίτης Αρμονικής, έγινε εφικτή η απεικόνιση εκφυλισμένων νευρώνων. Μέσω αυτών των μετρήσεων πραγματοποιήθηκε ο ακριβής *in vivo* προσδιορισμός του σχήματος και των δομικών χαρακτηριστικών των εκφυλισμένων νευρώνων στο οπίσθιο μέρος του νηματοειδούς καθώς και η απεικόνιση της εξέλιξης των εκφυλισμένων νευρώνων σε πραγματικό χρόνο.

Η ανάπτυξη της απεικονιστικής πειραματικής διάταξης για την *in vivo* καταγραφή τριών διαφορετικών μη γραμμικών σημάτων από βιολογικά δείγματα αποδεικνύεται ιδιαίτερα χρήσιμη για μια σειρά εφαρμογών στο πεδίο της βιολογίας και της ιατρικής. Προσφέρει νέες προοπτικές στην έρευνα εμβρυικών μορφολογικών αλλαγών καθώς και πολύπλοκων αναπτυξιακών διαδικασιών. Η τρισδιάστατη ανάλυση, επιτρέπει τη σύλληψη οπτικών πληροφοριών σχετικά με τις αναπτυξιακές διαδικασίες σε κυτταρικό ή υποκυτταρικό επίπεδο που συμβαίνουν σε ζωντανά έμβρυα. Τέλος, οι μετρήσεις Παραγωγής Τρίτης Αρμονικής αποδίδουν μοναδικές, υψηλής διακριτικής ικανότητας, μορφολογικές πληροφορίες και παρέχουν μία ποιοτική περιγραφή της δυναμικής εσωτερικών δομών σε wild type και μεταλλαγμένα (mutants) έμβρυα ή μοντέλα οργανισμούς.

Abstract

Two Photon Fluorescence (TPEF), Second Harmonic Generation (SHG) and Third Harmonic Generation (THG) are relatively new imaging tools for the imaging of biological structures and processes at the microscopic level. The combination of TPEF, SHG, and THG imaging contrast modes in a single instrument provides unique and complementary information concerning the structure and the function of tissues and individual cells. In the present study, a useful, reliable, compact set-up for the *in vivo* simultaneous TPEF, SHG and THG imaging of biological samples, was developed.

By means of the developed setup, high-resolution (~200nm) mapping of the nematode *C. elegans* in both its anterior and posterior body part was achieved. Unique information related the structure and the functions of tissues and cells of the nematode were extracted. Numerous strains were investigated. Wild type, mutants expressing GFP (membrane localized or cytoplasmic) in mechanoreceptor neurons, mutants expressing diffuse GFP in the pharyngeal cytoplasm and expressing diffuse DSRED in the head and motor neurons. Optimum conditions for the detection of THG signal, arising from the worm, were found. Detailed and specific structural and anatomical features can be visualized, by recording THG signals. This is the first time that a THG modality is employed to image live *C. elegans* specimens.

Additionally, by performing THG measurements, neurodegeneration phenomena were investigated. The *in vivo* precise identification of the shape and the contour of the degenerative neurons in the posterior part of the nematode and the monitor, in real time, of the evolution of the degenerative neurons of the worm through THG imaging measurements were achieved.

The development and optimization of a user friendly and compact prototype microscope system that combines three different nonlinear image-contrast modes (TPEF-SHG-THG) in a single instrument will be useful for a variety of applications in the field of biology and medicine. It offers new insights into the studies of embryonic morphological changes and complex developmental processes. The excellent 3D resolution capacity of these non linear techniques allows us to capture the subtle developmental information on the cellular or subcellular levels occurring deep inside the live larvae. Moreover, THG imaging measurements provide a quantitative description of the dynamics of internal structures in unstained wild type and mutant embryos and model organisms.

Introduction

The visualization of internal structures and the monitoring of processes in biological specimens are essential for the advancement of biomedical sciences. Within the field of microscopy there is the need for imaging complicated structures with higher contrast and higher 2D and 3D spatial and temporal sensitivity and spectral analysis. This need has been addressed by the use of laser scanning confocal microscopy (CM). CM has been very successful due to its reliability, robustness and its ability for imaging living specimens. However, in addition to being expensive, confocal microscopes are unsuited for imaging fast cellular processes. In any case, they can offer only some of the capabilities possible offered by the nonlinear spectroscopy.

The use of femtosecond (*fs*) lasers as excitation sources has improved not only the resolution and 3D imaging capabilities of microscopy by multiphoton excitation – e.g., Two- or Three Photon Excitation Fluorescence (TPEF) - but has also demonstrated the possibilities for new detection techniques by exploiting non-linear excitation effects, e.g. Second-Harmonic Generation (SHG) and Third Harmonic Generation (THG). The basic principle underlying these techniques is that for tightly focused *fs* laser pulses, the photon density is high enough to induce multiphoton absorption or other nonlinear (coherent) processes within the focal volume. Fluorophores whose excitation maximum is in the UV or in the VIS can be excited by two or three infrared photons. Since nonlinear absorption and thus induced fluorescence occurs solely at the focal volume of the laser beam, a high axial resolution and consequently the 3-D imaging capability of confocal microscopy can be attained without the use of a confocal aperture. Furthermore, there is no interfering fluorescence from the surrounding structures and “out of focal plane” photobleaching and phototoxicity can be significantly reduced. More precisely, for nonlinear techniques, the efficiency of the generated signal scales nonlinearly with the intensity of the excitation beam. Thus, the use of *fs* lasers enables high peak powers for efficient nonlinear excitation, but at low enough energies so that biological specimens are not damaged. Additionally, the use of infrared light implicates a high penetration depth into tissues due to the

low absorption of the primary cellular components (water, proteins etc). For SHG and THG, an additional advantage derives from the fact that no energy is deposited (absorbed) by specimens, thus sample disturbance (e.g., thermal, mechanical side-effects) are minimal. The 3-D fluorescence imaging based on nonlinear fluorophore excitation enables a number of applications in life science, such as high-resolution imaging of biological activities in living cells and tissues, studying cell motility and the distribution of a neurotransmitter in living cells.

In addition, the systems available at present are specialized to a single non linear detection method (e.g TPEF imaging measurements), whereas the complexity of the biological problems requires the parallel or successive application of more than one spectroscopic techniques. For instance, the combination of different image-contrast modalities (such of TPEF-SHG-THG) in a single instrument has the potential to provide unique and complementary information about the structure and function of tissues, individual cells and organelles of live biological specimens.

Within the framework of this project the development and the optimization of a user friendly and compact prototype microscope system that combines different nonlinear image-contrast modes in a single instrument for biological applications was achieved. Consummative and specific information about the anatomy and the functions of the nematode *Caenorhabditis elegans* was collected by implementing a combination of THG, SHG and TPEF image contrast modalities. Moreover, the potential of Third Harmonic Generation (THG) measurements to image specific cellular and anatomical features (such as neuronal degeneration) of the nematode *in vivo* was investigated. We found that THG is a powerful tool for probing structural and anatomical changes of biological samples and processes at the microscopic level.

1.1 Fluorescence

Fluorescence is only one of the possible mechanisms by which an excited molecule can undergo to the ground state. The Jablonski diagram in **Figure 1.1** shows that there are a number of potential transitions open to the S_1 state after being populated by excitation and internal conversion from upper states. Before we describe these potential transitions, we briefly discuss the process of internal conversion. The energy separation between consecutive singlet levels (S_0, S_1, \dots, S_n) tends to decrease with increasing electronic energy. Nonradiative transitions between upper states (S_n to S_{n-1}) occur rapidly to populate the lowest excited state, S_1 . These types of transitions are denoted *internal conversion* as they occur between states of the same spin multiplicity. For this reason, the fluorescence emission spectrum is typically independent of the excitation

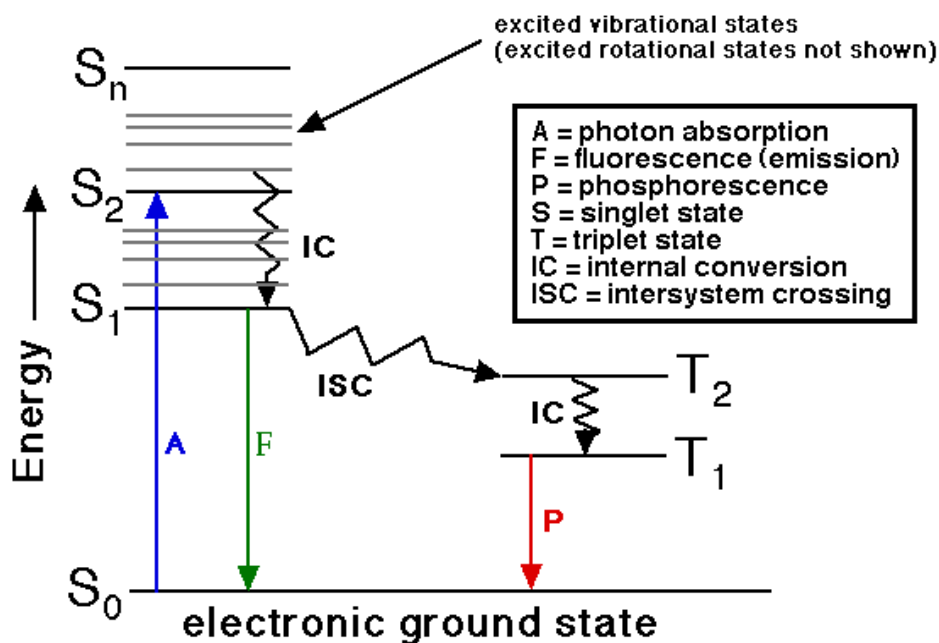


Figure 1.1: Modified Jablonski diagram showing radiative and nonradiative transitions between the ground state (S_0) and excited singlet (S_1, S_2) and triplet (T_1) states.

wavelength. According to the Jablonski diagram, now, the excited molecule can undergo both nonradiative and radiative (fluorescence) relaxation to the ground state (S_0) or nonradiative transition (*intersystem crossing*) to the lowest excited triplet state (T_1).

Intersystem crossing is defined as a nonradiative transition between states of different multiplicity (e.g. singlet-triplet) and results via inversion of the spin of the excited electron. Although intersystem crossing is formally forbidden due to selection rules, spin-orbit and vibronic coupling mechanisms makes it possible, but in any case less probable than fluorescence. Direct absorption into the triplet state from the ground state is spin forbidden, but the triplet excited state can be accessed indirectly through intersystem crossing from S_1 to T_1 state. The opposite transition from the excited triplet to the ground singlet is called phosphorescence and is also spin forbidden, hence it occurs very slowly with a radiative lifetime in the order of seconds or longer. By contrast, fluorescence lifetimes are of the order of nanoseconds. Phosphorescence can be observed only when the other de-activating processes have been suppressed, typically in rigid glasses, at low temperature and in the absence of oxygen.

Box 1: Useful magnitudes and basic relations.

According to the Beer-Lambert law the *molecular single photon absorption cross-section* σ_1 (cm^2) is given as:

$$\sigma_1 = \frac{\ln\left(\frac{I}{I_{out}}\right)}{nd} \quad (1.1)$$

where I the light intensity entering the sample, I_{out} the light intensity leaving it, n the number of molecules per volume (cm^{-3}), and d the sample pathlength (cm). The cross-section σ_1 is related with the single-photon absorption rate (W_1) through the relationship (I expressed as: *photons / sec·cm²*):

$$W_1 = \sigma_1 I \quad (1.2)$$

The *quantum yield of fluorescence* Φ_f is defined as:

$$\Phi_f = \frac{\text{number of fluorescence emitted photons}}{\text{number of absorbed photons}} \quad (1.3)$$

The quantum yield of fluorescence can also be defined in terms of rate constants by:

$$\Phi_f = \frac{k_r}{\sum k} \quad (1.4)$$

where k_r is the radiative rate constant and $\sum k$ is the sum of the rate constants for all processes that depopulate the S_1 state.

The radiative lifetime, τ_r is defined by:

$$\tau_r = \frac{1}{k_r} \quad (1.5)$$

while the observed fluorescence lifetime τ_f by:

$$\tau_f = \frac{1}{k_f} = \frac{1}{\sum k} \quad (1.6)$$

Only in the unlikely absence of any competing deactivation channels, would τ_r be identical to τ_f .

1.2 Two Photon Absorption

The process of absorption, in its simplest form, enables the absorption of a single photon from the molecule in the ground state in order to promote an electron to a higher energy molecular orbital. Apart from this simple form of absorption, quite more complicated exist, enabling more photons with lower energy. Absorption in these cases involves interaction of the molecule in the ground state with more photons to promote again an electron to a higher energy molecular orbital. The transition to the final excited state may involve the participation of intermediate real excited states, and then it is referred to as “*Multiple-Photon Absorption*”. The total transition is a multi-step process, and each step involves the independent absorption of a single photon, thus it is a resonant absorption. The molecule absorbs a photon, populates an excited state, and before the transition (radiative or nonradiative) to the ground state occurs, the molecule absorbs a second photon populating a higher excited state, and so on.

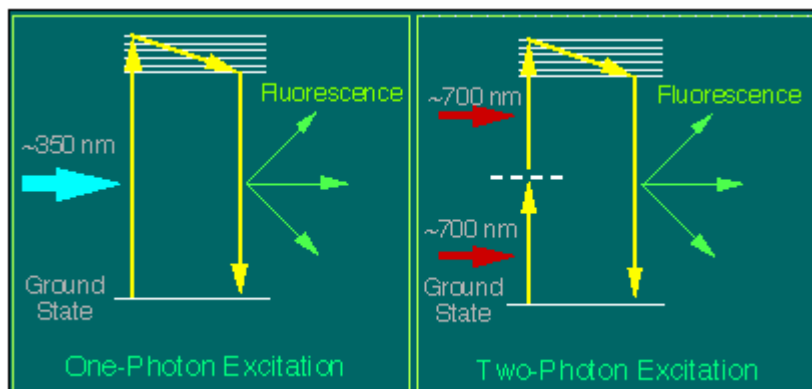


Figure 1.2: Potential energy diagram showing two-photon absorption through a virtual state. The molecule populates the first excited state, and undergoes normally to the ground state as in the case of the single-photon absorption.

On the other hand, the transition from the ground to the final state may involve the participation of intermediate virtual states, if the absorption of a single photon is not resonant, i.e. if the energy of the absorbed photon does not coincide

with the energy difference of two energy states. The total transition includes a series of virtual transitions, each occurring with a violation of energy conservation, and then it is referred to as “*Multi-Photon Absorption*”. The case of special interest for biophysical studies and for this work specifically is when the final state of the transition is the first excited state S_1 . In this case there are clearly no intermediate real states, and the absorption involving more photons and resulting in this transition is without question a multi-photon absorption. In **Figure 1.2**, the Jablonski diagram of two-photon excitation is depicted. The total transition of the molecule to the first excited state is realized via the absorption of two photons and involves the participation of one virtual state. Three-photon absorption would be realized via the absorption of three photons, and two virtual states would be involved. However, in the work presented here, two-photon absorption is used, and the generalization to the multi-photon case is made only for the best understanding of the two-photon absorption process.

In a virtual transition, the lifetime of the electron in the intermediate state τ_v is determined not by conventional relaxation mechanisms, but rather by the uncertainty principle connecting time and energy, $\Delta E \cdot \Delta \tau \sim \hbar$. The uncertainty in the energy of the virtual state can be taken as the detuning Δ from the nearest allowed resonance, $\Delta = \hbar(\omega_{10} - \omega)$, where $\hbar\omega_{10}$ is the energy difference between the ground and the state S_1 . For a typical detuning of 1 eV, the lifetime of the virtual state is expected to be about 0.5 fs. As the detuning from resonance Δ , approaches the natural width of the state Γ , virtual transitions become real transitions. In order for the electron to be able to be promoted from a virtual intermediate state to one of higher energy, the next photon (the second, in two-photon absorption) must be absorbed within the very short lifetime of the virtual

state. Therefore, such a process requires a very large photon density, and is observed only at very high light intensity.

The concept of multi-photon excitation, proceeding as a series of single-photon transitions through virtual states can be used to provide order of magnitude estimates of the N-photon cross-section. In **Box 2** the derivation of the “Two-photon absorption cross-section”, σ_2 is presented [1].

BOX 2: Derivation of the “Two-photon absorption cross-section”

The single photon absorption rate is given by:

$$W_1 = \sigma_1 I \quad (1.7)$$

For a resonant transition, the single photon absorption cross-section is of the order of 10^{-17} cm^2 for many molecules of biological interest. A second photon can be absorbed from a single molecule, only if it is incident within the lifetime of the state. The lifetime of a virtual state, τ_v is determined by the detuning of the state. Therefore, τ_v is of the order of the photon period:

$$\tau_v \sim \frac{2\pi}{\omega} \quad (1.8)$$

which is of the order of 1 fs. The rate of absorption out of the virtual state is again $W_1 = \sigma_1 I$, so that the combined rate for the absorption of two-photons W_2 , is given by:

$$W_2 \sim \sigma_1 I \frac{2\pi}{\omega} \sigma_1 I \quad (1.9)$$

Thus, defining a two-photon absorption cross-section, σ_2 ($\text{cm}^4 \cdot \text{sec} / \text{photon} \cdot \text{molecule}$) such that:

$$W_2 = \frac{1}{2} \sigma_2 I^2 \quad (1.10)$$

and combining eq. (1.9) and (1.10) the following estimation is obtained:

$$\sigma_2 \sim \frac{4\pi}{\omega} \sigma_1^2 \sim 10^{-49} \text{ cm}^4 \cdot \text{sec} / \text{photon} \cdot \text{molecule} \quad (1.11)$$

The value obtained from this crude estimation is in rather good agreement with both theoretical and experimental data, since for common chromophores with excitation wavelength ranging from 690 nm to 1050 nm, σ_2 is about 10^{-48} to $10^{-50} \text{ cm}^4 \cdot \text{sec} / \text{photon} \cdot \text{molecule}$ [2].

In the introduction, it was already mentioned that two-photon absorption, as well as second-harmonic generation (SHG) is a nonlinear phenomenon. Two photon absorption is related with the third-order susceptibility tensor $\chi^{(3)}$ of the nonlinear medium. In **Box 3** a series of calculations relating the two-photon absorption cross-section, σ_2 , with the term $\chi^{(3)}$, is presented [3].

BOX 3: Relating σ_2 to $\chi^{(3)}$

Suppose that an optical field with real amplitude E and a single frequency ω is incident to a nonlinear material. Macroscopically, the optical response of the material to the incident light, or generally electromagnetic radiation, is characterized by the optically induced polarization density, P , which can also be expanded in a Taylor's series about $E = 0$:

$$P = \chi^{(1)} * E + \chi^{(2)} * E * E + \chi^{(3)} * E * E * E + \dots \quad (1.12)$$

Eq. (1.12) can be rewritten as:

$$P = \chi * E \quad (1.13)$$

$$\text{where } \chi = \chi^{(1)} + \chi^{(2)} * E + \chi^{(3)} * E * E + \dots$$

The tensor χ is referred to as the susceptibility tensor. The index of refraction n is related with χ as:

$$n^2 = \frac{k^2 c^2}{\omega^2} = 1 + 4\pi\chi \quad (1.14)$$

Using the definition $n^2 = \varepsilon = \eta + i\kappa$, where ε is the complex dielectric constant, allows the real and imaginary parts of the refraction index to be expressed in terms of the real and imaginary parts of χ . Thus:

$$\eta^2 - \kappa^2 = 1 + 4\pi \operatorname{Re}\{\chi^{(1)} + \chi^{(3)} * E * E + \dots\} \quad (1.15)$$

$$\text{and} \quad 2\eta\kappa = 1 + 4\pi \operatorname{Im}\{\chi^{(1)} + \chi^{(3)} * E * E + \dots\} \quad (1.16)$$

Even terms in $\chi^{(n)}$ make no contribution for uniform excitation in an isotropic medium due to inversion symmetry. Several constraints are applied now to eq. (1.15) and (1.16). First, it is assumed that no single-photon absorption can occur, because the incident photons have no enough energy, since they lie in the near infrared region (NIR). This allows the imaginary part of $\chi^{(1)}$ to be set equal to zero. Second $\operatorname{Re}\{\chi^{(1)}\} \gg \operatorname{Re}\{\chi^{(3)}\}$ ensuring that the real refractive index η effectively is a constant at its single photon value. This condition removes intensity-dependent components from the refractive index [4].

Eq. (1.16) now becomes:

$$\kappa = \frac{4\pi^2 I' \text{Im}\{\chi^{(3)}\}}{\eta^2 c} \quad (1.17)$$

where $I' = \frac{c\eta E^2}{2\pi}$ is the radiation intensity at ω , expressed this time not as photon flux, hence $I' = I \cdot \hbar\omega$. The absorption coefficient K for the intensity is defined by $\frac{dI'}{dz} = -KI'$ and is given in terms of κ as:

$$K = \frac{2\omega}{c} \kappa = \frac{8\pi^2 \omega I'}{\eta^2 c^2} \text{Im}\{\chi^{(3)}\} \quad (1.18)$$

The absorption coefficient is related with the two-photon absorption cross-section σ_2 through a magnitude called two-photon absorption coefficient, denoted as β . The latter is normally defined using the relation:

$$\frac{dI'}{dz} = -(\alpha + \beta I') I' \quad (1.19)$$

which is usually used for gas samples, but it can be also used for chromophores of biological interest. It is obvious that since single-photon absorption is negligible, $\beta = \frac{K}{I'}$.

Combination of eq. (1.18) and (1.19), allows β to be expressed as:

$$\beta = \frac{8\pi^2 \omega}{\eta^2 c^2} \text{Im}\{\chi^{(3)}\} \quad (1.20)$$

The relationship between β and σ_2 is given by:

$$\beta = 2N \frac{\sigma^{(2)}}{\hbar\omega} \quad (1.21)$$

where N represents the molecular number density, and the factor 2 arises from the absorption of two photons. Combining eq. (1.20) and (1.21) and neglecting N in order to express σ_2 in $\text{cm}^4 \cdot \text{sec} / \text{photon} \cdot \text{molecule}$ the following relation between σ_2 and $\chi^{(3)}$ arises [52]:

$$\sigma_2 = \frac{4\pi^2 \hbar \omega^2}{\eta^2 c^2} \text{Im}\{\chi^{(3)}\} \quad (1.22)$$

Eq. (1.22) serves as the basis for determining the value of two-photon absorption cross-section of a single molecule through measurements of the third-order optical susceptibility of a collection of such molecules [3].

1.3 Two Photon Excited Fluorescence

Box 4: Basic relations describing TPEF.

In TPEF, the quantum yield of fluorescence Φ_{2f} is defined as:

$$\Phi_{2f} = \frac{\text{number of fluorescence emitted photons}}{\text{number of pair of absorbed photons}} \quad (1.23)$$

Eq. (1.10) gives the rate, W_2 at which a molecule populates an excited state through two-photon absorption. This rate, when multiplied by the fluorescence quantum efficiency Φ_{2f} , provides the rate at which a photon is emitted from the molecule, which undergoes from the excited to the ground state. In other words, the power of the TPEF, P_{TPEF} in $\frac{\text{photons}}{\text{sec}}$ is given by:

$$P_{TPEF} = \frac{1}{2} \Phi_{2f} \sigma_2 I^2 \quad (1.24)$$

Finally, if we define $\sigma_{TPEF} = \Phi_{2f} \cdot \sigma_2$ as the two-photon fluorescence cross-section (or action cross-section), eq. (1.24), can be expressed as:

$$P_{TPEF} = \frac{1}{2} \sigma_{TPEF} I^2 \quad (1.25)$$

Once an excited state has been populated through two-photon absorption, a process of deactivation follows with the same characteristics as the one-photon excited fluorescence process (OPEF). OPEF and TPEF lie their differences in the way that the excited state is reached, but not in the way that the excited state is deactivated to populate again the ground state S_0 . Fluorescence in both cases is only one of the possible ways that the excited molecule can undergo to the ground state. Thus, in TPEF, alike in OPEF, a magnitude called quantum yield of fluorescence can be introduced, and we denote it as Φ_{2f} , in order to distinguish

it from the quantum yield of fluorescence in the OPEF case, Φ_f . In **Box 4**, some basic relations are given, describing quantitatively the TPEF.

As far as the polarization of the emitted photons through fluorescence is concerned, it is expected that when fluorescent molecules are illuminated with linear polarized light, the emitted photons have a specific polarization, related with the polarization of the incident photons and the specific transition moment between the excited and the ground state. This specific transition is directly related with the orientation of the molecules in the space. However, since the molecules are free to rotate during the time taken for the electronic transitions to occur, changing their orientation and the corresponding transition moment, the fluorescence emission is largely unpolarized. For small fluorescent molecules, the rotational correlation time is much shorter than the fluorescence lifetime. For example, fluorescein has a rotational correlation time of 120 ps, 40 times shorter than its fluorescence lifetime [5]. By contrast, when the fluorescent molecule is relatively large, its rotational correlational time is larger than its fluorescence lifetime, and the fluorescence emission is more polarized. GFP is an example of such a fluorescent molecule [6].

1.4 TPEF Microscopy

TPEF microscopy is often compared with confocal microscopy, which is an example of one-photon excited fluorescence microscopy (OPEF). One-photon excited fluorescence is produced in an extended region of the specimen, and not only in the plane of focus. Since the one-photon absorption is a linear process, the intensity of light is enough to excite the fluorescent molecules, also out of the focal volume. However, 3-D resolution is obtained by placing a pinhole aperture in the emission light path at a conjugate location of the focal volume in the specimen. Photons generated inside this volume will be focused at the pinhole aperture and can be transmitted to the detector. On the contrary, photons originated outside this focal volume will be defocused at the aperture plane and will be blocked. In other words, the maximum resolution in the longitudinal direction, denoted as z , is achieved by placing a pinhole before the detector, while the maximum resolution in the transversal directions, in the plane of focus, denoted as x and y , is achieved by the tight focusing of the incident beam to the diffraction limit, by means of an efficient objective lens. It must be emphasized, however, that 3-D resolution (in the longitudinal direction), is obtained by limitation of the region of observation, not of the region of excitation, as in the transversal directions.

A typical TPEF microscope is very similar to the confocal microscope, and will be described analytically in the experimental part of this work. Its main difference from the confocal microscope is the lack of pinholes, since its 3-D sectioning ability is based on the limitation of the excitation region, in all three directions x , y and z . The incident light lies, this time, in the infrared region of

the optical spectrum, and the fluorophores contained in the sample can absorb light, only through the nonlinear two-photon absorption process. Since the two-photon absorption cross-section σ_2 is significantly lower than the one-photon absorption cross-section σ_1 , as eq. (1.11) implies, two-photon absorption occurs with appreciable rates only in regions of high temporal and spatial photon concentration. The high temporal concentration of photons is achieved by the availability of pulsed lasers with pulse widths of the order of few femtoseconds. The high spatial concentration of photons is achieved as in the confocal microscope, by focusing the beam with a high numerical aperture (NA) objective to a diffraction limited focus. Almost the total fluorescence intensity comes from a $1 \mu\text{m}$ thick region about the focal point for objectives with high NA (≥ 0.8), like the one used in this work. Thus, 3-D images can be constructed without a confocal pinhole due to the quadratic dependence of two-photon fluorescence intensity upon the excitation photon flux (eq. (1.10)), which decreases rapidly away from the focal point. In **Figure 1.3**, it is depicted the main difference between the one-photon confocal and the TPEF microscopy, as far as the excitation region is concerned. It is shown that in the confocal microscopy, the out-of-focus plane excitation is very intense, whereas in the TPEF microscopy is not.

Confocal and TPEF microscopy have their own advantages and disadvantages compared to each other. TPEF microscopy is more adequate for deep tissue imaging since the excitation wavelength lies in the IR and suffers less from tissue absorption and scattering. On the other hand, the excitation wavelengths of confocal microscopy lie in UV and blue region, thus the penetration depth is limited.

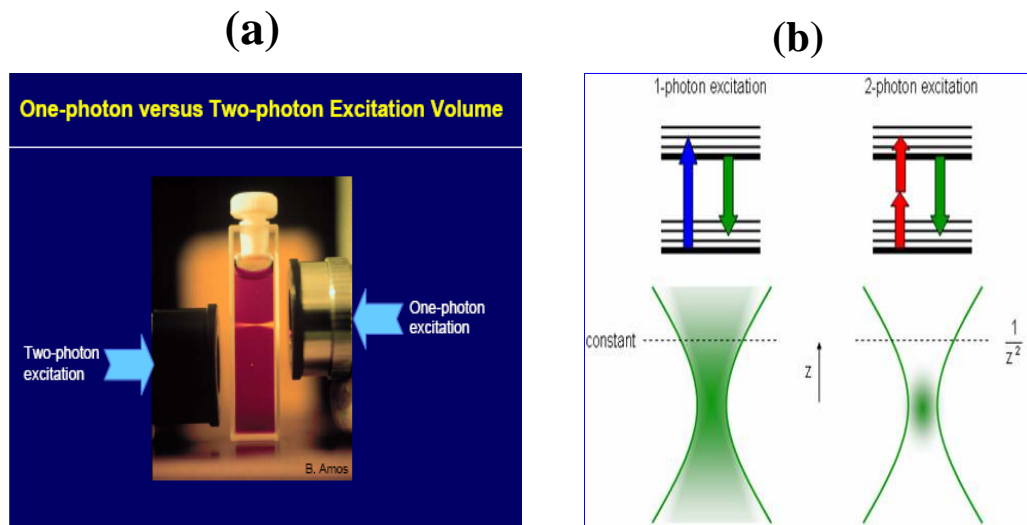


Figure 1.3: a) The excitation region (pink colour) is limited in the focal plane for the two-photon case, while extends above and below in the one-photon excitation. b) The same characteristic is noted in the two comparative pictures. [7]

Apart from the deeper penetration, TPEF microscopy exhibits two more important advantages. First, since the excitation light is in the IR region, the wide separation between the excitation and the emission spectra ensures that the excitation light can be rejected without filtering out any of the fluorescence photons, resulting in sensitivity enhancement and better signal to noise ratio (SNR). Second, the fact that the 3-D sectioning arises from the limitation of the excitation region, ensures that photobleaching and photodamage of the biological specimen are restricted only to the focal point. Since out-of-plane fluorophores are not excited, they are not subject neither to photodamage nor to photobleaching. The minimally invasive nature of two-photon imaging can be best appreciated in a number of embryology studies. Previous work on long-term monitoring of *C. elegans* and hamster embryos using confocal microscopy failed because of photodamage-induced developmental arrest. However, posterior

TPEF microscopy studies indicated that the embryos of these organisms can be imaged repeatedly over the course of hours without observable damage [8,9].

At this point it is necessary to describe briefly the terms photobleaching and photodamage. Photobleaching occurs when, under illumination, the triplet state in the fluorophore reacts with molecular oxygen, forming a nonfluorescing molecule.

On the other hand the term photodamage is more general and describes various mechanisms. Endogenous and exogenous fluorophores act as photosensitizers in photo-oxidative processes [10, 11], and the photoactivation of these fluorophores results in the formation of reactive oxygen species that trigger the subsequent biochemical damage cascade in cells. Flavin-containing oxidases have been identified as one of the primary endogenous targets for photodamage [12].

As far as the resolution of the two techniques is concerned, confocal microscopy is advantageous. For the excitation of the same fluorophore, two-photon resolution in x and y direction, is roughly half the one-photon confocal resolution, given that the excitation beam is focused to the diffraction limit. This lower spatial resolution is due to the use of longer wavelength light, approximately twice as long as the excitation light in confocal microscopy. However, in many practical setups the focusing of the fundamental laser beam to the diffraction limit is not feasible. In these cases, the resolution of the TPEF microscopy in x and y direction is superior to the corresponding resolution of the one-photon confocal microscopy, due to the quadratic dependence of two-photon fluorescence intensity upon the excitation photon flux. The resolution of the two kinds of microscopy in the longitudinal direction can not be directly compared, owing to the dependence of the confocal resolution on the size and the

quality of the pinhole. However, it is of the same order of magnitude. In **Box 5** the TPEF active volume is defined as the region from where the TPEF exclusively originates. Analytical expressions are presented.

BOX 5: TPEF active volume – Resolution of TPEF microscopy

The usual description of a Gaussian beam emerges from the paraxial approximation. However, the paraxial approximation is not valid when the beam is tightly focused.

The electric field of a Gaussian tightly focused excitation beam of angular frequency ω propagating in the z direction and polarized in the $\hat{\varepsilon}$ direction may be approximated by:

$$\vec{E}(x, y, z) = -iE_\omega \exp\left(-\frac{x^2 + y^2}{w_\rho^2} - \frac{z^2}{w_z^2} + i\xi k_\omega z\right) \hat{\varepsilon} \quad (1.26)$$

where w_ρ and w_z are respectively the radial and axial beam waists at the focal center, $\hat{\varepsilon}$ is a unit vector in the $x - y$ plane, k_ω is the wave vector at frequency ω , and ξ represents the effective reduction in the axial propagation vector caused by the phase anomaly, or Gouy shift. We define the TPEF active volume as the volume from where TPEF almost exclusively originates. This volume is critically dependent on the radial and axial beam waists, w_ρ and w_z , and is given by:

$$V_{TPEF} = \left(\frac{\pi}{2}\right)^{(3/2)} w_\rho^2 w_z \quad (1.27)$$

Owing to the above definition of the TPEF active volume, the longitudinal and the transversal resolution of the TPEF microscopy are defined as w_z and w_ρ , correspondingly. In **Figure 1.4** a focused Gaussian beam is depicted and its main parameters are shown.

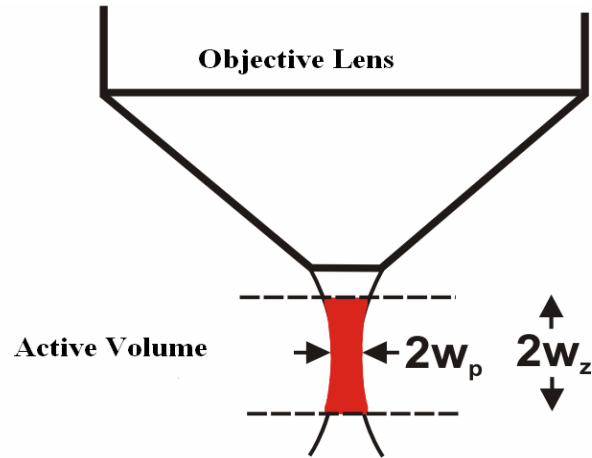


Figure 1.4: Tightly focused Gaussian beam. The radial and axial beam waists, w_p and w_z correspondingly, determine the TPEF active volume, the region from which TPEF exclusively originates.

1.5 Fluorescent Proteins

1.5.1 Green Fluorescent Protein (GFP)

Green Fluorescence Protein (GFP) is the extrinsic fluorophore used mainly in our work and the main source of the TPEF signal, detected from our biological system (*C. elegans*). Hence, a brief presentation of GFP is necessary at this point.

GFP was initially discovered in 1962 by Shimomura and colleagues, from the jellyfish *Aequorea Victoria*. [53] In **Figure 1.5** a photograph of the jellyfish *Aequorea Victoria* is depicted. *Aequorin* emits its chemiluminescence at 470 nm , which excites GFP. After an energy transfer, GFP emits its fluorescence at 508 nm .

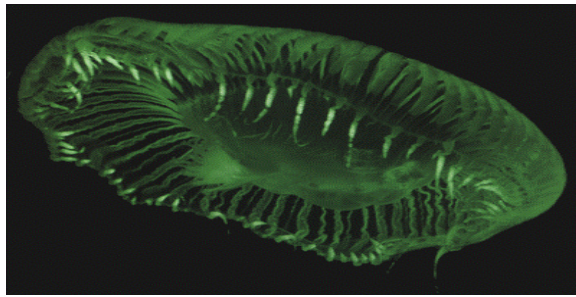


Figure 1.5 Photograph of the jellyfish *Aequorea Victoria*.

It is a protein of 238 amino-acids with a molecular weight of 27 or 30 kDa, and is an exceptionally stable protein concerning variations of *ph* and temperature [36].

Its extraordinary stability is a consequence of its compact tertiary structure. In

Figure 1.6 this structure is illustrated. GFP is the representative of a new protein

fold, which have been named as *beta-can* [37]. On the outside, 11 antiparallel

beta strands (yellow) form a very compact cylinder.

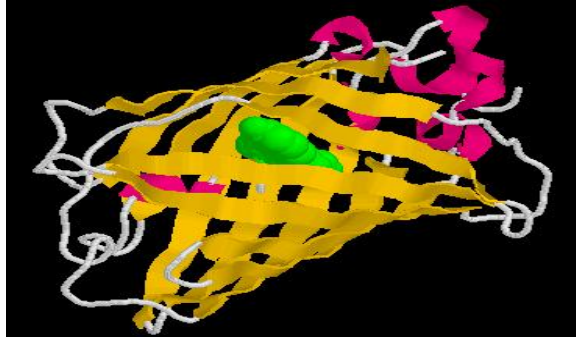


Figure 1.6: Tertiary structure of *Aequorea Victoria* GFP. On the outside, 11 antiparallel beta strands (yellow) form a very compact cylinder. Inside this beta-structure there is an alpha-helix (purple), in the middle of which is the chromophore (green). There are also short helical segments (grey) on the end of the can.

Inside this beta-structure there is an alpha-helix (purple), in the middle of which is located the chromophore (green). There are also short helical segments (grey) on the end of the can. The cylinder has a diameter of about 30 Å and a length of about 40 Å. The very compact single-domain structure with the chromophore centrally located in the molecule and protected from bulk solvent can explain a number of characteristics of GFP, such as the high quantum yield of fluorescence (0.72-0.85) and the inability of oxygen to quench the excited state [38].

1.5.2 Chromophore of GFP

GFP is unique among fluorescent proteins in that its chromophore is not a separately synthesized prosthetic group but composed of modified amino-acid residues within the polypeptide chain. The chromophore is positioned in an orientation that is close to perpendicular to the axis of the cylinder. The chromophore itself is a p-hydroxybenzylidene-imidazolidone. It consists of residues 65-67 (Ser - *dehydro*Tyr - Gly) of the protein. The cyclized backbone of these residues forms the imidazolidone ring. In **Figure 1.7** the initial amino-

acids, as well as the biosynthetic scheme of the chromophore, are depicted. Although the amino-acid sequence (Ser-Tyr-Gly) can be found in a number of other proteins as well, it is neither cyclized in any of these, nor is the Tyrosine oxidized, nor are these proteins fluorescent. This implies that the tendency to form such a chromophore is not an intrinsic property of this tripeptide.

When the neutral phenol group of the chromophore, depicted in Figure 1.6c, is deprotonated, the phenol group is converted to a phenolate anion. The chromophore with the neutral phenol group has an absorption peak of 395 nm, whereas the chromophore with the phenolate anion has an absorption peak of 475 nm. In native GFP, both forms of the chromophore coexist, with the form containing the neutral phenol group to be predominant [39]. Thus, in the absorption spectrum of the native GFP, both peaks are evident [36], as it is illustrated in **Figure 1.8**. The form of GFP with the phenol group, when illuminated and excited, turns also its phenol group to a phenolate anion. Thus, both forms of native GFP have the same excited state containing phenolate anion rather phenol group, and their emission spectra are identical, exhibiting a peak at 508 nm, as it is illustrated in **Figure 1.8**.

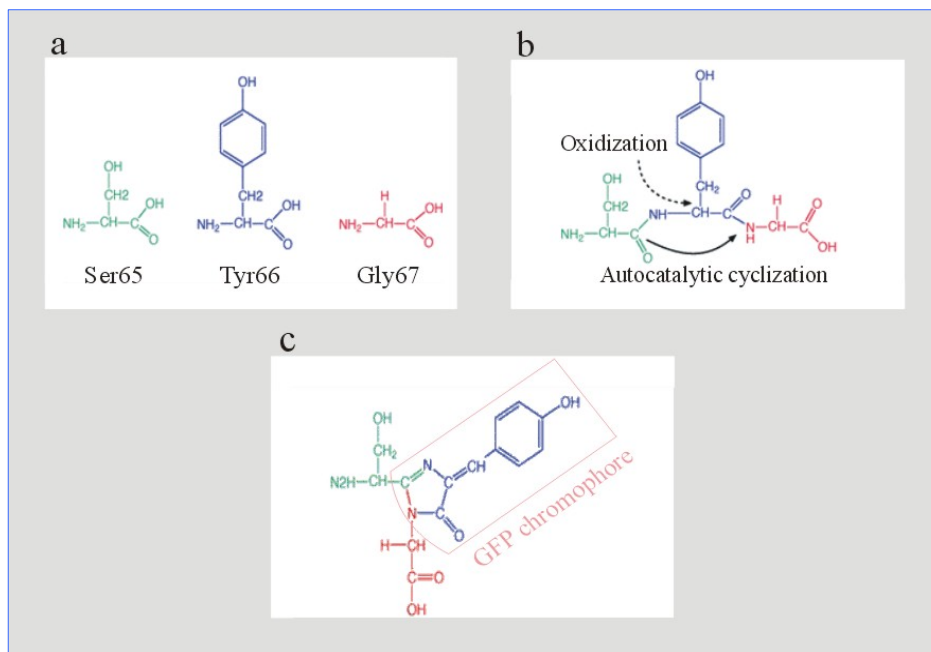


Figure 1.7: a) The chromophore of *Aequorea* GFP consists of residues 65-67 (Ser - *dehydro*Tyr - Gly) of the protein. b) The biosynthetic scheme includes the oxidation of Tyrosine and the autocatalyzed cyclization of the three amino-acids. c) The chromophore of GFP is enclosed by the pink line. It has a phenol group at one end of the molecule, conjugated to an imidazolinone group at the other.

Mutants of GFP can be devised in which all chromophores are in the phenolate form. In our work such a mutant was used, which is called S65C. Its absorption peak is at 479 nm and its emission peak at 507 nm [39]. S65C has been proved to be efficient for TPEF, although in the literature there are no values for its TPEF cross-section σ_{TPEF} .

Moreover, the chromophore of GFP has been proved to be efficient for significant Hyper-Rayleigh Scattering (HRS). Although it is not officially referred to as push-pull molecule, it has all the characteristics of the push-pull molecules that make them HRS efficient, namely the donor and the acceptor moieties, as well as the conjugation path between them. Upon illumination, the GFP molecule undergoes significant electron redistribution, with the phenolate anion to serve as a donor, and the imidazalinone group to serve as the acceptor.

This electron redistribution results in a large induced dipole, and enables the chromophore of the GFP to produce HRS signal [40]. Unfortunately, there are no elements in the literature for its SHG cross-section, σ_{SHG} .

It is worth mentioning that, due to the excitation wavelength used in this study (1028nm), the signal from the biological specimen (*C. elegans*) at 514nm comprises of both SHG and TPEF. The independently measured SHG signal (from the oriented endogenous proteins of the worm) at 514nm is at least 30 times stronger than the TPEF counterpart (arising from the GFP molecules). Consequently, the dominant contribution at 514nm comes from SHG signals. This signal abruptly reduces, as the monochromator setting is changed 5-6nm around this wavelength. This observation is in perfect agreement with the spectral distribution, which presents the non-linear phenomenon of Second Harmonic Generation. The collected signal exclusively comes from TPEF from the GFP molecules for $\lambda > 518$ nm. As it is expected, the spectrum of Two-Photon Excitation Fluorescence does not present any abruptly disappear over a few nanometers.

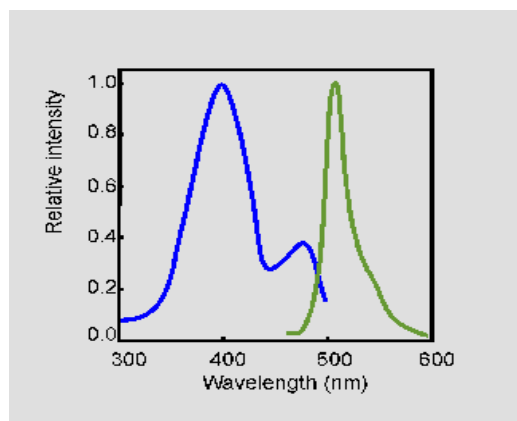


Figure 1.8: The excitation spectrum of native GFP from *Aequorea Victoria* (blue) has two excitation maxima at 395 nm and at 475 nm. The fluorescence emission spectrum (green) has a peak at 508 nm and a shoulder at 540 nm.

1.6 DsRed

1.6.1 Introduction

Dsred is a tetrameric, recently cloned 28-kDa fluorescent protein responsible for the red coloration around the oral disk of a coral of the *Discosoma* genus. DsRed has attracted tremendous interest as a potential expression tracer and fusion partner that would be complementary to the homologous green fluorescent protein from *Aequorea*.^[41] The first Anthozoa-derived fluorescent protein to be extensively investigated was derived from the sea anemone *Discosoma striata* and originally referred to as **drFP583**, but is now commonly known as **DsRed**.



Figure 1.9: Discosoma Striped Mushroom Reef Coral. ^[42]

1.6.2 Description of the structure of DsRed

DsRed is an 11-stranded β -can with a central α -helix, nearly identical in topology to the homologous GFP (**Fig 1.10a**). Four non-crystallographically related molecules in our $P2_1$ crystals form a tightly packed tetramer with orthogonal 222 symmetry through two extensive protein interaction surfaces. The top and bottom of each β -can is sealed off from bulk solvent by protein atoms, providing a rigid environment within the core of the structure for the DsRed chromophore. The

structural rigidity and insulation from bulk solvent is likely key for the efficient quantum yield of fluorescence observed in DsRed. [43]

As is the case in GFP, the DsRed chromophore rests in the middle of a α -helix that runs through the centre of the β -can fold and clearly shares much of the chemical mechanism of formation with GFP, namely autocatalytic cyclization of residues Gln 66, Tyr 67 and Gly 68 and dehydrogenation of the C_{α} - C_{β} bond of Tyr 67 (**Figs: 1.10b**). DsRed monomers comprising one tetramer are highly similar to each other (average root mean square (r.m.s.) deviation of C_{α} atoms of 0.18 Å), and each monomer differs from *A. Victoria* GFP with an average C_{α} r.m.s. deviation of 1.9 Å. The majority of the backbone structural variation between DsRed and GFP occurs in loop regions that form the ends of the β -can structure.

The oligomeric organization of DsRed suggests the possibility of fluorescence resonance energy transfer (FRET) between chromophores within the tetramers. Indeed, time-resolved anisotropy experiments indicate a rapid phase of depolarization in DsRed that likely results from intratetramer energy transfer. The physical basis for FRET is dipole – dipole coupling between donor and acceptor chromophores, where the probability of energy transfer depends on the spectral overlap between donor emission and acceptor absorbance, and the relative angular displacement and distance between the respective dipoles. **Fig.1.10b** shows the relative orientations of chromophores in the DsRed tetramer.

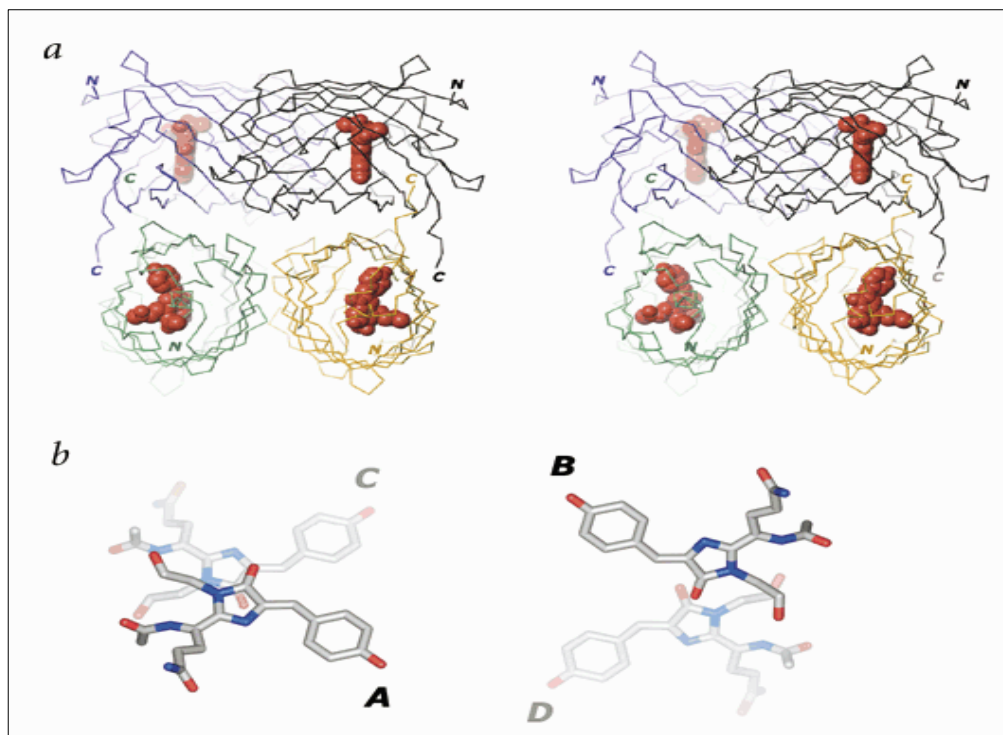


Figure 1.10: a) Stereoview of the DsRed tetramer. C α traces are colored gold, green, violet and black, each representing individual monomers that are related by orthogonal 222 noncrystallographic symmetry. Atoms in each chromophore (residues Gln 66, Tyr 67 and Gly 68) and the main chain *cis* peptide bond between Phe 65 and Gln 66 are shown as red van der Waals spheres. b) Relative orientation of the four chromophores of the DsRed tetramer. Chromophores are arbitrarily labelled A, B, C and D. The A-B and C-D pairs are 22 Å apart, the A-C and B-D pairs are 38 Å apart and the A-D and B-C pairs are 43 Å apart. [43]

Once the protein has fully matured, the fluorescence emission spectrum of DsRed features a peak at 583nm whereas the excitation spectrum has major peak at 558 nm and a minor peak round 500nm. The wavelength of our excitation source is 1028nm. By employing DsRed protein the collected TPEF images from the nematode are located to different spectral region ($\lambda=580-595\text{nm}$) in comparison with the obtained SHG images ($\lambda=514\text{nm}$) from the worm. Additionally according to the absorption spectrum characteristic of DsRed (**Fig. 1.11**), the two photon absorption arising from molecules labelled with DsRed is

much stronger (at 514nm) than the two photon absorption arising from molecules labelled with GFP. Consequently by employing our excitation wavelength (1028nm) the DsRed protein appears to be more advantageous for the realization of in vivo two photon fluorescence measurements in biological samples in comparison with the GFP.

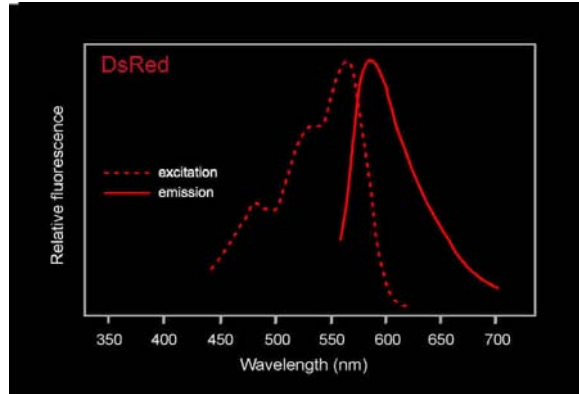


Figure 1.11: The excitation and the emission spectrum of DsRed

Several problems are associated with DsRed in practice. Maturation of DsRed fluorescence occurs slowly and proceeds through an intermediate chromophore stage where a majority of the fluorescence emission is seen in the green region.

Termed the **green state**, this artifact has proven problematic for multiple labelling experiments with other green fluorescent proteins because of the spectral overlap. Furthermore, DsRed is an obligate tetramer and can form large protein aggregates in living cells. Although these features are inconsequential for the use of DsRed as a reporter of gene expression, the usefulness of DsRed as an epitope tag is severely limited. In contrast to the jellyfish fluorescent proteins, which have been successfully used to tag hundreds of proteins, DsRed conjugates have proven much less successful and are often toxic. [44]

Even if DsRed is a source of stronger signal of TPEF than GFP, for the reasons described above, most of the samples used in our study, are stained with GFP.

2.1 Hyper-Rayleigh Scattering (HRS) from a single molecule

To first order, the molecule may be regarded as a simple electrical dipole. That is, the molecular electron distribution may be regarded as mobile relative to the nuclear distribution, and the molecular dipole moment is defined as $\vec{\mu} = q\vec{r}$, where q is the nuclear and electronic charges and \vec{r} is their relative displacement. Changes in $\vec{\mu}$ are occasioned by forces applied to the molecular electrons. In the analysis carried in this chapter, only electric dipole forces are considered, that is forces whose interaction energies are given by $W = \vec{\mu}\vec{E}$, where \vec{E} is the applied (incident) electric field. The molecules, as electric dipoles, can either be symmetrical or asymmetrical. The simplest form of asymmetry is possessed by a uniaxial polar molecule. In this case the molecule may be regarded as a one-dimensional rod, along which its electron cloud can shift up or down. We begin by examining the case when the molecule is perfectly symmetric, meaning that the molecular dipole moment vanishes at rest.

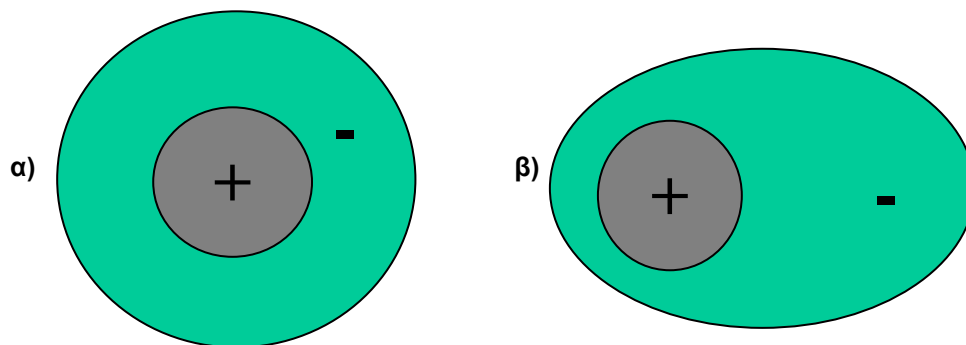


Figure 2.1: a) The charge distribution due to the electrons (-) is symmetrical to the nuclear distribution (+). b) Asymmetrical electron distribution.

Upon illumination, the electron cloud, depicted in **Figure 2.1** as a point electron, is subject to a sinusoidal force along the molecular axis, whose frequency is ω . Because the molecule is symmetric, the resultant oscillation of the electron cloud is also symmetric and generates radiation at the same frequency ω . Such radiation is called *Rayleigh scattering* [13]. It is linear in the sense that the scattered frequency is exactly the same as that of the driving illumination light. In this example of a symmetric molecule, no second-harmonic light (light of frequency 2ω) can be generated.

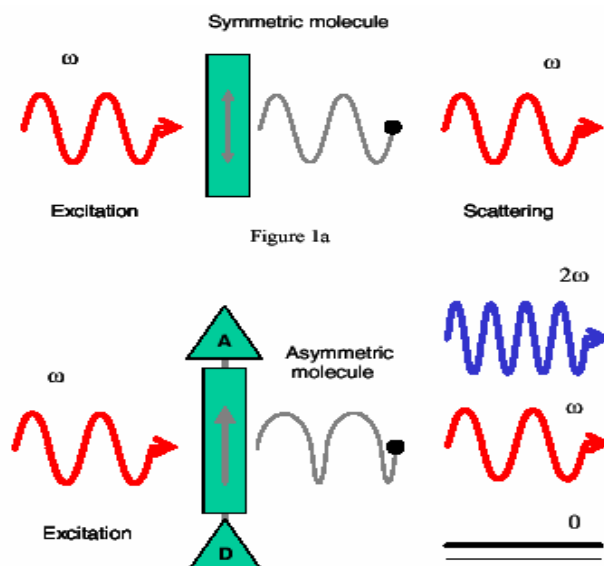


Figure 2.2: When driven by light of frequency of ω , the induced electron motion in a symmetric uni-axial molecule produces Rayleigh scattering at the same frequency ω . In an asymmetric molecule, the induced electron motion produces scattered light at frequencies ω and 2ω . The latter is called Hyper-Rayleigh scattering (HRS).

One way to impart charge asymmetry on a molecule is by grafting electron donor (D) and acceptor (A) moieties to its opposite ends, producing what is known as a “push-pull” chromophore [14], since both moieties act in tandem to favor electronic motion in the direction $D \rightarrow A$. When an asymmetric molecule is subjected to the same sinusoidal driving field as above, the resultant electron motion, though still periodic, is no longer symmetric, as shown in the lower part

in **Figure 2.2**. The acceleration of the electron motion contains additional frequency components. In addition to the usual linear component at frequency ω , the scattered radiation contains nonlinear components at frequencies 0 and 2ω . The 0 frequency component is called optical rectification [15]. The 2ω component is called Hyper-Rayleigh scattering (HRS), and is the center of the analysis, carried out in this chapter. As a general rule, the generation of second-harmonic light requires a non-symmetric source. In **Box 6**, the basic equations describing the HRS from a single molecule are presented. The description includes the definition of the SHG cross-section σ_{SHG} , so that a direct comparison between the SHG and the TPEF emission can be made at the molecular level [16].

BOX 6: SHG originated from a single molecule

Molecular SHG is caused by the nonlinear dependence of the induced dipolar moment $\vec{\mu}$ of the molecule on the incident optical electric field \vec{E} . Thus $\vec{\mu}$ can be expanded in a Taylor's series about $\vec{E} = 0$:

$$\vec{\mu} = \vec{\mu}_o + \alpha * \vec{E} + \frac{1}{2} \beta * \vec{E} * \vec{E} + \frac{1}{6} \gamma * \vec{E} * \vec{E} * \vec{E} + \dots \quad (2.1)$$

where α is the linear molecular polarizability and β and γ are the nonlinear first and second hyperpolarizabilities [17]. SHG is governed by β , which is a tensor with 27 elements β_{ijk} , where $i, j, k = x, y, z$. For simplicity we assume the simplest form of asymmetric molecules, those having the character of “push-pull” molecules. They are uniaxial polar molecules, which can be regarded as rods, as in Figure 2.1. We further assume that such a “rod” is aligned along the x axis, and that the excitation field is linearly polarized in the same direction. Under this description, only the β_{xxx} component plays an active role and should be examined. If the excitation light has frequency ω , the induced dipole moment at frequency 2ω will be given by:

$$\vec{\mu}_{2\omega} = \frac{1}{2} \beta_{xxx} \cdot E^2 \hat{x} \quad (2.2)$$

The radiated second-harmonic far field at an inclination ψ from the x axis is:

$$\vec{E}_{2\omega}(\psi) = -\frac{\mu_{2\omega}\omega^2}{\pi\varepsilon_0c^2r}\sin(\psi)e^{-2i\omega[t]}\hat{\psi} \quad (2.3)$$

where ε_0 is the free-space permittivity, c is the speed of light, r is the observation distance from the dipole, and $[t]$ is the corresponding retarded time. The resultant power per differential solid angle at an inclination ψ , in units of $\text{photons}/\text{sec}$, may be expressed as:

$$P_{2\omega}(\psi) = -\frac{3}{16\pi}\sigma_{SHG}\sin^2(\psi)I^2 \quad (2.4)$$

where I is the excitation intensity in units of $\text{photons}/\text{sec}\cdot\text{area}$ and σ_{SHG} is defined (in $\text{cm}^4\cdot\text{sec}/\text{photon}\cdot\text{molecule}$) as:

$$\sigma_{SHG} = \frac{4n_{2\omega}\hbar\omega^5}{3\pi n_{\omega}^2\varepsilon_0^3c^5}|\beta|^2 \quad (2.5)$$

In eq. (2.5) n_{ω} and $n_{2\omega}$ are the indices of refraction at ω and 2ω . The definition of σ_{SHG} is such, that the total power, obtained by integration of eq.(2.4) over all solid angles, reduces to the simple expression:

$$P_{SHG} = \frac{1}{2}\sigma_{SHG}I^2 \quad (2.6)$$

We recall that the fluorescence emitted by a molecule, undergoing two-photon excitation can be expressed similarly according to eq. (1.25) as $P_{TPEF} = \frac{1}{2}\sigma_{TPEF}I^2$. In this sense, σ_{SHG} and σ_{TPEF} may be expressed in the same units for direct comparison.

2.2 HRS coming from a number of biological molecules

In order to distinguish HRS from Rayleigh scattering or from fluorescence, some important aspects have to be considered. As an illustration, two asymmetric molecules are considered, that are located in close proximity, separate by a distance d much smaller than an optical wavelength, and oriented in parallel directions. When these molecules are illuminated by a driving field, their respective electron motions will be identical, and the resultant HRS from both molecules will be in phase (**Figure 2.3a**). In other words, the net HRS amplitude will be doubled, meaning that the net HRS power will be quadrupled relative to the HRS power obtained from a single molecule. If, on the other hand, the two molecules are oriented anti-parallel, the asymmetric components in their electronic motions are now inverted relative to one another. Thus, their respective HRS amplitudes are out-of-phase and exactly cancelled (**Figure 2.3b**). More specifically, it has been empirically found, that in biological samples, when two antiparallel oriented molecules have a distance $d < \lambda/10$, they do not produce a total detectable signal [16, 18]. It is noted that the dependence of radiative phase on molecular orientation is a characteristic property of HRS that does appear neither in Rayleigh scattering nor in fluorescence. In particular, the Rayleigh scattered components from both molecules in **Figure 2.3** remain in phase regardless of whether the molecules are oriented parallel or anti-parallel. Similarly, if the molecules are fluorescent, the phases of their fluorescence emission are essentially random, also independent on molecular orientation.

For imaging applications, one is not interested in looking at the HRS from one, or even two molecules, but from an entire population of molecules. First, a

configuration of N molecules in solution is considered (**Figure 2.4a**). Since the orientations of these molecules are random, the phases of their individual SHG contributions are also random. The molecules produce HRS incoherently, and the total generated HRS scales as the number of the radiating molecules: $P_{HRS} \sim N$. Alternatively, in **Figure 2.4b** a configuration is illustrated, where the molecules are globally aligned along the same direction.

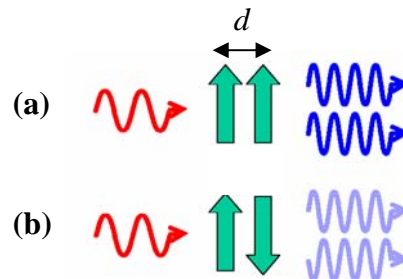


Figure 2.3 : The HRS from two molecules located close together. a) If the molecules are parallel, their HRS are in phase and interfere constructively. b) If the molecules are anti-parallel, their HRS are out-of-phase and cancel each other.

The phases of the individual HRS contributions from each molecule are now prescribed by the phase of the driving field, which is presumably well defined. The HRS is therefore produced coherently, meaning that interference effects play a significant role. When HRS is produced coherently by an organized population of molecules, it is called SHG. Due to the coherent character of SHG, its total power scales as the square of the number of radiating molecules: $P_{SHG} \sim N^2$. Moreover, because of the same character, the angular distribution of SHG is highly structured. In general, SHG is constrained to propagate along the same direction as the driving field.

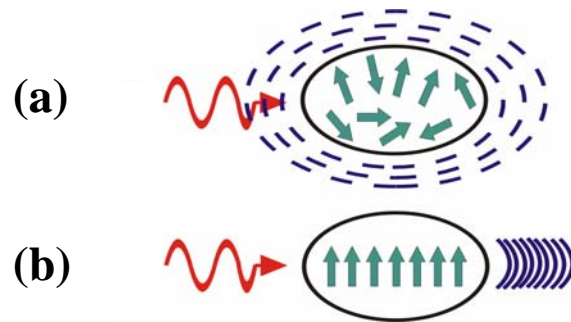


Figure 2.4 : The HRS from a population of N molecules. a) Randomly oriented molecules scatter incoherently and the total HRS scale as N . b) Aligned molecules scatter coherently producing SHG. This signal is well directional, and its power scales as N^2 .

As a conclusion, for imaging applications, it is highly desirable that the radiating molecules are organized than unorganized, because first, much more SHG signal is generated for the same number of molecules, and second, the signal can be collected more efficiently due to its high directionality.

In this work, describing the construction and the applications of a SHG microscope, the insight in the molecular level is the appropriate way to describe the nonlinear response of the biological specimen. In a next paragraph, the calculations for the coherent summation of the individual molecular HRS, resulting in a total SHG signal, will be presented, and conclusions for the directionality and the magnitude of the signal will be carried out. However, some basics for the macroscopical description of SHG are provided in **Box 7**, in order to obtain a full understanding of the nonlinear phenomenon of SHG.

BOX 7: Macroscopical description of SHG

The nonlinear response of a material to an incident electric field can be described, by eq. (1.12), which is reproduced here for convenience:

$$P = \chi^{(1)} * E + \chi^{(2)} * E * E + \chi^{(3)} * E * E * E + \dots \quad (2.7)$$

While TPEF is determined by the 3rd order susceptibility tensor $\chi^{(3)}$, SHG is correspondingly determined by the 2nd order susceptibility tensor $\chi^{(2)}$. $\chi^{(2)}$ is a bulk property of the medium, referring to the entire population of the individual molecules of the medium. The total power of the generated second-harmonic signal P_{SHG} , is proportional to:

$$P_{SHG} \sim \left(\chi^{(2)}\right)^2 I^2 \quad (2.8)$$

where again I is the excitation intensity in units of $\frac{\text{photons}}{\text{sec} \cdot \text{area}}$. The bridging between the macroscopical behavior of the material, as far as SHG is concerned, and the HRS originated from the individual molecules is achieved through the relation:

$$\chi^{(2)} = N_s \langle \beta \rangle \quad (2.9)$$

where N_s is the density of molecules, and β is the first molecular hyperpolarizability, as it has already been defined in Box 6. The brackets denote an average of orientation, which shows the need for orientational organization among the molecules that constitute the material. Moreover, it makes clear the need for an environment lacking a center of symmetry. In other words, media that are characterized by inversion symmetry, do not have the ability for SHG, since their $\chi^{(2)}$ becomes zero. This property is well known [19]. Let us assume now, to our convenience, that we have a population of molecules, completely aligned to each other, so that the brackets do no have a sense anymore. Combining eq. (2.5) and (2.9), it is clear that the molecular SHG cross-section, σ_{SHG} is proportional to the square of the 2nd order susceptibility tensor $\chi^{(2)}$:

$$\sigma_{SHG} = \frac{4n_{2\omega} \hbar \omega^5}{3\pi n_{\omega}^2 \epsilon_0^3 c^5} \left| \chi^{(2)} \right|^2 \quad (2.10)$$

We recall combining eq. (1.22) and (1.25) that the molecular TPEF cross-section σ_{TPEF} is proportional to the imaginary part of the 3rd order susceptibility tensor $\text{Im}\{\chi^{(3)}\}$. As such, σ_{TPEF} tends to be much larger than σ_{SHG} in practice. However, due to the coherent character of the SHG, and the coherent summation of the HRS from the individual molecules, the total SHG signal can be comparable or even larger from the total TPEF signal, emerging from an entire population of molecules.

For the coherent summation of the HRS radiations from single molecules, the knowledge of three parameters is necessary. First, the characteristics of the molecular hyperpolarizability of the single molecules. Second, the way in that, the single molecules are globally organized inside the biological specimen. Third, the way in that the beam is incident on the sample, and particularly if the beam is collimated or it is tightly focused. In **Figure 2.5**, it is depicted the simplistic case of a collimated beam, incident on a region, where well-organized asymmetrical molecules are located. The beam can be described in this region as a planar wave with its wavefronts well-defined and perpendicular to the propagation axis z .

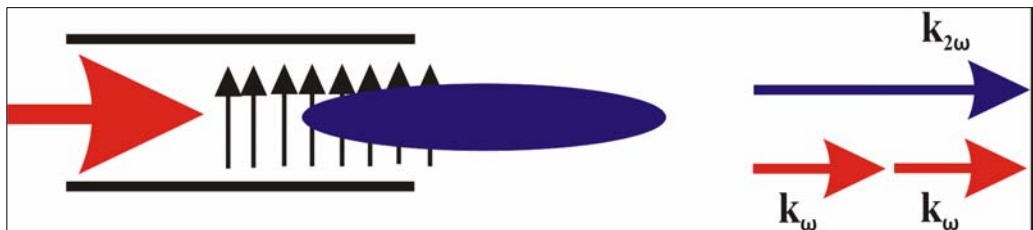


Figure 2.5: SHG from well-organized asymmetrical molecules, when illuminated by a collimated laser beam. Momentum conservation principle assures that the SHG signal propagates on-axis.

The phase of the HRS produced by each molecule is governed by the phase of the driving field. However, in this case, the driving field is propagating, meaning that the HRS produced by the individual molecules-emitters propagates as well: Molecules that are located leftmost, generate HRS earlier than those located

rightmost. The resulting SHG radiation pattern can be evaluated by treating each molecule in the interaction area as a local emitter of second-harmonic radiation. The phase and amplitude of this radiation is precisely determined by the phase and the amplitude of the driving field at the same location. When the second-harmonic contributions from each molecule, given by eq. (2.3), are added, taking into account their respective phase and amplitude, the resulting total SHG is found to propagate in the same direction as the driving field. This result arises directly from the “*momentum conservation principle*”, and describes the well-known in nonlinear optics “*phase matching condition*”: To ensure momentum conservation in the axial direction, the second-harmonic photon whose momentum is twice that of a driving photon, must propagate in the same direction as the driving photons, as illustrated vectorially in Figure 2.5.

The illumination geometry, depicted in Figure 2.5, is simplistic and does not correspond to geometries used in laser scanning microscopy. In *chapter 1*, it has been already noted that the 3-dimensional microscopic resolution of TPEF microscopy emerges from the tight focusing of the illumination laser beam to a microscopic spot size. The intensity is large enough to provoke two-photon absorption, only in a restricted area around its focal center. This is the case in the SHG microscopy as well. The rigorous confinement of TPEF to a small volume stems from its quadratic dependence on excitation intensity, as eq. (1.25) implies. Inasmuch as SHG also depends quadratically on excitation intensity, as eq. (2.6) implies, it is expected that the active SHG volume, and hence the effective resolution afforded by SHG microscopy is the same as that in TPEF microscopy. This turns to be true in almost all practical cases of interest, and in general, the SHG and TPEF active volumes may be defined identically [16].

A focused beam differs from a collimated beam, not only as far as the restriction of the intensity is concerned, but also as far as its phase fronts are concerned. Its phase fronts are no longer evenly distributed along its propagation axis. This characteristic must be taken into account, when the coherent summation of the individual molecules-emitters is carried out, since the phase of the emitters is determined by the phase of the driving (focused) beam. The radiation pattern changes dramatically, and the SHG signal does not propagate on-axis anymore. In **Box 8** the mathematical description of a focused beam in the vicinity of the focal spot is given.

BOX 8: Description of a focused beam – SHG active volume –
Coherent summation of HRS from single molecules.

The electric field of a tightly focused excitation beam of angular frequency ω propagating in the z direction and polarized in the $\hat{\epsilon}$ direction may be approximated by:

$$\vec{E}(x, y, z) = -iE_\omega \exp\left(-\frac{x^2 + y^2}{w_\rho^2} - \frac{z^2}{w_z^2} + i\xi k_\omega z\right) \hat{\epsilon} \quad (2.11)$$

where w_ρ and w_z are respectively the radial and axial beam waists at the focal centers, $\hat{\epsilon}$ is a unit vector in the $x - y$ plane, k_ω is the wave vector at frequency ω , and ξ represents the effective reduction in the axial propagation vector caused by the phase anomaly, or Gouy shift [63]. In the case of relatively weak focusing ξ may be approximated by $(1 - \frac{2}{k_\omega^2 w_\rho^2})$, whereas for tight focusing this expression tends to be a slight overestimate.

The active SHG volume can be defined as :

$$\text{(1-D line distribution of molecules)} \quad V_{(1)} = \left(\frac{\pi}{2}\right)^{1/2} w_z \quad (2.12a)$$

$$\text{(2-D surface distribution of molecules)} \quad V_{(2)} = \left(\frac{\pi}{2}\right) w_\rho w_z \quad (2.12b)$$

$$\text{(3-D volume distribution of molecules)} \quad V_{(3)} = \left(\frac{\pi}{2}\right)^{(3/2)} w_\rho^2 w_z \quad (2.12c)$$

Eq. (2.12c) provides the same result for the SHG active volume, as eq. (1.27) for the TPEF active volume. The transversal and longitudinal resolution are again defined as w_ρ and w_z , correspondingly.

Eq. (2.2) provides the induced dipole moment at frequency 2ω of a single uniaxial molecule, when the driving field is linear polarized, parallel to the axis of the molecule. For the coherent summation below, we generalize, and we do not exclude other kinds of asymmetry, or other relation between the orientations of the molecules relative to the polarization of the field.

Thus, no one of the 27 elements of the tensor β is a-priori zero. The basic strategy for the coherent summation consists in averaging the molecular dipole moments over regions of the active volume, whose dimensions are small compared with the radiation wavelength, but large enough to encompass large numbers of molecules. In this way a local second-harmonic dipole moment per unit scatterer concentration is defined by:

$$\vec{\mu}_{2\omega,i}(x, y, z) = \frac{1}{2} \vec{E}_\omega(x, y, z) \sum_{j,k} \langle \beta_{ijk} \rangle \hat{\epsilon}_j \hat{\epsilon}_k \quad (2.13)$$

where $\langle \beta \rangle$ is the local ensemble-averaged unit-density hyperpolarizability. It should be noted that eq. (2.13) is the generalized form, when the molecules are arranged in a 3-D volume. In other cases the molecules may be distributed in a 2-D plane ($x-z$) or even along the axis of propagation z . We proceed, however, further with the general case.

All the molecules taken in the average at a given position (x, y, z) are driven in phase with one another, and the net local second-harmonic dipole moment per unit volume generated at this position is simply $N_{(d)} \cdot \vec{\mu}_{2\omega}(x, y, z)$, where $N_{(d)}$ is the molecular spatial density.

We consider, now, that a cell is illuminated by a laser beam, as it is depicted in **Figure 2.6**. Its membrane is labeled with push-pull chromophores, and the beam is focused with an objective of moderate numerical aperture ($NA=0.8$). The illumination is from the side, because the radiation-molecule interaction is supposed to be exclusively dipolar, and as so, it is most efficient when the principal axes of the chromophore molecules are oriented parallel to the electric-field polarization axis of the illumination beam. The SHG active area is given by eq. (2.12c), and is centered at the beam focus. Any SHG generated outside this area may be safely neglected. The SHG from the focused beam instead of propagating on-axis as in **Figure 2.5** propagates off-axis in two well-defined symmetric lobes. This may be explained again by phase-matching. Because the phase of the excitation beam has effectively been retarded near the focal center, its effective axial momentum has accordingly been decreased and can be written as ξk_ω , instead of k_ω . The latter is implied from the description of the beam, given from eq. (2.11). As before the momentum of SHG is $k_{2\omega}$. Momentum conservation along the axial direction forces SHG to propagate at an off-axis angle given by: $\theta = \pm \cos^{-1}(\xi)$.

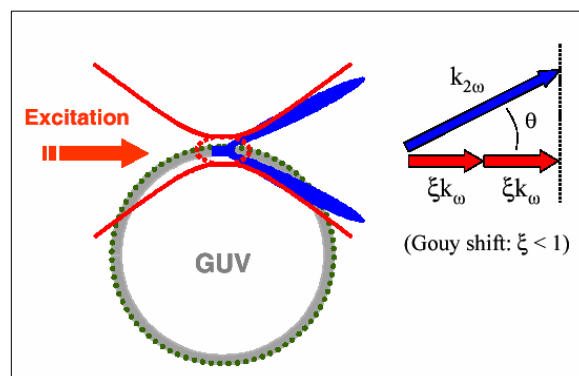


Figure 2.6: SHG from a labelled membrane when illuminated by a focused laser beam. The active SHG area is confined near the focal center. SHG propagates off-axis because of momentum conservation, taking into account the Gouy phase slippage.

2.3. Endogenous SHG

This paragraph describes SHG arising from endogenous tissue structures in biological specimen. The physical principle behind endogenous SHG is the same as in exogenous SHG, meaning that in both cases a local asymmetry in the specimen along the excitation polarization direction is required. Exogenous SHG involves asymmetries like uniaxial push-pull molecules, however, in endogenous SHG other kinds of asymmetry are mainly incorporated. These include helical geometries exhibiting “chirality”, as these geometries were identified in sugars and most amino-acids, or on a larger scale in filaments and fibrous bundles.

The organization of the most endogenous tissue structures forces us to adapt the bulk (volume) geometry, in order to properly describe endogenous SHG. Thus, the active SHG volume is provided by eq. (2.12c), since focused beams illuminate the specimens. In the previous paragraph, an analysis was carried out indicating the off-axis propagation of the SHG signal in the forward direction. The analysis was adjusted to the case of 2-D distribution of molecules. In the case of a 3-D distribution, the conclusions about the radiation pattern of the SHG are very similar. For uniformly distributed asymmetric molecules within the SHG active volume, SHG propagates in the forward direction, but also off-axis, exhibiting two well-defined lobes. However, the angular spread between the outgoing lobes is smaller, and SHG is emitted closer to axis [16].

Collagen is an extracellular protein that is the main fibrous component of skin, bone, tendon, cartilage and teeth, and can be readily be imaged with SHG microscopy [20, 21]. Though the physical origin of collagen’s remarkably high SHG efficiency has not been fully established, its non-centrosymmetric structure consisting of three intertwined polypeptide helices (**Figure 2.7**) plays very likely

a significant role [22]. Each collagen molecule has a diameter of 1.5 nm, while collagen fibrils are typically 30 – 50 nm in diameter containing therefore 30 or so, tightly packed molecules. Each molecule acts as an induced dipole, when it is illuminated by a laser beam. However, the direction of the induced dipole is not as clear as in the case of the uniaxial push-pull molecules, but in any case the resultant SHG signal arises from the coherent summation of the contributions originated from the individual collagen molecules. Since the diameter of the fibril is small compared to the typical wavelengths of the excitation beams, the collagen molecules contained in a single fibril can be considered to be excited in phase to each other. That means that the SHG signal originated from a single fibril has not a predominant propagation direction (forward or backward). However, collagen fibrils in tissue are typically not closely packed, but spaced in a loose array, so that a large number of fibrils are contained in the SHG active volume of a focused laser beam, with a particular disposition. Due to the large number of fibrils, contained in the active volume, the contributions from each fibril interfere constructively in the forward direction, whereas destructively in the backward direction [22].

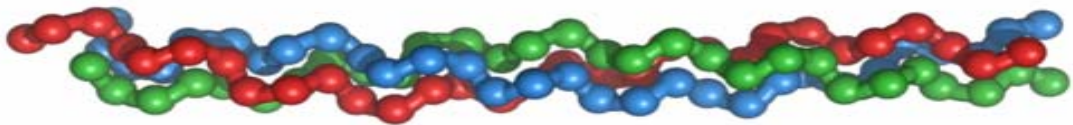


Figure 2.7: Portion of a collagen molecule. Its right-hand triple polypeptide helix is depicted.

Apart from collagen, *actomyosin assemblies* and *microtubule-based structures* exhibit high degree of organization and can be imaged using SHG microscopy. Actomyosin assemblies are the basic components of the sarcomere, i.e. of the skeletal muscle. Sarcomere is composed from myofibrils, which in turn are composed from thin and thick filaments. The thin filaments consist mainly of the

protein actin, while the thick of the protein myosin. Muscular contraction, occurs due to the movement of the myosin filament over the actin filament. Actually, the successive binding of myosin from the molecules of actin, provokes the movement of myosin over actin. The way in which the cross-bridge between actin and myosin occurs in muscle contraction, is depicted in **Figure 2.8**. Actomyosin assemblies are consisted of coiled-coil multiple helices and have a characteristic asymmetry, leading to SHG efficiency [23, 24].

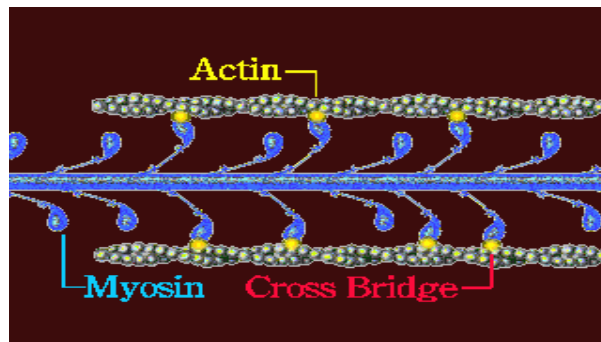


Figure 2.8: Cross-bridge formation in muscle contraction. The bridged actin (thin) and myosin (thick) filaments are referred to as actomyosin assemblies. They exhibit particular SHG efficiency.

In our work, SHG originated from actomyosin assemblies in *C. elegans*, plays a central role. Owing to that, these assemblies will be referred further in the experimental part of this work.

Microtubule-based structures, on the other hand, do not consist of coiled-coil multiple helices, they exhibit, however, a characteristic asymmetry, and are efficient for SHG [25]. Microtubules are formed from two protein groups: α -tubulin and β -tubulin. Centrosomes are representative well-organized microtubule structures. In *C. elegans*, centrosomes in early embryonic cells have been imaged by SHG [23].

3.1 Third Harmonic Generation

As it has already mentioned SHG and THG are scattering phenomena that are constrained to propagate along the same direction as the driving field. While Second Harmonic Generation requires a medium without inversion symmetry, Third Harmonic Generation can be produced in every medium. Unlike SHG, it is limited to the observation of noncentrosymmetric media such as crystals or structured media. In case of THG, 3 photons are acquired for the excitation from a low energy level to a level of higher energy. During deactivation, a photon of triple energy in comparison with the fundamental beam is emitted. This assumes the existence of three virtual states.

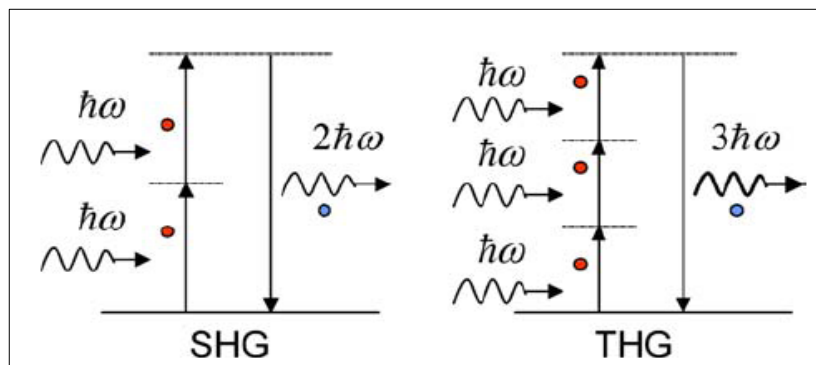


Figure 3.1: Energy level diagrams describing Second Harmonic Generation (on the left) and Third Harmonic Generation (on the right). [26]

SHG and THG can be visualized by considering the interaction in terms of exchange of photons between various frequencies of the fields. According to this picture, which is illustrated in **Fig.3.1**, two or three photons of angular frequency ω are destroyed and a photon of angular frequency 2ω (for SHG) or 3ω (for THG) is simultaneously created in a single quantum-mechanical process. The solid lines in the figure represent the atomic ground states, and the dashed lines represent what are known as “virtual” levels. These virtual levels are not energy

levels of the atoms, but rather represent the combined energy of one of the energy states of the atom and one or more photons of the radiation field.

Due to its virtual level transition characteristic, higher harmonic generation is known to leave no energy deposition to the interacted matters, since no transition involves and the emitted photon energy is exactly the same as the total absorbed photon energy, also referring as the energy conservation law. This virtual-transition and energy conservation characteristics provide the optical “noninvasive” nature desirable for microscopy applications, especially for live specimen imaging.

Optical third-harmonic generation (THG) is generally a weak process but is dipole allowed, therefore it occurs in all materials with inversion symmetry. When using focused high intensity ultrashort laser pulses, this normally weak THG process becomes highly operative at a simple air-dielectric interface and is much stronger than the bulk of most materials. This non-linear optical response at interfaces is characterized as a phenomenological surface-enhanced THG in transmission or in reflection. This surface THG is further cascaded in transmission or reflection from layered composite dielectric materials of a high-low index of refraction, resulting in a marked increase in photon conversion efficiency than that of a single interface. It is important to note that the surface-enhanced optical THG is a fundamental physical process occurring at all interfaces and is relatively free from the constraint of a phase-matching condition and wavelength restriction. Using optical THG at an interface, it becomes possible to generate wavelengths at which harmonic crystals are unavailable.

[27]

Consider a laser beam propagating in the z direction and tightly focused into a sample. Using the theory of harmonic generation with focused Gaussian beams, we can calculate the intensity of the third harmonic light:

$$P^{(3)}(3\omega) = \frac{1}{4} \varepsilon_0 \chi^{(3)}(3\omega) E^3(\omega) \quad (3.1)$$

Where $\chi^{(3)}$ is the third-order susceptibility tensor, responsible for the third harmonic generation. The third order polarization $P_{3\omega}$ has a third order dependence from P_ω . In the case of a tight focused Gaussian beam the power of third harmonic can be expressed as: [27]

$$P_{3\omega} = k_{3\omega} k_\omega \left(\frac{4\pi}{n_{3\omega} n_\omega^2 c} \right)^2 P_\omega^3 |J|^2 \quad (3.2)$$

Where J is the integration:

$$J = \int_{-\infty}^{+\infty} \frac{\chi^{(3)}(z) e^{i\Delta k b z} dz}{(1 + 2iz)^2} \quad (3.3)$$

In the equation above, the integration extends over the volume of the medium, where $b = k_\omega w_0^2$ is the confocal parameter, the axial width of the focal field distribution. k_ω is the wave vector at the fundamental wavelength, w_0 is the beam waist radius and $\Delta k = 3k_\omega - k_{3\omega}$ is the phase mismatch. The calculation of this integration shows that efficient THG signal in a uniform medium with a tight focused laser beam is possible only for $\Delta k > 0$. Due to the phase factor $e^{i\Delta k b z}$, the integral is zero for uniform, infinite, normally dispersive media ($\Delta k < 0$), and even for perfect phase matching ($\Delta k = 0$) the efficiency of THG vanishes. [28]

Hence, in normally dispersive materials where $\Delta k < 0$, third harmonic generation is impossible. However, when the medium is not uniform, i.e when there is an interface either in refractive index or in the third-order non linear susceptibility $\chi^{(3)}$, significant THG can be observed. The need for negative phase mismatch can be understood if we remember that a focused beam contains a collection of wave vectors with different orientation. Three such wave vectors contribute to the $k_{3\omega}$, only when $k_{3\omega} \leq 3k_{\omega}$.

When the nonlinear medium is not homogeneous, either in the refractive index or in the third order non-linear susceptibility $\chi^{(3)}$, the THG signal does not vanish, and significant output of THG can be observed. For example, near the interface in between two media, which have the same linear refractive index but different non linear susceptibility, assuming that $\Delta kb < 1$, we find that:

$$P_{3\omega} = \delta\chi^2 (1 + 4z^2/b)^{-1} \quad (3.4)$$

where $\delta\chi$ the difference in susceptibility values and z is the distance between the interface and the beam waist. Hence, as this interface is scanned along the optical axis the THG signal is generated efficiently when the interface is near the beam waist. The signal peaks when the interface is at the beam waist position, and its full-width at half-maximum (FWHM) is b . When the linear index and the phase mismatch are also discontinuous at the interface, the beam parameters change across the interface, but the third harmonic is still generated efficiently only when the interface is located within one confocal parameter of the focal plane. Similarly, a thin film with a thickness $t \ll b$ embedded in a homogeneous medium will generate a THG signal with

$$P_{3\omega} \propto \delta \chi^2 (t/b)^2 (1 + 4z_\omega^2/b^2)^{-2} \quad (3.5)$$

The signal is generated only when the film is near the focal plane, now with a FWHM of $0.64b$. [29]

Since the efficiency of THG scales with the third power of the excitation power, it is, for a given input power, inversely proportional to the square of the input pulse duration. Hence, there is a clear advantage in using ultrashort pulses for THG imaging.

$$I(3\omega) \propto |\chi^{(3)}|^2 I^3(\omega) \quad (3.6)$$

According to Eq: $P(2\omega) = \frac{1}{2} \varepsilon_0 \chi^{(2)}(2\omega: \omega, \omega) E(\omega) E(\omega)$ the generated SHG intensity depends on the square of the incident light intensity, while generated THG intensity will depend on the cubic of the incident light intensity. Similar to 2PFM, SHG and THG microscopy provides superior axial resolution due to quadratic and cubic dependencies of the signals on the illumination intensity. Usually the third-order non linear susceptibility $\chi^{(3)}(3\omega: \omega, \omega, \omega)$ responsible for THG is much weaker than the second-order nonlinear susceptibility $\chi^{(2)}(2\omega: \omega, \omega)$ responsible for SHG, thus THG is harder to observe. However, not all materials have second-order nonlinear susceptibility. For centro-symmetric media, the lowest order nonlinear susceptibility will be $\chi^{(3)}$ instead of $\chi^{(2)}$. Random distribution of biomolecules and suborganelles inside tissues and cells create optical centro-symmetry in the optical wavelength (0.4-1 μ m) scale, thus inhibiting SHG. On the other hand, all materials allow the creation of third-order susceptibility, of which the magnitudes vary according to material properties and wavelengths.

BOX 9: Description of THG in the case of a tight focused beam.

THG is related to the creation of a third-order nonlinear polarization (at 3ω angular frequency) according to: [30]

$$P(3\omega) = \frac{1}{4} \varepsilon_0 \chi^{(3)}(3\omega : \omega, \omega, \omega) E(\omega) E(\omega) E(\omega) \quad (3.7)$$

Where $\chi^{(3)}(3\omega : \omega, \omega, \omega)$ represents the third-order non-linear susceptibility responsible for THG.

In the process, the optical field at the fundamental wavelength (E_ω) induces a macroscopic polarization ($P_{3\omega}$) of the form

$$P_{3\omega} \propto \chi^{(3)} E_\omega^3 \quad (3.8)$$

Which in turn generates a field at the third harmonic frequency ($E_{3\omega}$). It follows that the THG power, $P_{3\omega}$ has a third – order dependence on the incident power, P_ω [31]

$$P_{3\omega} \propto [\chi^{(3)}]^2 P_\omega^3 \quad (3.9)$$

The THG power in the case of strong focusing of a Gaussian beam can expressed as

$$P_{3\omega} \propto P_\omega^3 |J|^2 \quad (3.10)$$

Where

$$J = \int_{-\infty}^{\infty} \frac{\chi^{(3)}(z) e^{i\Delta k b z} dz}{(1 + 2iz)^2} \quad (3.11)$$

Here $P_{3\omega}$ is the fundamental beam power, $\chi^{(3)}(z)$ is the third order susceptibility, $\Delta k = 3k_\omega - k_{3\omega}$ is the phase mismatch, b is the confocal parameter. The spatial coordinate z is measured in units of b .

Due to the phase factor $e^{i\Delta k b z}$, the integral is zero for uniform, infinite, normally dispersive ($\Delta k \leq 0$) media, and there is no THG in this case. If one omits the case of anomalous dispersion, THG can only be generated in media with spatial change in refractive index or third order susceptibility. It is straightforward that big changes in the refractive index and third order susceptibility are expected to occur on interfaces between different media.

3.2 THG applications

Optical higher harmonic generation, including second harmonic generation and third harmonic generation, leaves no energy deposition to its interacted matters due to an energy-conservation characteristic, providing the “noninvasiveness” nature desirable for biological studies. Combined with its nonlinearity, higher harmonic generation microscopy provides excellent three-dimensional (3D) sectioning capability, offering new insights into the studies of embryonic morphological changes and complex developmental processes. By choosing a laser working in the biological penetration window, a non-invasive in vivo light microscopy with sub-micron 3D resolution and millimetre penetration, utilizing endogenous higher harmonic generation signals in live specimens has been achieved.

The primary contrast mechanism in THG microscopy is related to sub-focal volume inhomogeneities in the optical properties of a biological sample. Under tight focusing conditions, the extent of THG increases dramatically when the focus spans an interface between two optically different materials. This allows imaging based on THG to resolve otherwise transparent interfaces and inhomogeneities within the resolution of the confocal parameter and without the use of dyes. THG has been used to image mitochondria, red blood cells, embryonic development, neurons, plasma flows, muscle fibers, skin biopsy samples, and most recently large intracellular lipid vesicles. [29]

Furthermore, non-invasive imaging was performed in live zebrafish (*Danio rerio*) embryos. The complex developmental processes-within >1mm-thick zebrafish

embryos can be observed *in vivo* without any treatment. No optical damage was found even with high illumination after long-term observations and the examined embryos all developed normally at least to the larval stage. The excellent 3D resolution of the demonstrated technology allows the capture of the subtle developmental information on the cellular or subcellular levels occurring deep inside the live embryos and larvae. This technique can not only provide *in vivo* observation of the cytoarchitecture dynamics during embryogenesis with submicron resolution and millimetre penetration depth, but would also make strong impact in developmental and structural biology studies. [29]

Additionally, third harmonic generation microscopy is used to make dynamical images of living systems. Chara plant rhizoids have been imaged, showing dynamic plant activity, and non-fading image characteristics even with continuous viewing, indicating prolonged viability. In addition, another dependency of the third harmonic was revealed: the image contrast varied according to the relative orientation of the interface within the focus with respect to the excitation beam's direction of propagation. [32, 33]

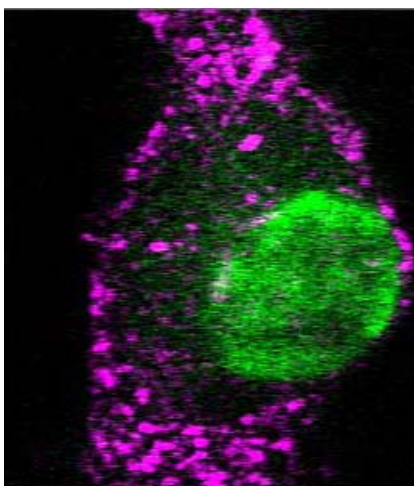


Figure 3.2: Combined images of TPEF (green) and THG (purple) of a fixed neuron. The cell nucleus was labelled with DAPI (maximum excitation at 350 nm, maximum emission at 450 nm). The two data channels were combined for false-color images (purple for THG and green for TPEF).

Combined image of THG and TPEF of a fixed neuron is presented in figure 3.2.

The THG and the TPEF appear quite complementary: the THG signal from the

nucleus comes only from the nucleolus (which can be noted in Fig. 3.2) and the TPEF from the DAPI is generated mainly at the nucleus. The nucleolus cannot be resolved by the TPEF image only. The THG image is shown here to provide the general shape of the cell as a frame of reference in which specific fluorescence labelling is used. All this can be done in a single scan of a single laser beam. Adding the THG imaging capability to these microscopes involves only adding a detection path in the forward direction for the detection of the UV third-harmonic signal. The most important advantage of this method is that it is possible to perform third-harmonic and two-photon excitation fluorescence (TPEF) imaging with a single laser source. Using a single laser source is most desirable for some reasons: first, the problem of chromatic aberration does not exist and therefore the third harmonic and the TPEF are generated exactly at the same depth. Second, the microscope system and its alignment are most simplified using only one laser beam and, by using two separate collection paths, in the forward direction for the THG and in the backward direction for the TPEF, a single scan is sufficient to provide the combined image.

In the current work the simultaneously collection of two non-linear optical signals from *C. elegans* mutants was achieved, by detecting third Harmonic Generation (THG) signals in the forward direction and TPEF images in the backward direction. By employing this configuration complementary information about the structure and function of our biological sample have been extracted.

4.1 The biological samples

In our study, the biological specimen under investigation was the nematode *Caenorhabditis elegans* (*C. elegans*). We used the nematode *Caenorhabditis elegans* to exploit the capacity of combined non-linear optical imaging to provide specific structural and functional information related to anatomical features and cellular processes of our model biological system.

The developed nonlinear microscope can be used in a variety of studies in the field of physics, biophysics and medicine. One main research target comprises the investigation of the molecular and physiological processes, underlying the neuronal function of *C. elegans* samples. For this reason, a brief presentation of the nematode is necessary.

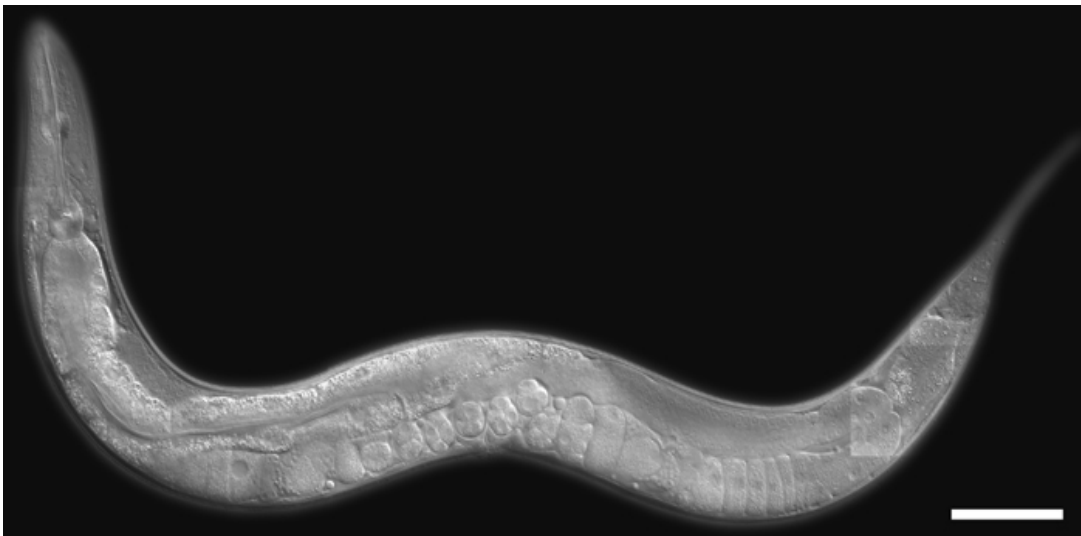


Figure 4.1: Photograph of an adult *C. elegans* with the use of Nomarski microscope. The length of the nematode is about 1 mm, and the width is about 80-100 μm .

C. elegans is a small (1 mm) free-living hermaphroditic nematode that completes a life cycle in 2.5 days at 25°C. A photograph of *C. elegans* is shown in **Figure 4.1**. The simple body plan and transparent nature of both the egg and the cuticle

of this nematode have facilitated an exceptionally detailed developmental characterization of the animal.

Serial section electron microscopy has identified the pattern of synaptic connections made by each of the 302 neurons of the animal (including 5000 chemical synapses, 600 gap junctions, and 2000 neuromuscular junctions), so that the full “wiring diagram” of the animal is known [34].

C. elegans has been established as an ideal model organism for neurobiology studies. The nematode nervous system comprises 302 neurons whose pattern of connectivity has been completely mapped out [35]. This relative simplicity has been used for studying sensory processing and the neural coding of behaviour. Most studies in this area have concentrated on identifying the specific neurons and molecules involved in generating behavioural responses to chemical, mechanical and thermal stimuli. Individual neurons can be easily identified by transgenic animals using cell-specific markers such as fluorescent proteins. By recording simultaneously the three nonlinear signals described previously (TPEF-SHG-THG) cumulative information about the biological sample can be obtained. Due to their specific nature, these signals are generated by different structures and molecules of the animal. The capacity for three-dimensional (3D) reconstruction of a live organism will facilitate the detailed description of anatomical features of both wild type and genetically modified animals. Such reconstructions may contribute to the understanding of the molecular mechanisms pertinent to specific genetic alterations.

C. elegans embryos are particularly suitable for differentiation and morphogenesis analysis. Fertilized eggs move down the uterus and out through the vulva, continuing development outside the uterus. Newly hatch larvae have

588 cells and additional divisions of somatic blast cells occur during the four larval stages eventually giving rise to 959 somatic cells. Besides the reproducibility and speed of its development, additional advantages of *C. elegans* are its transparency and its small size, so it fits within a high magnification microscope field. To identify the role of a specific cell type, targeted killing has been used extensively. This process can be performed by laser ablation microsurgery or by genetic means (cell-specific expression of cytotoxic agents). By combining the THG capabilities of 3D imaging with long term measurements (3 to 6 hours) it is possible to visualize and map cell division and development in living embryos, larvae and adults.

The Sample

Five different strains and transgenic *C. elegans* samples have been investigated: Wild type, mutants expressing GFP (membrane localized or cytoplasmic) in mechanoreceptor neurons, mutants expressing diffuse GFP in the pharyngeal cytoplasm and expressing diffuse DSRED in the head and motor neurons. We followed standard procedures for *C. elegans* strain maintenance, crosses and other genetic manipulations [34]. Nematode rearing temperature was kept at 20°C. Before each experiment, young adult animals were anaesthetized by immersing to 0,5M of sodium azide (NaN₃), and subsequently mounted on glass slides. The samples were prepared at IMBB at the laboratory of Dr N. Tavernarakis.

5.1 Experimental apparatus

The experimental set-up is outlined in **figure 5.1**. The laser used is an Amplitude Systems t-pulse laser operating at 1028 nm. This source is a compact diode-pumped femtosecond laser oscillator delivering a train of highpeak power, short duration pulses. The average power of the laser is 1 Watt, with pulse duration of less than 200fs and a repetition rate of 50MHz. The Amplitude femtosecond laser system emitting at 1028 nm employed for the realization of the non linear measurements due to the advantage that its third harmonic signal is in the near ultraviolet (UV) part of the spectrum. Consequently, there is no need to use UV optics with special coatings for the collection of the THG signal. Additionally, by employing this wavelength (1028nm) the absorption of the water, which leads to unwanted thermal heating of the biological samples, is constrained.

The beam is directed to a modified optical microscope (Nikon Eclipse ME600D) using suitable dichroic mirrors, and is focused tightly onto the sample by an objective lens with high numerical aperture (Nikon 50X N.A. 0.8). The average laser power on the specimen is 30mWatt (0.6 nJ per pulse). No damage in the sample is appreciated at this power. A CCD camera (PixaLINK PL A662) is used for observation. Biological samples are placed between two round glass slides (*Marienfeld 0.06mm-0.08mm*) that fit into a motorized xyz translation stage (Standa 8MT167-100) by employing a special holder. The minimum step of the stages in each direction is 1 μm .

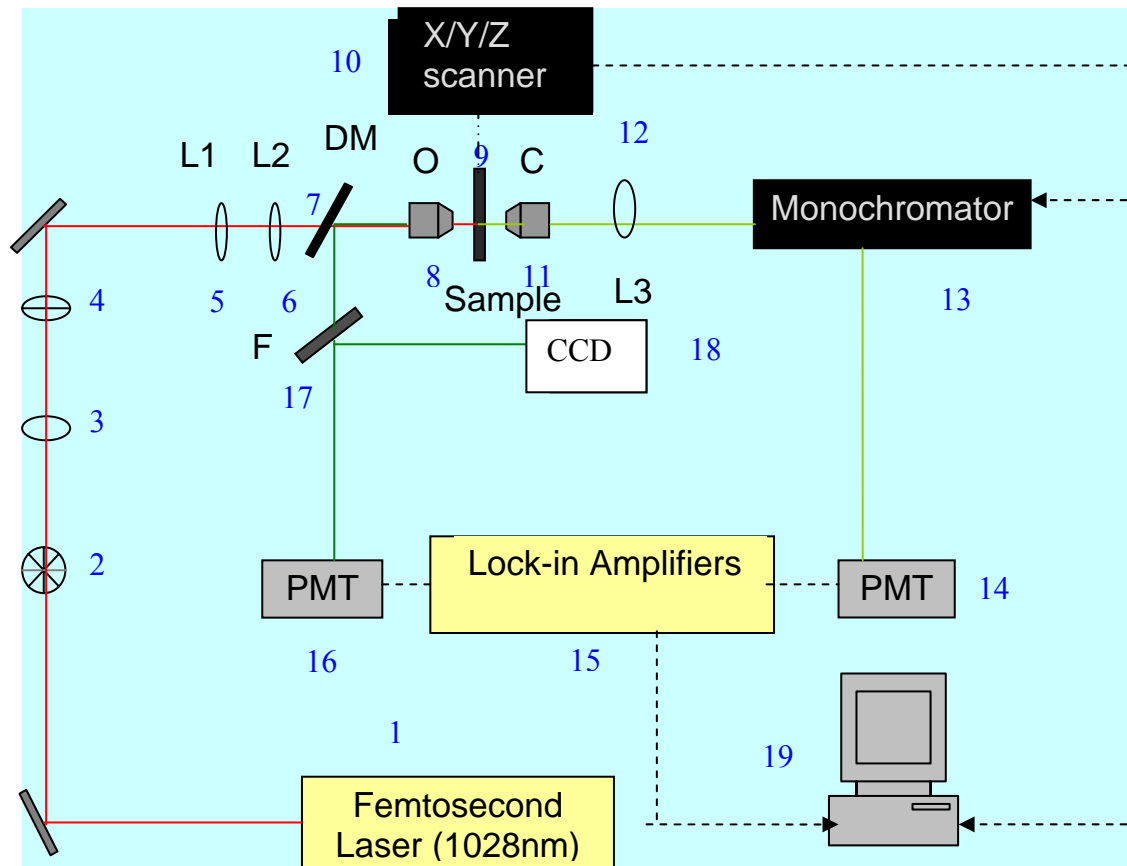


Figure 5.1: Experimental set-up for combined TPEF and SHG or THG microscopy. 1) Femtosecond laser ($\lambda=1028\text{nm}$), 2) chopper, 3) Iris, 4) attenuator, 5), 6) lenses, 7) Dichroic mirror, 8) Objective lens, 9) Holder of the sample, 10) x-y-z motorized scanning stages, 11) Condenser lens, 12) lens, 13) Monochromator, 14) Photo-multiplier tube, 15) Lock-in amplifiers, 16) PMT, 17) Flip-mount mirror, 18) CCD camera, 19) P.C.

Two signals are collected simultaneously, TPEF in the backward and THG or SHG in the forward direction, by tuning the monochromator. The system is completely automated and controlled with a LabView interface.

The induced losses of the emitted THG signals, due to the thin cover slips which are used to mount the biological samples, are constrained. This configuration limits the resolution to $1\mu\text{m}$, but allows scanning bigger areas, without aberration due to the edges of the aperture of the objective. The average accumulation time in every step is 30msec.

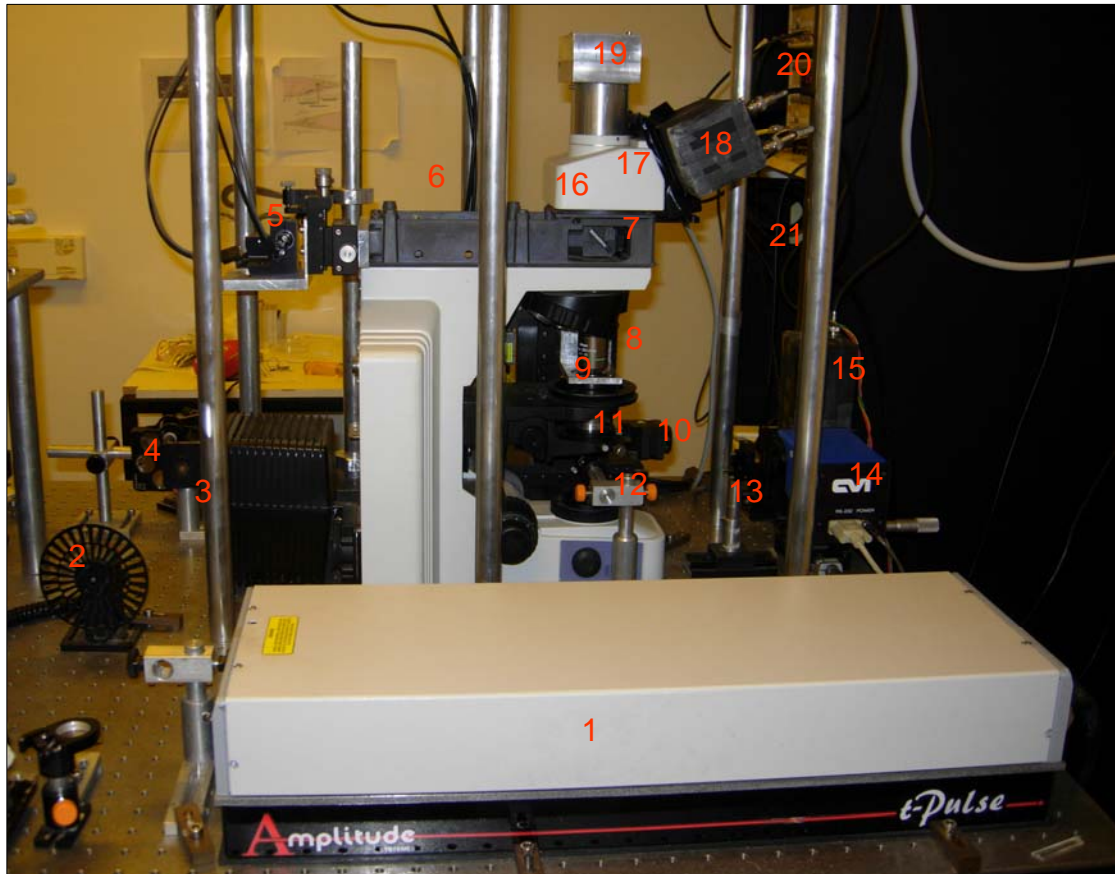


Figure 5.2: Photograph of the experimental setup for combined TPEF-SHG-THG scanning microscopy. The setup is placed on an optical table (Newport). The components, depicted in figure 5.1 that are visible on the above picture have been numerated.

TPEF signals are collected in the backward direction using a photomultiplier tube (PMT Hamamatsu R4220) connected to a Lock in Amplifier (SR810 Stanford Research Systems). The use of a Lock in Amplifier provides a very good noise rejection, and measurements can be performed in less stringent lighting conditions. The photomultiplier tube is attached at the position of the microscope eye-piece. A short pass filter (SPF 650nm CVI) is placed at the photomultiplier input to cut off the reflected laser light. Furthermore, a high pass filter (HPF 520nm CVI) is used for the elimination of reflected SHG and THG signals. For thin samples, most of SHG and THG signals propagate with the laser and are collected and collimated by employing a common condenser lens (Carl Zeiss Plan-Apochromat 100X N.A. 1.4 oil immersion). A dichroic mirror

(Enhanced Aluminium Mirror, Thorlabs) is used to reflect the transmitted beam. The signals are focused by means of a lens (UV Fused Silica Plano-Convex, Thorlabs) into the slit (100 μ m) of a monochromator. The focal length of the lens is 3 cm. The monochromator (Digikrom CM110 CVI) consists of two gratings (1200 grooves/mm each).

The first one is suitable for visible light (maximum efficiency 80% at 500nm) and the second is appropriate for ultraviolet light (maximum efficiency 72% at 300nm). The resolution of the monochromator is 1nm. For the detection of signals, a photomultiplier tube (PMT Hamamatsu R636-10) connected to another Lock-in Amplifier is used. With this configuration, it is possible to record SHG and THG signals in distinct sets of measurements by tuning the monochromator in different spectral regions. By detecting SHG or THG images in the forward direction and TPEF images in the backward direction, our experimental apparatus allows the collection of two non-linear optical signals simultaneously.

5.2 Experimental results

To demonstrate the performance of the t-pulse laser operating at 1028 nm as a photon source for THG measurements with biological samples at the microscopic level, different body parts of wild type *C. elegans* were imaged. As mentioned previously, the THG signal is generated at the interface between different media that break the axial symmetry of focus. That allows recording of THG signals arising from the worm body surface and from boundaries between organs tissues and cells. We find that specific organs generate strong signals that reveal novel structural information about the anatomy of the nematode.

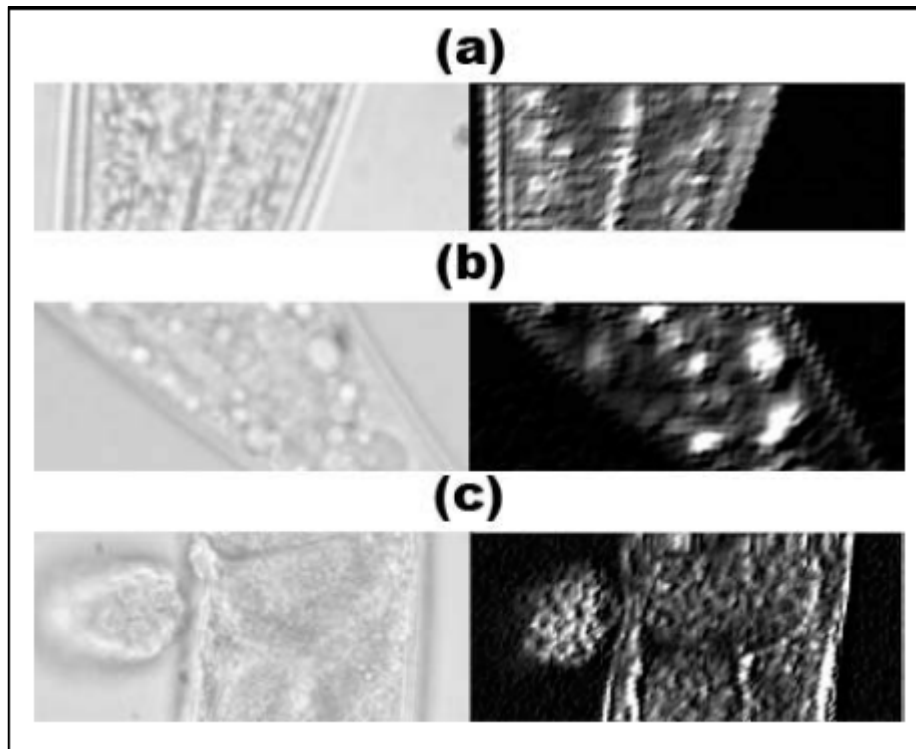


Figure 5.3: (a) THG image of the pharynx region of a wild type worm. (b) THG image from the posterior end, (c) the uterus region of the worm.

Figure 5.3(a) depicts the THG image of the pharynx region of a wild type animal. **Figure 5.3(b)** shows the THG image from the posterior end and **figure 5.3(c)** shows the uterus region of the worm. A light-transmission picture of the scanned region is included for reference. The dimensions of the scanned area were $61 \times 21 \mu\text{m}^2$, $51 \times 25 \mu\text{m}^2$ and $121 \times 55 \mu\text{m}^2$, respectively. Signals were recorded in the forward direction, as described previously. The monochromator was tuned at 343nm. Thus, detection was performed in a spectral region where the only detectable signal is contributed by THG. Each scan was performed in a specific z position where the THG signal that arises from the sample was maximal.

From **figure 5.3**, the shape and contour of the worm as well as the internal tissue and organ arrangement, can be observed with satisfactory resolution. It is

feasible the collection of strong THG signals originate from the body surface, the pseudocoelomic cavity and the boundaries between internal organs of the worm, due to abrupt changes of the refractive index values (**fig.5.3(a)**). This indicates constitution differences between different tissues. The collected THG signals from the pharynx are minimal. Similar characteristics can be seen in **figure 5.3(b)**. The outline of the worm tail is clearly visible. High THG signals were generated by discontinuities in the region of the tail. These discontinuities are likely due to lipid depositions [45] or formations of discontinuous refractive index in the intestine and pseudocoelomic cavity. The central part of the worm is shown in **figure 5.3(c)**. Three eggs are also shown, two inside the uterus and another in the vicinity of the animal. The contours of individual cells inside the external egg are detectable through THG measurements. No THG signal is recorded from the left part of the external egg, which appears slightly defocused in the light-transmission picture, demonstrating the sectioning capabilities of THG measurements. We note that the signals are obtained without the use of labeling molecules.

As shown previously, THG is a general purpose technique that provides structural information about the sample, but is not capable to provide information on specific stained molecules. In order to improve and expand the imaging capacity of our microscope we sought to combine THG measurements with complementary nonlinear techniques. Due to their specific nature, the three nonlinear signals described above (TPEF-SHG-THG) are generated by different structures and molecules in the animals. By recording simultaneously these three nonlinear modalities, cumulative information about the biological sample is obtained. The use of an excitation wavelength of 1028 nm allows us to record all

three signals with a single laser, simplifying the layout of the set-up. Additionally, with this configuration, we ensure that produced signals correspond to the same optical section.

Figure 5.4 depicts the non linear imaging (TPEF-SHG-THG) of the *C. elegans* anterior part. In these transgenic animals, GFP is expressed in the cytoplasm of the pharyngeal muscle cells. The pharynx is a muscular organ that pumps food into the pharyngeal lumen, grinds it up, and then transfers it into the intestine.

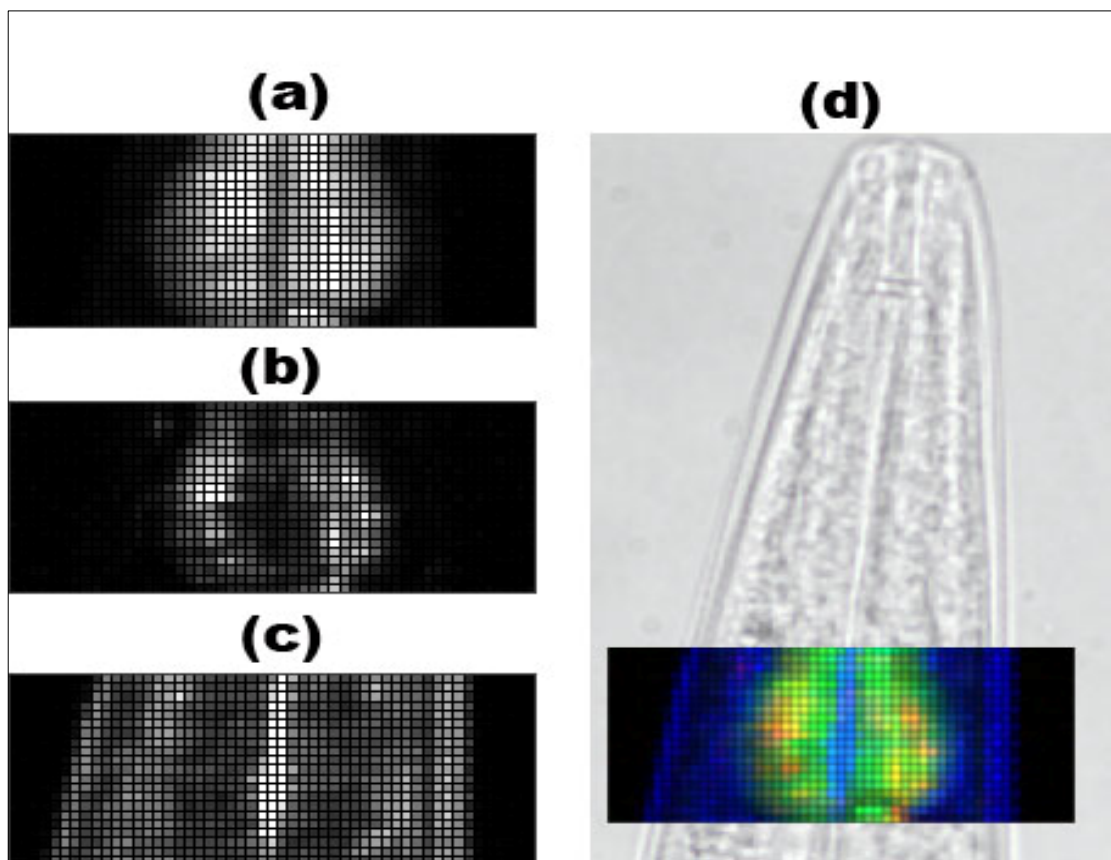


Figure 5.4: Non-linear signals generated in the pharynx region of a worm expressing GFP in the pharyngeal muscles: (a) TPEF (b) SHG (c) THG and (d) multimodal image obtained by the combination of the previous three: TPEF (green), SHG (red) and THG (blue). Note all images are raw data – no image processing has been performed only an artificial colour look up table has been used to assign a value to the image intensity.

The dimensions of the scanned region were $51 \times 21 \mu\text{m}^2$. Scanning was performed at a specific z position where the collected TPEF signal derived from

the pharynx became maximum. **Figure 5.4(a)** shows a TPEF image, obtained by backward detection, while **figures 5.4(b)** and **5.4(c)** show the SHG and THG measurements respectively, detected in the forward direction. SHG and THG measurements were performed in different sets by tuning the monochromator at 514 nm and 343 nm, respectively. There are main peaks at 514 nm (SHG) and 343 nm (THG) which abruptly reduce, as the monochromator setting was changed 3-4 nm around these wavelengths. These observations are in perfect agreement with the spectral distributions, which present the non-linear phenomena of *Second Harmonic and Third Harmonic Generation*. Moreover it is worth mentioning that by placing a 514nm interference filter (CVI F03-514.5) or a 340nm band pass filter (UQG Hoya U 340 UV transmitting Vis and IR absorbing) in the forward detection scheme, the recorded SHG or THG images from the nematode respectively are similar with the ones obtained without the filters.

Consequently, the contribution of the higher diffraction orders of the fundamental beam, due to the use of gratings, can be safely excluded from the detected signals. The combination of the three contributions is shown in **figure 5.4(d)** (TPEF in green, SHG in red and THG in blue). By TPEF imaging of the GFP molecules in pharyngeal muscles, we are able to visualize the inner part of the pharynx. The endogenous structures of well-ordered protein assemblies in the pharyngeal muscles, such as actomyosin complexes, are the main contributors to recorded SHG signals [46,47,48,49]. GFP is expressed under the control of the myo-2 promoter in animals used for this experiment. The myo-2 promoter is specific to the pharynx and GFP expression is limited to the cytoplasm of pharyngeal muscle cells. GFP molecules, due to their random orientation in the

pharynx region do not contribute to the SHG signal. The contour and shape of the worm can be observed through THG measurements. Furthermore, high THG intensity signals were collected from the linings of the animal pseudocoelomic cavity. The three image modalities provide complementary information about the biological sample, as seen in **figure 5.4(d)**. This is due to the fact that individual, induced signals come from different components. Diffuse GFP molecules are the main source of the detected TPEF signals. The endogenous oriented structural proteins are responsible for the observed SHG signals. Unique structural and functional information can be obtained by recording THG signals, given the sensitivity of these signals to changes of the refractive index of the medium.

Figure 5.5 depicts the non linear imaging (TPEF-SHG-THG) of the *C.Elegans's* interior part. In these transgenic animals, GFP is expressed again under the control of the *myo-2 promoter*. The *myo-2 promoter* is specific to the pharynx and GFP expression is limited to the cytoplasm of pharyngeal muscle cells. The dimensions of the scanned region were $60 \times 25 \mu\text{m}^2$, $60 \times 30 \mu\text{m}^2$ and $60 \times 25 \mu\text{m}^2$, with $1 \mu\text{m}$ resolution. In order to get valuable information scanning was performed over different animals at specific positions.

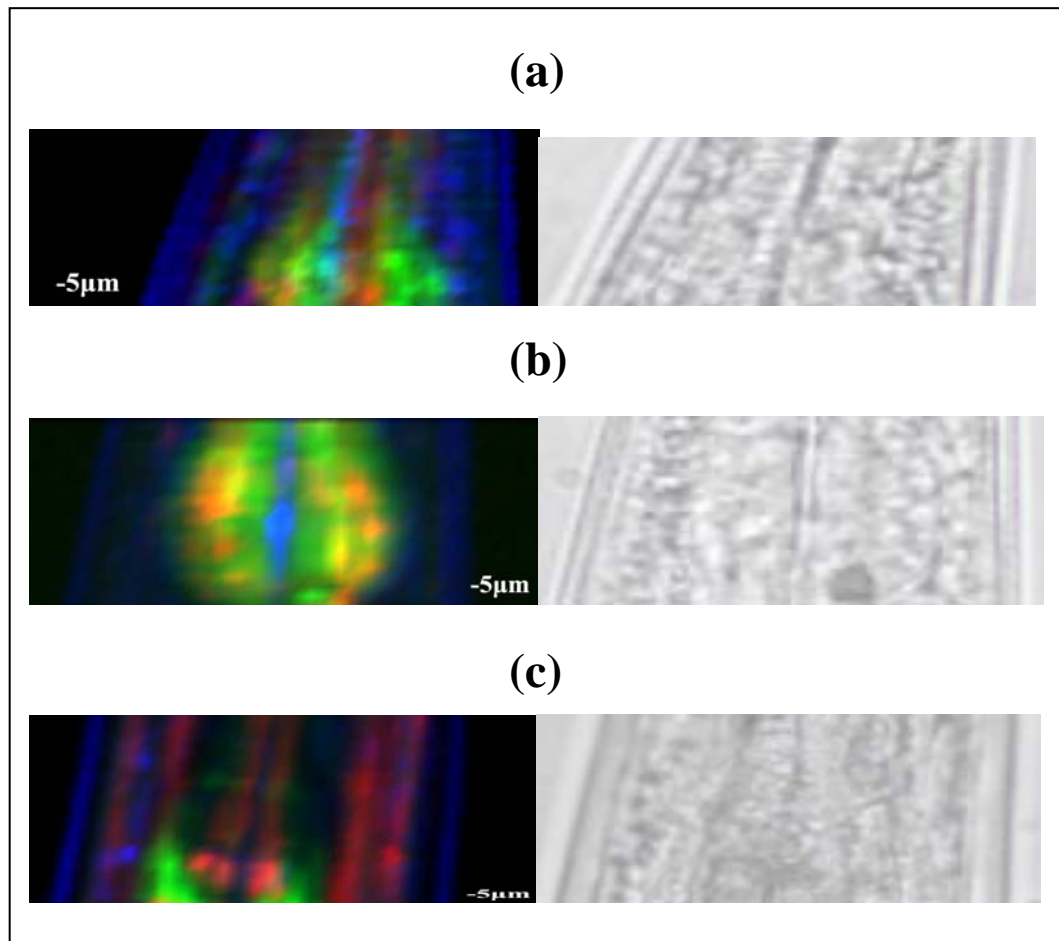


Figure 5.5: Multimodal image obtained by the combination of TPEF (green), THG (blue) and SHG (red) from *C. elegans* expressing GFP in the pharynx cytoplasm.

On the left part, the combination of the three contributions (TPEF in green, SHG in red and THG in blue) is shown. On the right hand, we also include the light-transmission picture corresponding to the same region. That will allow us to detect the sources of the different effects. By TPEF imaging of the GFP molecules in pharyngeal muscles, it is possible to visualize the inner part of the pharynx. Although the spatial resolution of this set-up is limited by the minimum step of the scanning stage (1 μm), the body wall of the worm as well as the internal tissue and organ arrangement can be observed with satisfactory resolution, through THG signal. In contrast, the fluid filled body cavity that separates the body wall from internal organs does not contribute to the THG.

Then, the contour and shape of the worm can be observed through THG measurements. Furthermore, high THG intensity signals were collected from the linings of the animal pseudocoelomic cavity (**Figure 5.5(a),(b)**), while no signal arise from the pharyngeal muscle. These findings are in perfect agreement with our previous measurements (**Figure 5.3** and **5.4**). Food particles trapped in the sieve (**Figure 5.5(a)**) in the metacarpus or anterior bulb and the grinder (**Figure 5.5(b)**) in the terminal bulb also generates great signal. The sieve traps food particles while fluid is expelled by the pharyngeal channels. The grinder has a function of macerating the food and as a valve to regulate one-way ttraffic of food into the intestine.

Highly ordered structures generate a high level of SHG signal. The endogenous structures of well-ordered protein assemblies in the pharyngeal muscles, such as actomyosin complexes, are the main contributors to recorded SHG signals [46,48,49] in **figure 5.5(c)**, where the structure of the longitudinal somatic muscles can be clearly visualized. The oblique somatic muscles contain many sarcomeres repeating in regular order in one cell. In **figure 5.5(a)** and **5.5(b)** the SHG arise from the interior part pharyngeal muscle. Pharyngeal muscles are formed by non striated muscles, containing a single sarcomere. The first five layers of muscles are radial oriented filaments attached medially to the cuticle of the lumen and laterally to the pharyngeal basal lamina.

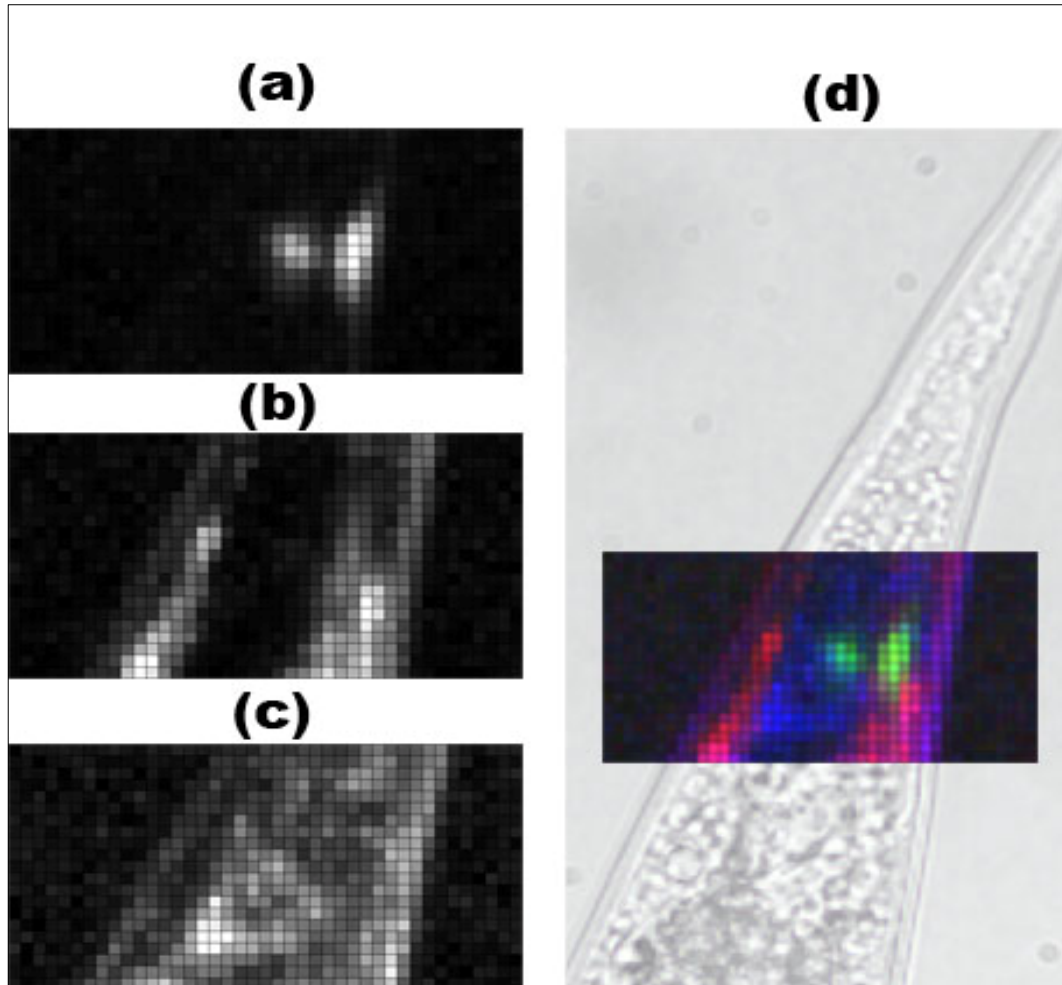


Figure 5.6: Non-linear signals generated at the tail of an animal expressing GFP in the mechanoreceptor neurons: (a) TPEF (b) SHG (c) THG and (d) multimodal image obtained by the combination of the previous three: TPEF (green), SHG (red) and THG (blue).

Figure 5.6 depicts non linear imaging (TPEF-SHG-THG) of the posterior part of a sample. In these experiments, GFP is expressed under the *mec-4* touch-cell specific promoter and is localized in the cytoplasm of the six mechanoreceptor neurons of the animal. Two of the six mechanoreceptor neurons are located in the posterior part of the worm, usually in different z positions. These two touch receptor neurons (PLML – PLMR) do not overlap with the gut. They are situated close to the tip of the tail, away from the autofluorescent gut. The dimensions of the scanned region were $41 \times 21 \mu\text{m}^2$. Scanning was performed at a specific z position, where the TPEF signal emanating from one neuron was maximum.

The recorded TPEF signal arises from cytoplasmic GFP molecules, which are expressed in the six neurons. It is clear that the precise localization of the two touch receptor neurons, which are positioned near the tail, is feasible by processing of the obtained images (figure 5.6(a)). The SHG image enabled us to detect muscles close to the tail of the worm. Endogenous structural proteins (actomyosin complexes) are the main contributors to the recorded SHG signals. [46,48] GFP molecules in the neuronal cell are symmetrically distributed. Therefore, their contribution to the observed SHG signal is expected to be minimal. This is in agreement with experimental data, since it was not possible to detect the neuronal cells, as depicted in **figure 5.6(b)**. In **figure 5.6(c)** the morphology and the contour of the worm can be observed through THG measurements. Rather, discontinuities (such as sub-cellular organelles, inclusions, cavities, lipid depositions, etc) in the *C. elegans* posterior body segment are the source of high intensity THG signals. **Figure 5.6(d)** shows the superposition of the three nonlinear signals. It is again clear that the three types of nonlinear imaging (TPEF, SHG and THG) provide complementary information.

We point out that, by collecting THG images, detailed information related to the structure, the contour and the discontinuities of the animal tail are obtained (shown in **figures 5.5** and **5.6**). This information provides a frame of reference, which facilitates the precise localization of specific stained markers by fluorescence measurements and allowing structural orientation studies through SHG experiments.

Figure 5.7 shows the combined image of SHG (blue) and THG (red) of an embryo in a late developmental stage, just before hatching. The dimensions of the scanning region were $60 \times 40 \mu\text{m}^2$. The eggshell is clearly recognized by SHG signal, although signal from THG harmonic it is also observed. The eggshell consists of an external vitelline layer, a tough central layer made principally of chitin, and an internal lipid layer. THG shows the body of the larva, rolled over it. Strong signal of SHG arise from specific location of the nematode.

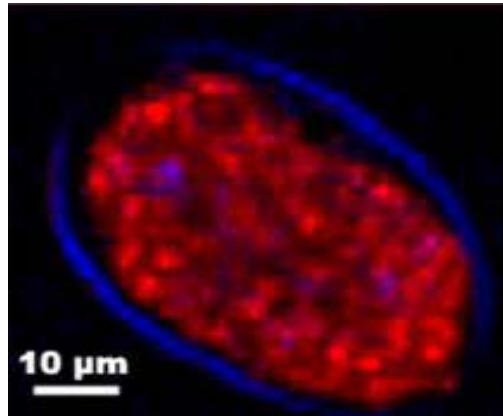


Figure 5.7: (a) Multimodal image of an embryo before hatching obtained by the combination of SHG (blue) and THG (red).

The resolution of our non linear system is limited to $1 \mu\text{m}$ due to the use of the xyz motorized stage (Standa). This choice represents an inexpensive and reliable solution for the realization of the scanning procedure. In order to verify, in a more accurate way, which anatomical features give rise to the THG signals and to improve the quality and resolution of the collected images, we performed a number of experiments by replacing the motorized stage with a galvano-mirror scanning system (6220H Cambridge Technology Inc.). In the following chapter, improved quality and higher resolution non linear images of the nematode are presented.

Of special interest is the capacity for three-dimensional (3D) reconstruction of a live organism that should facilitate the detailed description of anatomical features of both wild type and genetically modified animals. Such reconstructions may contribute to the understanding of the molecular mechanisms pertinent to specific genetic alterations. Since THG mainly provides information about boundaries between different media, it is feasible to reconstruct the animal outer surface and extract structural information from several inner organs by performing scan at different z positions. To this end, we utilized the Matlab software package (MathWorks.Inc) to design appropriate routines.

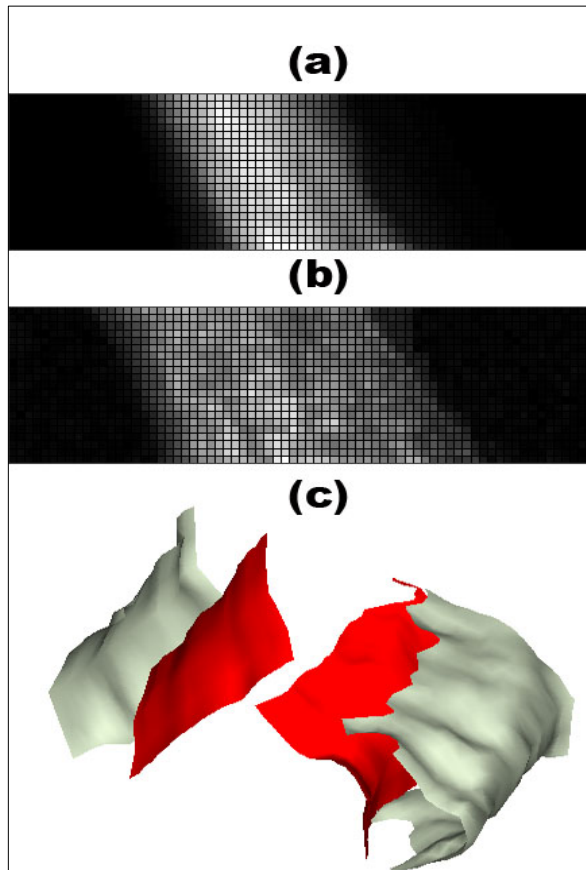


Figure 5.8: Z-projection of non-linear signals generated in the pharynx region of a worm expressing GFP in pharyngeal muscles. The projection comprises 5 slices 5 μm apart: (a) TPEF (b) THG. The 3D reconstruction is shown in (c).

Figure 5.8 shows the 3-D reconstruction of non linear (THG and TPEF) images obtained from the anterior part of *C. elegans*. The strain used in this line of experiments expressed GFP in the cytoplasm of the pharyngeal muscle cells. The dimensions of the scanning region were $71 \times 21 \mu\text{m}^2$. Five optical sections, $5 \mu\text{m}$ apart, were collected. **Figures 5.8(a)** and **5.8(b)** present the z-projection of the TPEF and THG images, respectively. The two different non linear images (TPEF and THG) were recorded simultaneously in each optical section. **Figure 5.8(c)** is the superposition of the two 3-D reconstructed images. Because GFP molecules are localized inside the pharynx of the nematode, the outline of the pharynx can be recognized (red surface) from the reconstruction of the TPEF images. Conversely, the contour of the worm body is becomes obvious (gray surface) by the reconstruction of THG images. It is important to point out, the difference in the origin of TPEF and THG signals. Whereas THG provides information about the morphological features of the worm and internal organs, TPEF indicates the position of the fluorescent protein.

The 3-D reconstruction of THG and TPEF images, recorded from the posterior part of the nematode is shown in **figure 5.9**. We used strains that express GFP in the cytoplasm of the six mechanoreceptor neurons of *C. elegans*. The dimensions of the scanned region were $41 \times 21 \mu\text{m}^2$. Eight optical sections, $5 \mu\text{m}$ apart, were obtained.

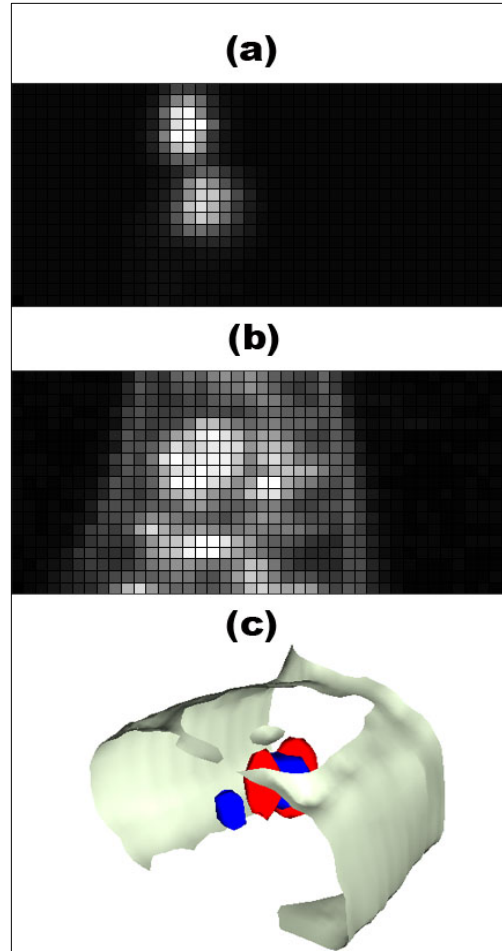


Figure 5.9: Z-projection of the non-linear signals generated in the tail of a worm expressing GFP in the mechanoreceptor neurons. The projection corresponds to 8 slices every 5 μm : (a) TPEF (b) THG. The 3D reconstruction is shown in (c).

Figure 5.9(a) shows the z-projection of TPEF images, **figure 5.9(b)** depicts the corresponding THG images and **figure 5.9(c)** is the superposition of the two (TPEF and THG) 3-D reconstructed images. The precise 3-D localization of the two touch receptor neurons which are positioned near the tail of the animal is easily derived (red surface) from the reconstruction of TPEF images (due to fluorescence of the cytoplasmic GFP molecules). Moreover, detailed morphological information concerning the shape (gray surface) and the inner structure of the animal tail (blue surface) can be obtained from the reconstruction of THG images.

6.1 Experimental apparatus

The resolution of our previous non linear system is limited to $1\ \mu\text{m}$ due to the use of the xyz motorized stage (Standa). This choice represents an inexpensive and reliable solution for the realization of the scanning procedure. In order to verify, in a more accurate way, which anatomical features give rise to the THG signals and to improve the quality and resolution of the collected images, we performed a number of experiments by replacing the motorized stage with a galvano-mirror scanning system (6220H Cambridge Technology Inc.).

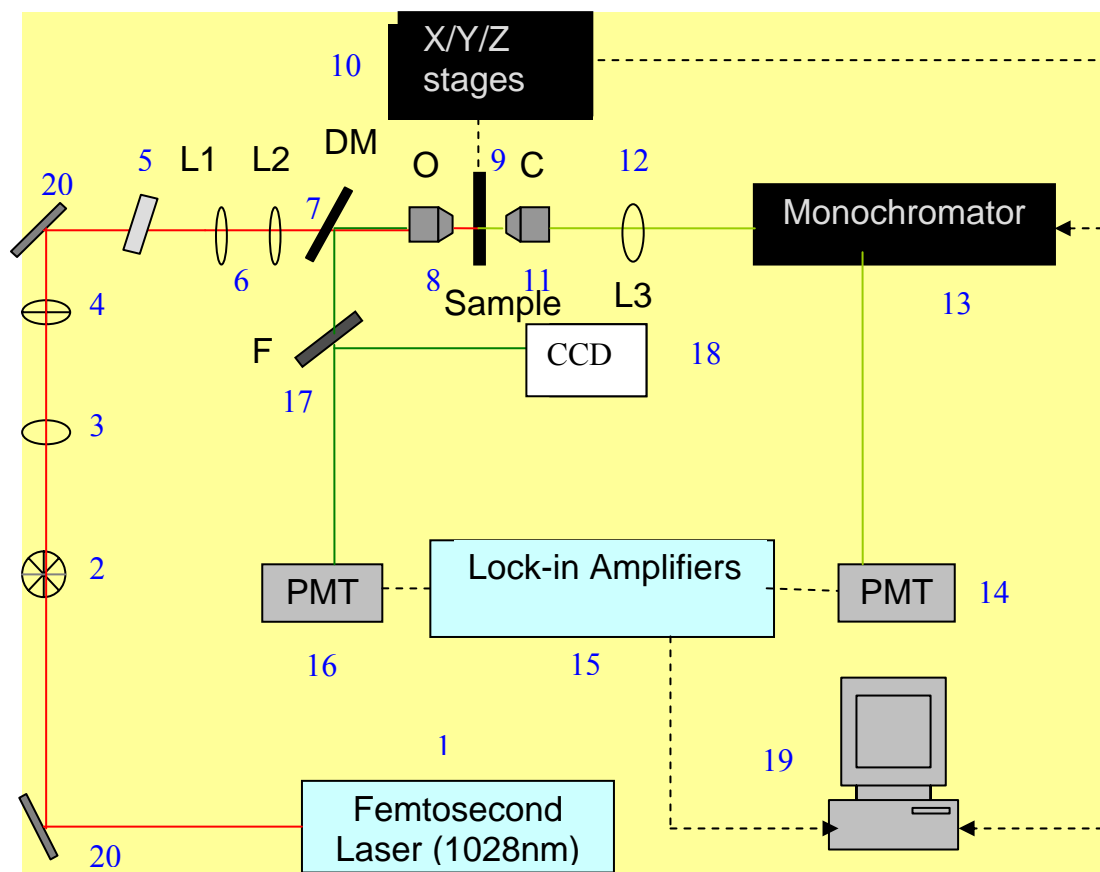


Figure 6.1: Experimental set-up for combined TPEF and SHG or THG microscopy. 1) Femtosecond laser ($\lambda=1028\text{nm}$), 2) chopper, 3) Iris, 4) attenuator, 5) Scanning System, 6) lenses, 7) Dichroic mirror, 8) Objective lens, 9) Holder of the sample, 10) x-y-z motorized stages, 11) Condenser lens, 12) Lens, 13) Monochromator, 14) Photo-multiplier tube(PMT), 15) Lock-in amplifiers, 16) PMT, 17) Flip-mount mirror, 18) CCD camera, 19) P.C., 20) Reflecting mirrors.

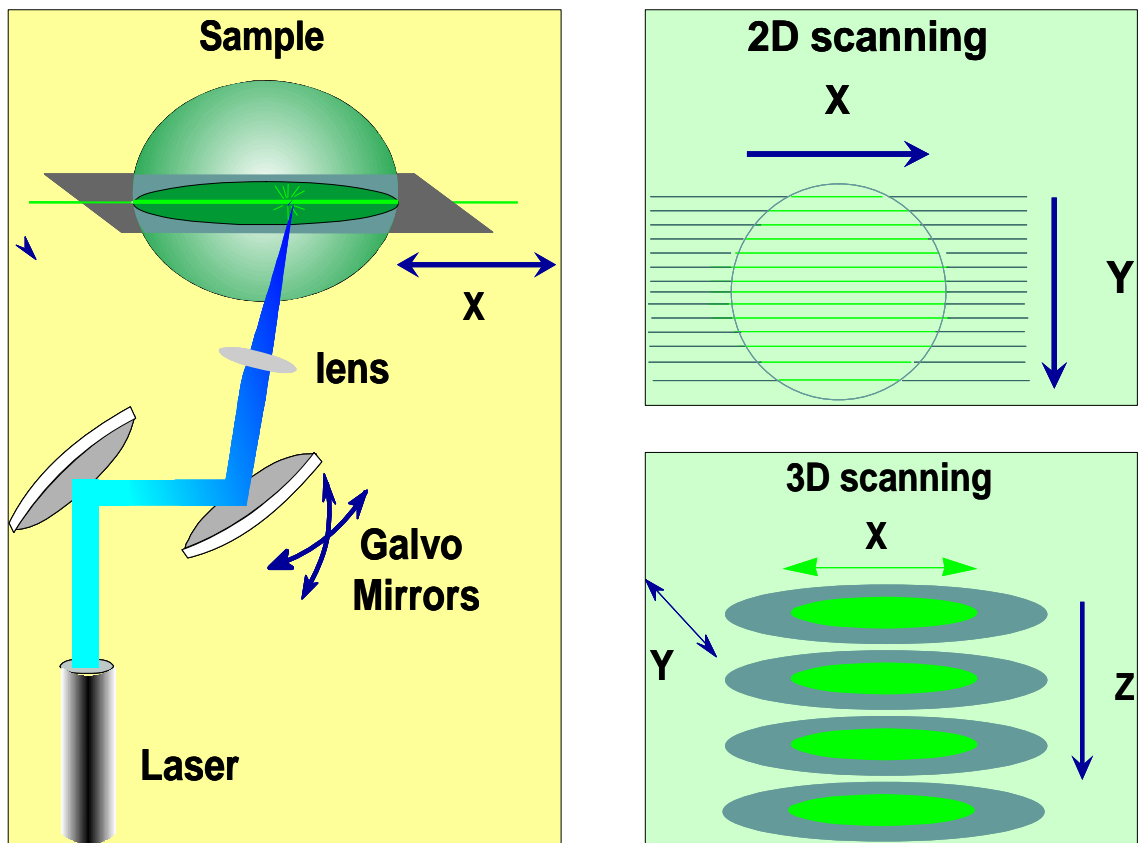


Figure 6.2: Description of the Galvo-mirrors function. The galvo-mirrors scan in 2 dimensions (x,y), while the standa stages move the sample in z direction. [51]

Instead of moving the sample, this configuration moves the galvo-mirrors, which are computer-controlled by specially designed software (National Instruments, Labview7.1). Consequently, the laser beam scans the area that is defined by Labview software. The resolution of the image depends on the number of points that are chosen for the scanning. High resolution needs a large number of points. The scanned area can be a square or rectangle depending on the dimensions of the scanned area that are defined by Labview software.

For 3-D reconstruction, the sample is moved by the z motorized stage (Standa), which is controlled by Labview software .

6.2 Experimental results

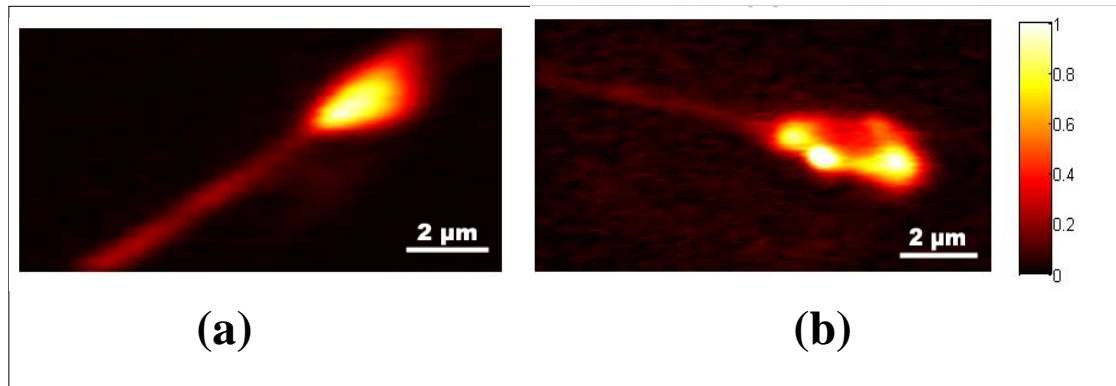
Posterior part

Figure 6.3 : TPEF images from mechanosensory neurons of C.Elegans marked with (a) diffused GFP (b) oriented GFP.

In this line of experiments transgenic animals that express GFP under the *mec-4* touch –cell specific promoter in two out of the six mechanoreceptor neurons are imaged. The PLM(L/R) touch receptor neurons are located in the posterior part of the worm, close to the tip of the tail, away from the gut autofluorescence. In **figure 6.3**, TPEF signals arising from these neurons are shown. Scanning was performed at a specific z position, where the TPEF signal emanating from the neuron was maximal. The dimensions of the scanned region were $12 \times 6 \mu\text{m}^2$ with a resolution of 60nm/pixel. Two different kinds of GFP markers have been used: diffused GFP (**figure 6.3(a)**) and oriented GFP (**figure 6.3(b)**). The first one is localized in the cytoplasm of the mechanoreceptor neurons of the animal, when the second is attached to the membrane of the neuron. The absorption and emission maxima for GFP are 489 and 508, respectively. Although the excitation wavelength of our laser for TPEF measurements is not optimal for the excitation of the GFP molecules (less than 20% is the absorption efficiency of the GFP at

514nm) it was observed that not only the neuronal cell bodies (2-3 microns) but and others anatomical components such as neuronal axons (~200nm) are detectable.

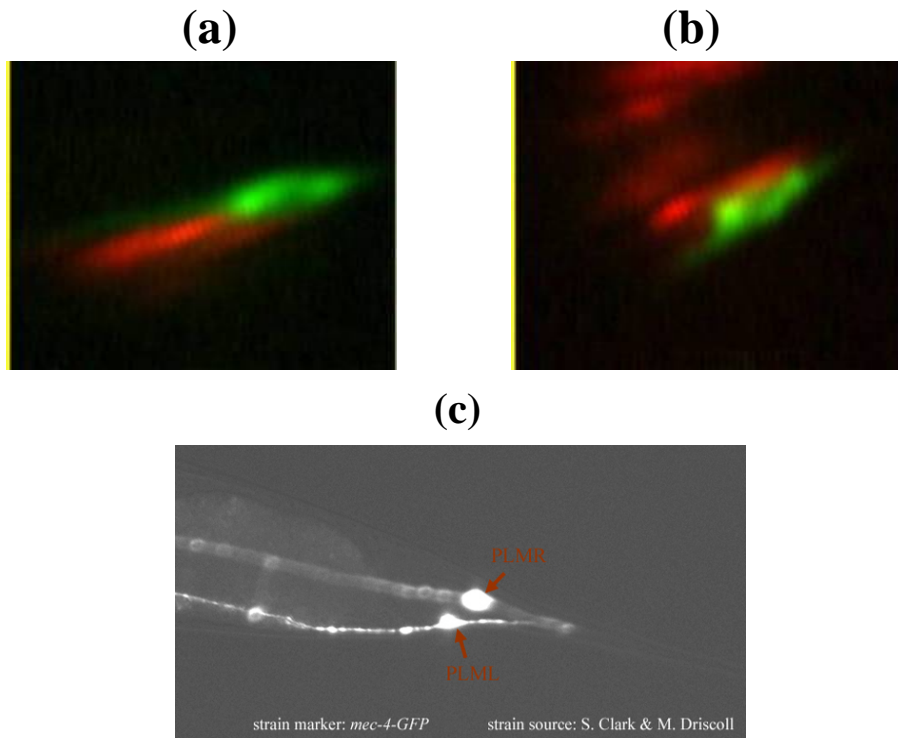


Figure 6.4: The recorded signals of combined TPEF and SHG measurements, arising from the two touch receptor neurons in the posterior part of *C.Elegans*. TPEF(green) is arising from the GFP molecules expressed in the cytoplasm of the mechanoreceptor neurons and SHG(red) coming from the muscles of the nematode. (a) Combined imaging of the PLMR, (b) Combined imaging of the PLML. (c) The two touch receptor neurons, localized in the posterior part of *C. elegans* are shown. Fluorescence arises from GFP molecules, attached to the transmembrane protein MEC-4.

The pictures above depicts the two touch receptor neurons in the posterior part of the worm through TPEF measurements. Endogenous structural proteins (actomyosin complexes) are the main contributors to the recorded SHG signals. [46,48] The scanning area is $12 \times 12 \mu\text{m}^2$ and $8 \times 8 \mu\text{m}^2$ and 100 points resolution respectively(1pixel ~ 150nm).

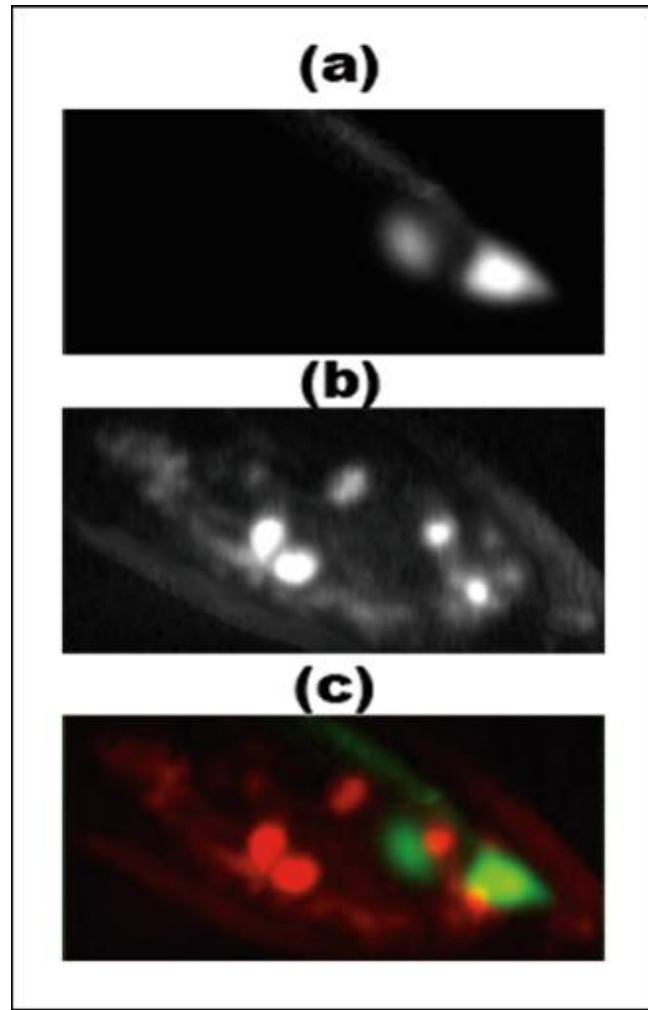


Figure 6.5: Non-linear signals generated at the tail of an animal expressing GFP in the mechanoreceptor neurons: (a) TPEF (b) THG (c) multimodal image obtained by the combination of the previous two: TPEF (green), THG (red).

Figure 6.5 shows the non-linear images (**6.5(a)** TPEF, **6.5(b)** THG and **6.5(c)** the combination of the two previous contributions; TPEF in green, THG in red), obtained from the tail of an animal expressing GFP in the mechanoreceptor neurons. The scanning area is $30 \times 15 \mu\text{m}^2$ with 200 and 100 points resolution respectively (1 pixel ~ 150 nm). The precise localization of the two touch receptor neurons and one neuron axon is feasible via TPEF measurements. Consequently, by employing this configuration new anatomical features such as the axon morphology of worm neurons (~ 200 nm) are easierly detectable. We note that,

for the THG measurements (**Figure 6.5(b)**) the main signal contributors (discontinuities in the tail of the animal) are similar with the ones detected by employing the xyz Standa system (**Figures 5.6(b)** and **5.9(c)**).

Since THG mainly provides information about boundaries between different media, it is feasible to reconstruct the animal outer surface and extract structural information from several inner organs by performing scan at different z positions. The 3D reconstructions of THG, SHG and TPEF images, recorded from the posterior part of the nematode are shown in **figure 6.6**.

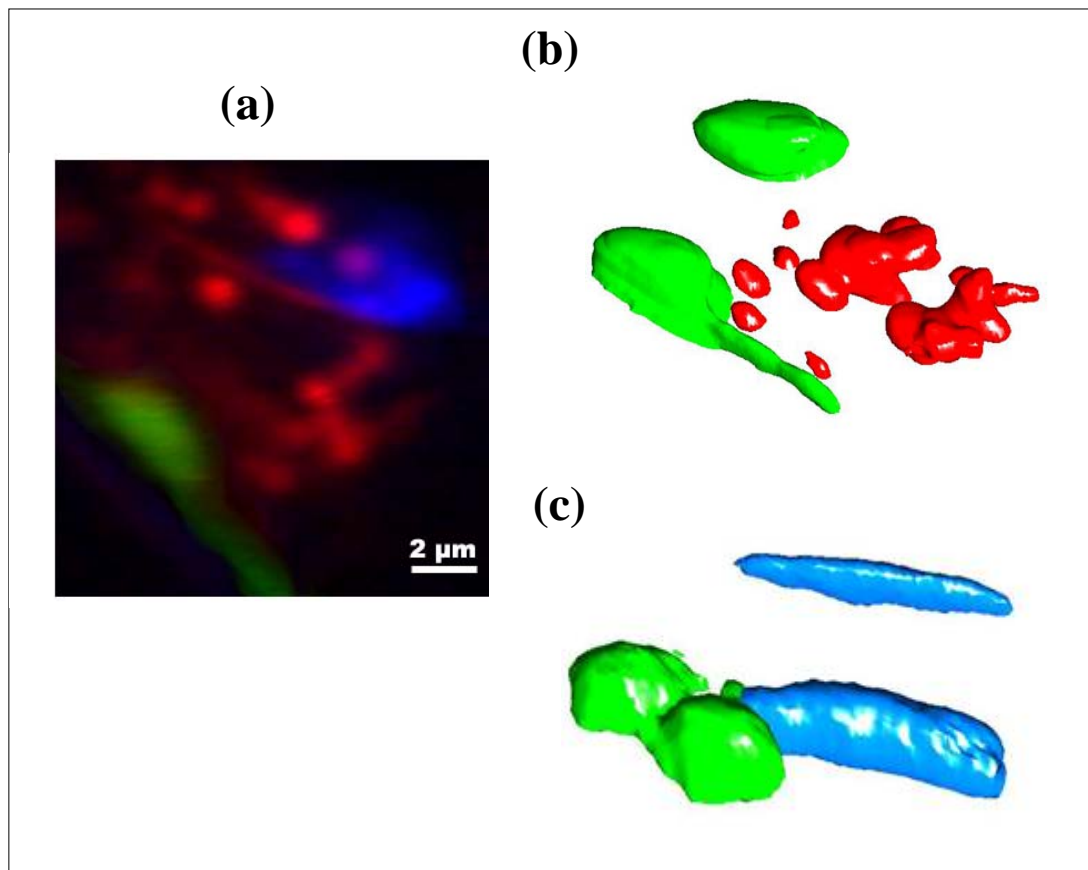


Figure 6.6: Non-linear signals (TPEF (green), THG (red) and SHG (blue) generated at the tail of an animal expressing GFP in the mechanoreceptor neurons: (a) Multimodal images from the posterior part, (b) 3D reconstruction of TPEF and THG with diffuse GFP, (c) 3D reconstruction of TPEF and SHG with oriented GFP.

Figure 6.6(a) depicts non-linear imaging (TPEF-SHG-THG) of the posterior part of a sample. TPEF image was obtained in backward detection, while SHG and THG measurements were detected in the forward direction.

The recorded TPEF signal arises from cytoplasmic GFP molecules, which are expressed in these two touch receptor neurons. It is clear that the precise localization of a touch receptor neuron and its axon (green). The SHG image enabled us to detect somatic muscles close to the tail of the worm. Endogenous structural proteins (actomyosin complexes) are the main contributors to the recorded SHG signals [46, 48]. GFP molecules in the neuronal cell are symmetrically distributed. Therefore, their contribution to the observed SHG signal is expected to be minimal. The morphology and the contour of the worm can be observed through THG and SHG measurements, the last one due to its composition of collagen. Rather, discontinuities (such as sub-cellular organelles, inclusions, cavities, lipid depositions, etc) in the *C. elegans posterior* body segment are the source of high intensity THG signals.

Figure 6.6(b) presents strains that express GFP in the cytoplasm of the six mechanoreceptor neurons of *C. elegans*. Twelve optical sections, 1 μ m apart, were obtained. The precise 3-D localization of the two touch receptor neurons and one neuron axon which are positioned near the tail of the animal is easily derived (green surface) from the reconstruction of TPEF images (due to fluorescence of the cytoplasmic GFP molecules). High THG signals were generated by discontinuities in the region of the tail (red surface). These discontinuities are likely due to lipid depositions [45] or formations of discontinuous refractive index in the tail.

Figure 6.6(c) shows the superposition of the 3D reconstruction of TPEF (green) of an neuron with oriented GFP and SHG (blue) arising from somatic muscles. The image is form from 15 slices obtained every 1 μm . The neuronal axon of these neurons travels all along the mid body of the worm.

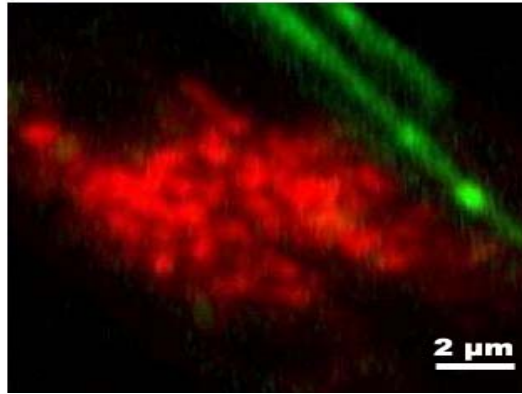


Figure 6.7: the mid-body section showing the neuronal axon and the intestines.

In **figure 6.7** can be clearly distinguish the axon in the area of the intestine presenting some clusters of GFP molecules (green). Intestinal cells are filled with numerous granules that likely contain lipids, proteins and carbohydrates. Due to this concentration of lipids, a big signal of THG signal is detected from intestine (red). The dimensions of the images are $13 \times 13 \mu\text{m}^2$, with a 65 nm/pixel resolution.

Anterior part

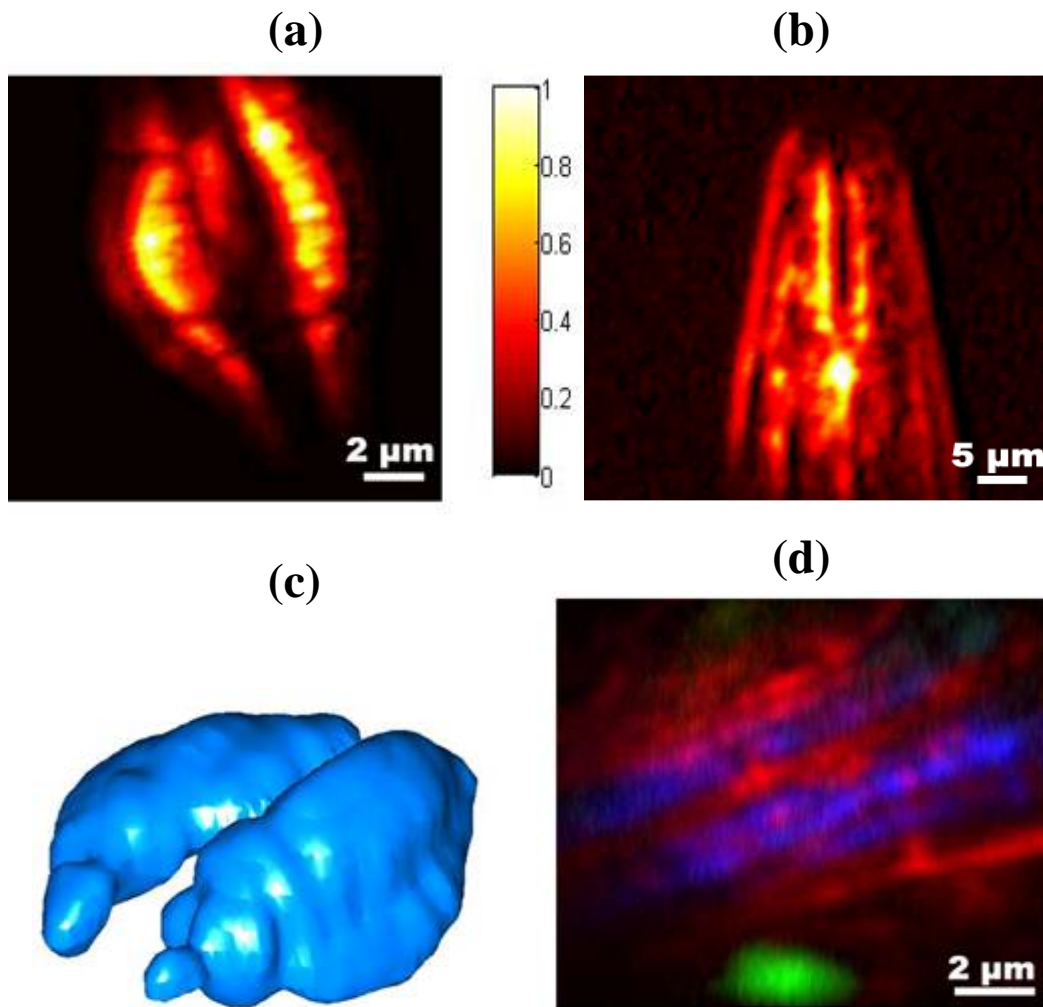


Figure 6.8: Higher harmonic signals from wild type *C. elegans*: (a) SHG from the anterior bulb of the pharynx (b) THG signal from the buccal cavity. (c) 3D reconstruction of the SHG signal from the anterior bulb of the pharynx. (d) Multimodal image obtained by the combination of TPEF (green), THG (red) and SHG (blue) from *C. elegans* expressing DsRed in CEP neurons.

Figure 6.8(a) shows the SHG signal recorded from the pm4 muscle of the anterior bulb of the pharynx of a wild type *C. elegans*. The image is 200×200 points with a resolution of 80 nm/pixel, approximately. In **figure 6.8(b)** the buccal cavity of a larva through THG is illustrated. The image dimensions are $50 \times 50 \mu\text{m}^2$. The structure of the pharyngeal epithelium can clearly distinguish. In **figure 6.8(c)** the obtained 3-D reconstruction of SHG images is shown. No

fluorescent markers have been used, reducing the photodamage. Twelve optical sections, 1 μm apart, were collected.

In **figure 6.8(d)** we show a high resolution picture ($12 \times 12 \mu\text{m}^2$ with 60 nm/pixel) of the isthmus region between the two pharyngeal bulbs. In this case transgenic animals were genetically modified to express DsRed strain marker in the ADE, CEPD and CEPV neurons in the head, PDE in the mid body and PVQ in the tail. In the anterior part of the worm the nervous system includes twenty neurons that innervate and regulate the activity of the pharynx. The three classes of dopaminergic neurons (CEPs, ADEs, and PDEs) function redundantly to sense the mechanosensory stimulus from bacteria and mediate the motor circuit to control the behavioural known as basal slowing response. In **figure 6.8(d)** it is visible the CEPDL neuron (CEP neurons are directly exposed to the pseudocoelomic body fluid), through TPEF measurement (green). DsRed has significant advantages in this setting, such as bright red fluorescence and resistance against photobleaching. The absorption and emission maxima are 557 and 579, respectively. The excitation wavelength of our laser for TPEF measurements is optimal for the excitation of the DsRed molecules since the DsRed absorption efficiency is more than 50% at 514 nm, and its emission (fluorescence) is far away from the detection wavelength of SHG signals. SHG signal (blue), like in **figure 6.8(c)**, arise from longitudinal somatic muscles, whereas THG signal show the boundaries of the pharyngeal muscles due to abrupt changes of the refractive index values. This indicates constitution differences between different tissues. This information provides a frame of reference, which facilitates the precise localization of specific stained markers by

fluorescence measurements and allowing structural orientation studies through SHG experiments.

The main target of this study is the development and optimization of a user friendly and compact microscope system that combines different nonlinear image-contrast modes (TPEF-SHG-THG) in a single instrument and employed femtosecond laser pulses as excitation source.

7.1 THG imaging microscopy measurements as a tool for the *in vivo* monitoring of neuron degeneration in *C. elegans* samples.

Caenorhabditis elegans is widely used as a model system to study ageing and longevity-related processes. A number of genes have been demonstrated to play major roles in determining the lifespan of this nematode.

The ageing process precipitates dramatic alterations in the physiology of all organisms, including reduced cellular function, compromised resistance to stress and pathological agents, and increased likelihood of developing age-related diseases. Among the most characteristic pathologies associated with old age are numerous late-onset neurodegenerative disorders such as Alzheimer's, Parkinson's and Huntington's diseases. In addition to stroke, which also inflicts loss of neuronal cells, these conditions account for ever-increasing debilitation among the elderly. Recent studies in model organisms such as the nematode *Caenorhabditis elegans* and the fruit fly *Drosophila melanogaster*, which offer the prowess of sophisticated genetic approaches, have uncovered significant, novel aspects of the molecular mechanisms that underlie both neurodegeneration and the ageing process. These advances hold promise that the intimate link between the aged state and the manifestation of several neurodegenerative diseases will be deciphered. [54]

At a first attempt to develop a mutant strain by targeting endogenous APP (Amyloid Precursor Protein) gene [54], researchers found that the *C. elegans* genome does include genes that encode proteins related to human APP- *apl-1*.

Alzheimer's disease (AD) has been associated with aggregation of β -amyloid peptide (A^β) and cell death in the brain. Using various models, such as the

nematode *Caenorhabditis elegans*, the fruit fly *Drosophila melanogaster* and the mouse *Mus musculus*, investigators have attempted to imitate the pathology process of AD for better understanding of the cellular mechanisms and for possible therapeutic intervention. Among many *in vitro* and *in vivo* models of AD, transgenic *C. elegans* expressing human A^β has shown its own advantages.

The transgenic *C. elegans* model have been used in studying AD due to its short life span, facility to maintain, ability to develop muscle associated deposits reactive to amyloid-specific dyes and the concomitant progressive paralysis phenotype. Moreover, the transgenic *C. elegans* exhibits increased levels of reactive oxygen species (ROS) and protein carbonyls, similar to those observed in AD patients, supporting the current theory on A^β-induced oxidative stress and subsequent neurodegeneration in AD. DNA microarray assays of the worm demonstrated several stress-related genes being upregulated, particularly two genes homologous to human α^B-crystallin and tumor necrosis factor-related protein, which were also upregulated in postmortem AD brain. [56]

IMBB researchers demonstrate [57] that the cellular process of protein synthesis is intimately coupled with the pace of ageing. Protein synthesis is one of the most energy-demanding cellular processes, consuming almost 50% of the total energy produced by the cell.

Ageing and senescence are complex processes that dramatically impact human health. Elucidation of the basic molecular mechanisms underlying the progressive decline in cellular function that accompanies ageing and eventually leads to senescence will have an immediate impact on the design of novel interventions that could reduce or delay age-related deterioration in humans.

In addition, Parkinson's disease (PD) is another of the most common age-related neurodegenerative diseases that is characterized by selective loss of dopaminergic neurons. *C. elegans* represents a powerful system for the identification of factors involved in neurodegeneration. [58]

THG imaging is a non-invasive technique that can be useful in the determination and the extraction of unique information related to the in vivo cellular processes. Differences in THG coefficients at different locations in the biological sample translate to differences in THG intensities that can be measured. This principle can therefore be used to form a compact user friendly nonlinear laser-scanning microscope very helpful for the biologists, permitting the precise localization of the degenerated neurons of various biological specimens. The nonlinear dependence of THG on the excitation power provides inherent optical sectioning. At the same time, the non-resonant nature of THG, in combination with the near-IR excitation wavelengths used (1028nm), render this technique potentially (biologically) nondamaging and nonbleaching. Consequently, THG can be fairly regarded as the most suitable technique for the imaging of structural features and molecular processes of transparent samples like *C. elegans* samples.

Mutations in a number of genes, including but not limited to *mec-4*, *deg-1*, and *deg-3*, lead to the death of particular cells by causing them to swell and lyse. Analysis of these mutations has shown that in most cases, the degeneration-inducing mutation results in a gain of gene function, that the mutated gene encodes an ion channel subunit, and that the affected cells are neuronal.

Swelling deaths induced by gain-of-function mutations in genes of the degenerin family, such as *mec-4*, *deg-1*, and *mec-10*, exhibit morphological features of necrotic cell death. Such deaths are distinct from programmed cell death in

several ways: Cells undergoing programmed cell death, appear to be compacted and “button-like”, whereas cells undergoing degenerative cell death appear to be swollen and enlarged (**figure 7.1**). In addition, distinct ultrastructural changes accompany the two types of death, programmed cell deaths transpire within the hour, whereas degenerative deaths occur over several hours.

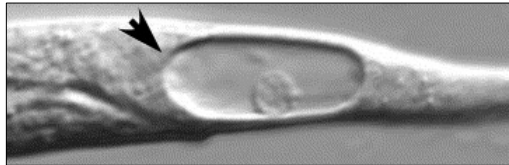


Figure 7.1: Neurodegeneration in worms.

The time of onset of degenerative death correlates with initiation of degeneration gene expression, and the rapidity with which death occurs correlates with dose of the toxic allele. These observations are consistent with the hypothesis that a threshold ion influx is needed to initiate the degenerative process. Ultrastructural analysis has established that degeneration initiates with striking infoldings of the plasma membrane. Small tightly wrapped membranous whorls are the first indications of pathology. Subsequently, internalized whorls grow in size and large vacuoles appear. Cell body volume can increase 100-fold during this process. The nucleus becomes distorted and chromatin aggregates. Internal degradation of cell contents then follows shortly. [59] In the framework of this study larvae worms were irradiated. The samples used, were especially prepared in the laboratories of IMBB, with degenerated neurons. For the realization of the THG measurements the following experimental set up (**Fig 7.2**) was developed.

7.2 Experimental apparatus

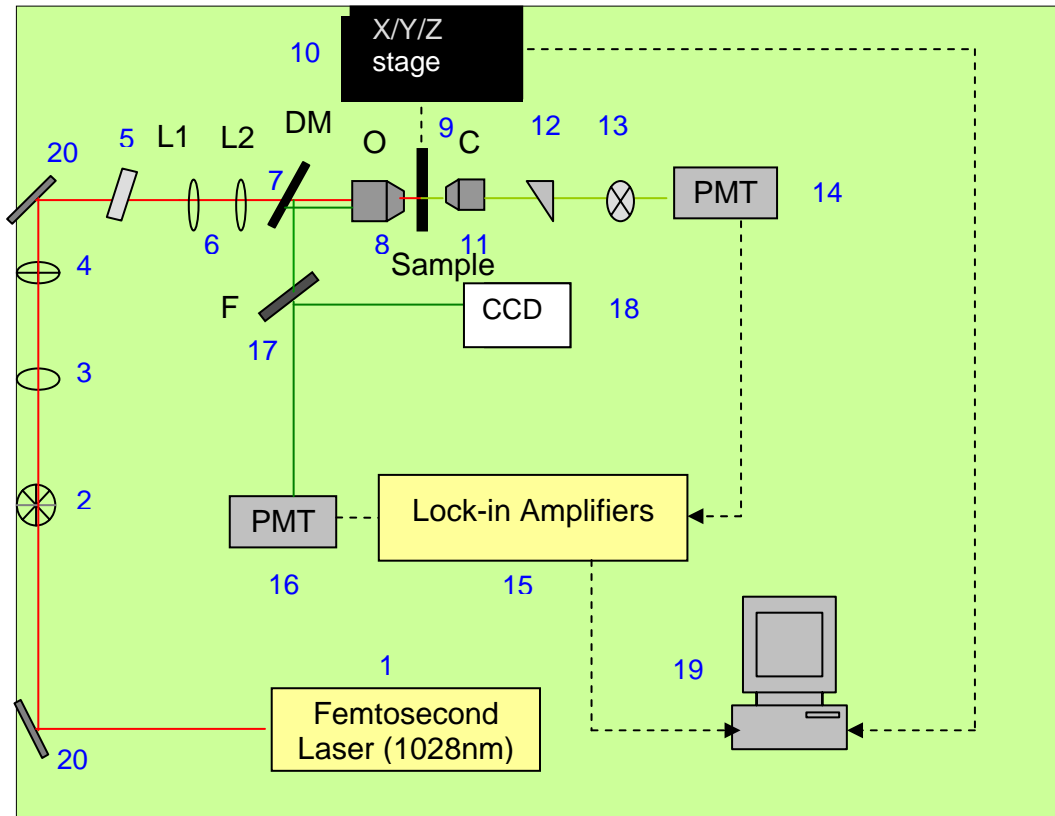


Figure 7.2: Experimental set-up for THG microscopy measurements. 1) Femtosecond laser ($\lambda=1028\text{nm}$), 2) chopper, 3) Iris, 4) attenuator, 5) Scanning System, 6) lenses, 7) Dichroic mirror, 8) Objective lens, 9) Holder of the biological sample, 10) x-y-z motorized stages, 11) Condenser lens, 12) Reflecting IR mirror at 45° , 13) 340nm band pass filter (UQG Hoya U 340 UV transmitting Vis and IR absorbing 14) Photo-multiplier tube, 15) Lock-in amplifiers, 16) PMT, 17) Flip-mount mirror, 18) CCD camera, 19) P.C, 20) Reflecting mirrors.

7.3 Experimental results

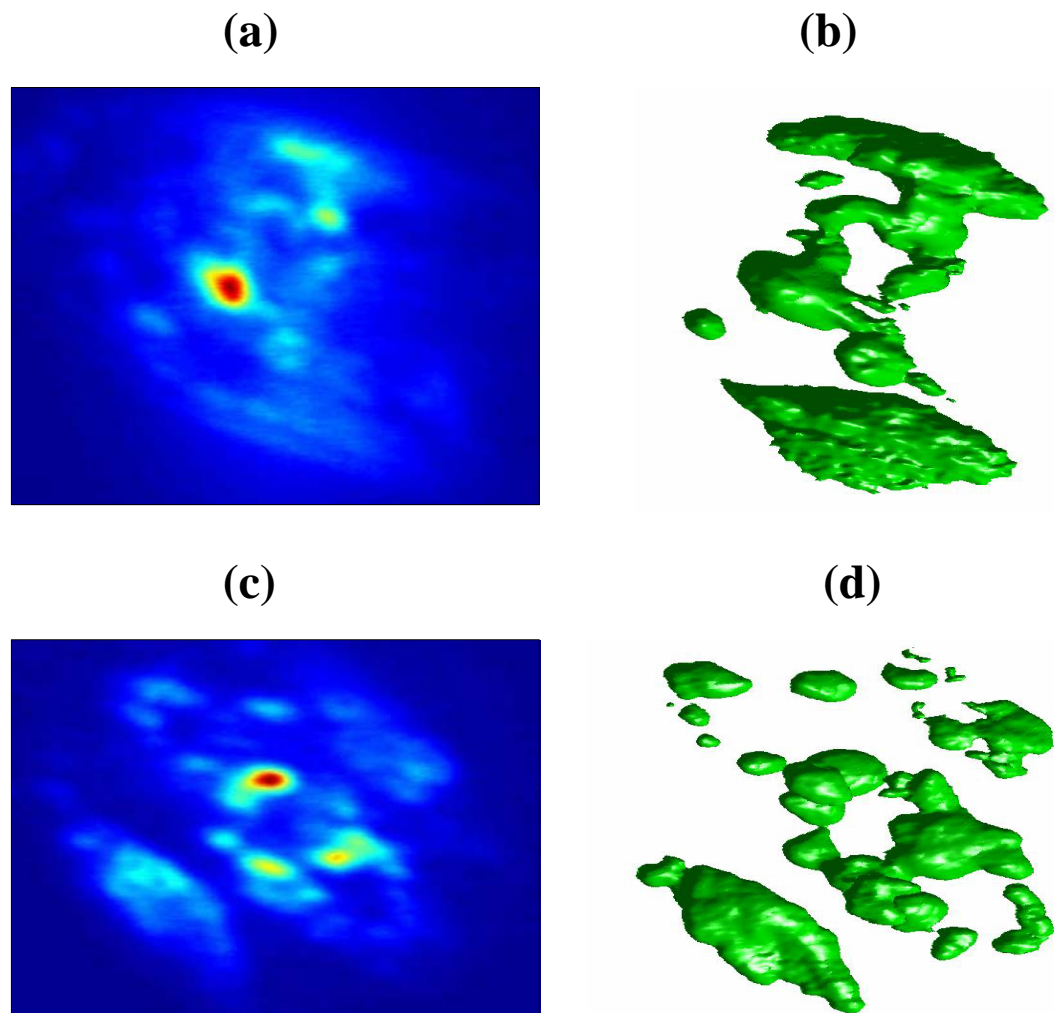


Figure 7.3: THG imaging of a degenerated neuron: (a) Normalized image of 10 stacks, (b) 3D reconstruction of 10 stacks separated by $1\mu\text{m}$, (c) THG Image of 13 stacks, (d) 3D reconstruction of 13 stacks separated by $1\mu\text{m}$.

By employing the developed set-up the precise morphology and the contour of the degenerative neurons in the posterior part of the nematode can be observed in vivo through THG measurements. Furthermore, high intensity THG signals are

detected from the discontinuities such as sub-cellular organelles, inclusion, cavities or lipid depositions in the *C. elegans* posterior body segment.

In the **figure 7.3(a)** the strongest signal of THG arises from the lipids surrounding the degenerative neuron. Moreover, THG signal coming from the contour of the worm. The scanning area is $15 \times 15 \mu\text{m}^2$ and 300 points resolution.

In **figure 7.3(b)**, the 3-D reconstruction depicts in a more accurate way the shape of the hole and the morphology of the contour of the worm. It consists of 10 stacks separated by $1 \mu\text{m}$.

Figure 7.3(c) illustrates again the degenerated neuron of the nematode. This THG image consists of 13 stacks. The shape of the hole in the neuron is better depicted in this image than in **figure 7.3(a)**.

The 3-D reconstruction of this image consists of 13 stacks separated by $1 \mu\text{m}$ and depicts the precise shape of the degenerated neuron and the lipid inclusions that surround it (**Figure 7.3(d)**).

The following **figure (7.4)** presents an ameliorated resolution in comparison with the previous one. The scanned area is $15 \times 15 \mu\text{m}^2$ and the resolution of this image is 300 points.

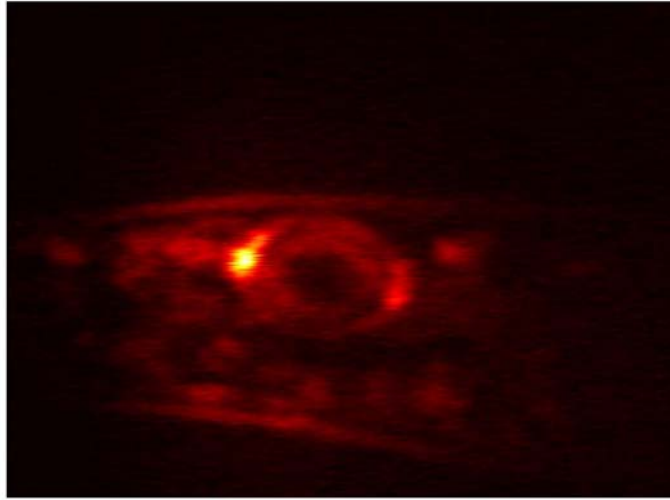


Figure 7.4: THG image of the posterior part of the larvae. Scanned area $15 \times 15 \mu\text{m}^2$.

In the picture above (**Figure 7.4**), the shape of the hole can be clearly observed. The lipids on the membrane of the neuron are the source of the strongest THG signal. In addition, THG signal arising from the contour of the posterior part of the worm is clearly recorded.

The picture below (**Figure 7.5**) illustrates the movement of the nucleus in the cavity of the degenerative neuron of the nematode. THG permits the detection not only of structural features but also of processes happening in organelles such as neurons. Molecular processes can be observed and provide important information on the internal degradation of the cell. The scanning area is $15 \times 15 \mu\text{m}^2$ and the resolution 300 points.

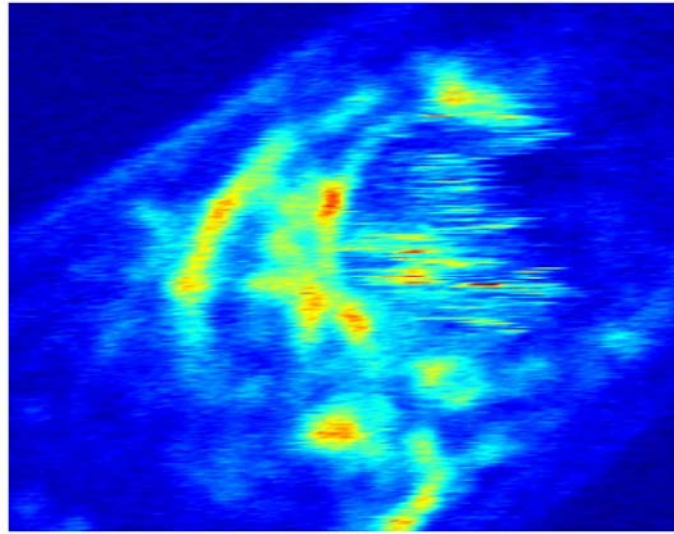


Figure 7.5: Detecting the movement of the nucleus in the cavity of the degenerated neuron by recording THG signal.

After the *in vivo* precise identification of the shape and the contour of the degenerative neurons in the posterior part of the nematode, the monitoring, in real time, of the evolution of the degenerative neurons of the worm through THG imaging measurements (**Figure 7.6**) comprises the second target of this study.

In **figure 7.6(a)** the 2-D normalized image consists of 14 stacks. The small nucleus can be observed in the hole, but in this measurement its movement could not be detected. Additionally, a part of the contour of the hole is detectable. After 20minutes, the vacuole has shrunk, consequently by performing THG measurements, the alterations on the membrane of the vacuole can be observed (**figure 7.6(b)**). It is worth mentioning that the measurements were performed at the same scanning area with the same resolution as in the **figure 7.6(a)**.

The change of the shape of the neuron is more obvious in the 3D reconstruction by Matlab simulation (red insets in **figures 7.6(a)** and **7.6(b)**). In addition, the

presence of organelles or lipids round the cavity can be observed. Lipids are the source of the highest signal of THG.

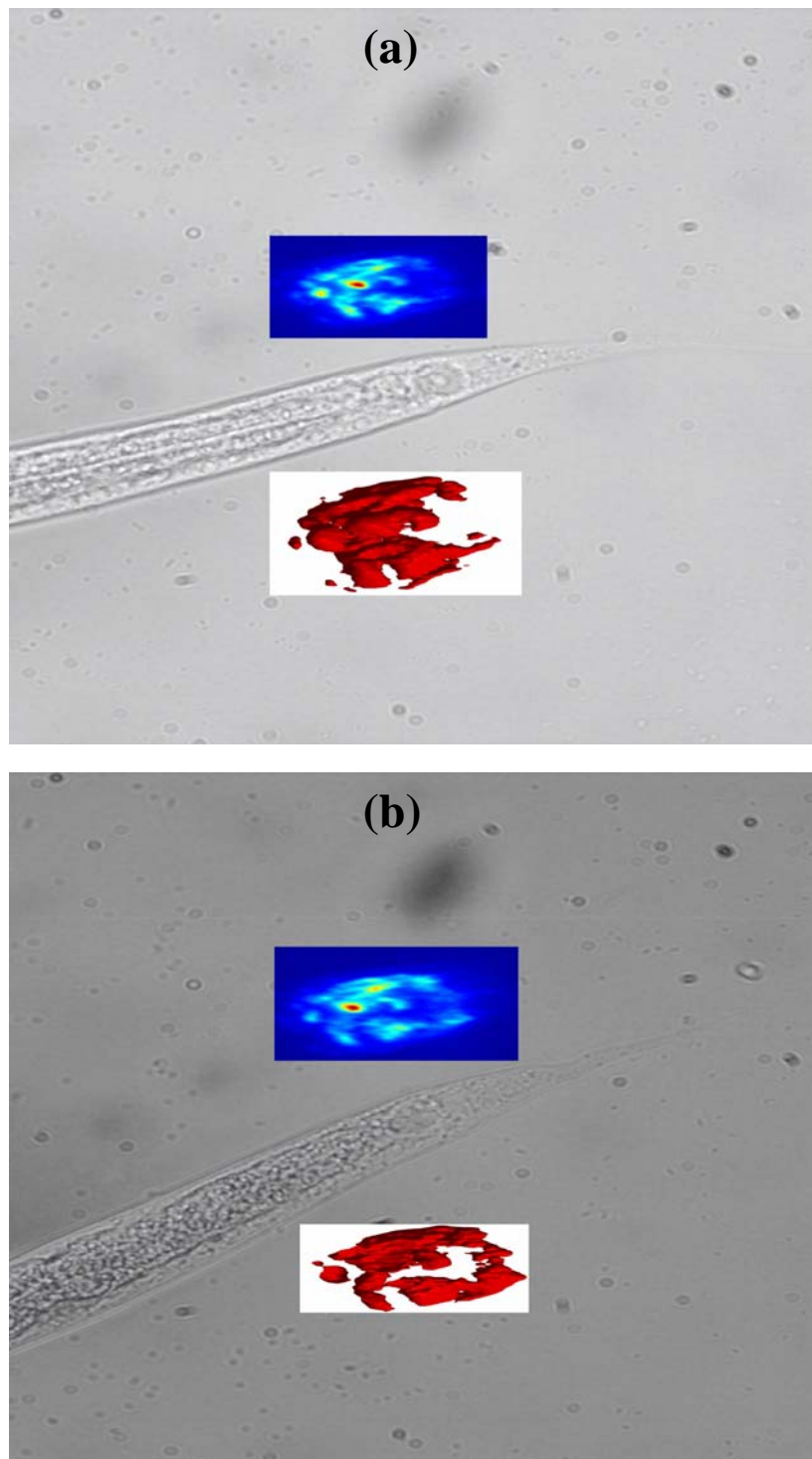


Figure 7.6: (a) THG imaging and 3D reconstruction of 14 stacks separated by $1\mu\text{m}$ compared with the image obtained from the CCD camera, (b) evolution of the hole after 20 minutes. The dimensions of the scanned area are $15\times 15\mu\text{m}^2$ and the resolution 1pixel $\sim 150\text{nm}$.

Images of the evolution of the degenerative neurons of the posterior part of the worm were obtained after the performance of experiments on 30 different samples. The picture that follows depicts the evolution of the vacuole of the worm. The data were obtained every hour, in order to make clear the changes happening in the hole; Changes of its shape or inside. According to the picture taken by the CCD camera, it is obvious that the shape of the degenerative neuron changes and gets smaller. That means that the vacuole shrinks as the time passes.

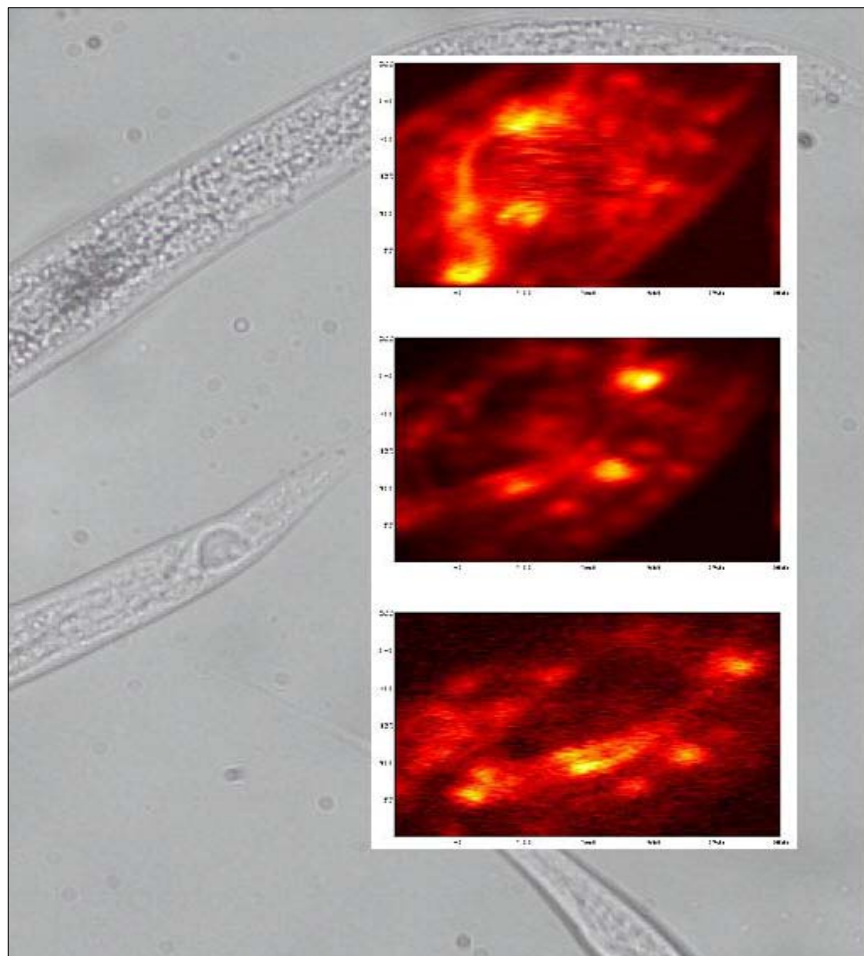


Figure 7.7: Images of the posterior part of *C. elegans* consisting of 8 slices $1\mu\text{m}$ apart: Three images were recorded every one hour.

The measurements for every collected image were performed at the same scanning area with the same resolution. The dimensions of the scanning area are $15 \times 15 \mu\text{m}^2$, while the resolution of the image is 300 points.

In **figure 7.7** the movement of the nucleus is obvious in the first image (zero time), while in the second (one hour later) the vacuole is narrower and the internal organelles, like nucleus's movement, is not detected. In the third picture (two hours later) the degradation of the cell is obvious. The shape of the vacuole is shrunk and no internal organelles are detected. This proves that degenerative deaths occur over several hours. Consequently, the changes of the shape of the hole are obvious from the recorded images. Two hours later, the neuron is narrower and no internal organelles are detectable in comparison with the fresh sample (zero time (**figure 7.7**)).

Concluding, highly spatially resolved and highly penetrative non-invasive *in vivo* non linear imaging microscopy has the potential of offering new insights into the morphological changes and the complex developmental processes. By using endogenous higher harmonic generation as the microscopic contrast mechanism, no fluorescence is required and the common issues of photodamage, phototoxicity, photobleaching, dye availability, or dye toxicity can all be eliminated. By properly choosing the excitation source that will allow detectable SHG and THG signals but minimize the unwanted interactions, cellular processes can be *in vivo* monitored continuously for a long period of time.

This technique can provide high-spatial resolution (in the order of 200nm), excellent sectioning of the biological sample and high-contrast *in vivo* images of developmental processes deep inside larvae without extra labelling or handling.

This demonstrated higher harmonic generation microscopy, a truly non-invasive microscopy, should be potentially useful for studying cell-fate determination at early developmental stages. Especially THG imaging microscopy is a powerful tool for the *in vivo* monitoring of cell death (neuron degeneration) in various biological samples. By employing this innovative non invasive imaging technique unique information related to the mechanisms and the processes of cell death will be extracted.

However, many tasks remain at hand, to fully develop this unique technique into a reliable and useful tool for imaging both biological and non-biological specimens. For instance, much more work needs to be done to fully quantify the mechanisms responsible for image contrast. Further, no attempt was made in this study to vary the laser parameters (such as the polarization of the excitation beam, wavelength of excitation, repetition rate, pulse duration etc) to truly optimize the efficiency of the THG signal. [60].

Clearly, the THG efficiency would benefit greatly from the use of shorter pulses. It is unclear however, how shorter pulses may affect the viability of a living system. Thus, a systematic study that varies pulse repetition rate, energy, and pulse duration in an attempt to optimize THG efficiency and cell viability is necessary.

References:

- [1] Michael Perry, "High-Order Multiphoton Ionization of the Noble Gases", Ph.D Thesis, Lawrence Livermore National Laboratory-University of California, (1987).
- [2] Chris Xu and Watt W. Webb, "Measurement of two-photon excitation cross-sections of molecular fluorophores with data from 690 to 1050 nm", *J. Opt. Soc. Am. B*, **13**, 481-491, (1996).
- [3] J. Burris, T. J. McIlrath, "Theoretical study relating the two-photon absorption cross-section to the susceptibility controlling four-wave mixing", *J. Opt. Soc. Am. B*, **2**, 1313-1317, (1985).
- [4] C. C. Wang, *Phys. Rev.*, **152**, 146, (1966).
- [5] Nicholas Billinton and Andrew W. Knight, "Seeing the Wood through the Trees: A Review of Techniques for Distinguishing Green Fluorescent Protein from Endogenous Autofluorescence", *Analytical Biochemistry*, **291**, 175-197, (2001).
- [6] R. Swaminathan, C. P. Hoang and A. S. Verkman, *Biophys. J.*, **72**, 1900-1907, (1997).
- [7] http://biomicroscopy.bu.edu/r_nonlinear.htm.
- [8] Mohler W. A. , Simske J. S., Williams-Masson E. M., Hardin J. D., and White J. G., "Dynamics and ultrastructure of developmental cell fusions in the *Caenorhabditis elegans* hypodermis", *Cur. Biol.*, **8**, 1087-1090, (1998).
- [9] W. A. Mohler, J. G. White, "Stereo-4-D reconstruction and animation from living fluorescent specimens", *Biotechniques*, **24**, 1006-1010, (1998).
- [10] S. M. Keyse, R. M. Tyrell, "Induction of the heme oxygenase gene in human skin fibroblasts by hydrogen peroxide and UVA (365 nm) radiation: evidence for the involvement of the hydroxyl radical", *Carcinogenesis*, **11**, 787-791, (1990).
- [11] R. M. Tyrell, S. M. Keyse, "New trends in photobiology. The interaction of UVA radiation with cultured cells", *J. Photochem. Photobiol. B*, **4**, 349-361, (1990).
- [12] Philip E. Hockberger, Timothy A. Skimina, Victoria E. Centonze, Colleen Lavin, Su Chu, Soheil Dadras, Janardan K. Reddy, and John G. White, "Activation of flavin-containing oxidases underlies light-induced production of H₂O₂ in mammalian cells", *Proc. Natl. Acad. Sci. USA*, **96**, 6255-6260, (1999).
- [13] M. Born and E. Wolf, "Principles of Optics", 6th ed: Cambridge University Press, (1980).
- [14] W. Liptay, "Excited States", 1, N.Y.: Academic Press, (1974).
- [15] P. N. Butcher and D. Cotter, "The elements of nonlinear optics", 9: Cambridge University Press, (1990).

- [16] L. Moreaux, O. Sandre, J. Mertz, “Membrane imaging by second-harmonic generation microscopy”, *J. Opt. Soc. Am. B.*, **17**, 1685-1694, (2000).
- [17] N. Bloembergen, “Nonlinear Optics”, World Scientific, (1965).
- [18] J. I. Dadap, Shan, K. B. Eisenthal, and T. F. Heinz, “Second-harmonic Rayleigh scattering from a sphere of centrosymmetric material”, *Phys. Rev. Lett.*, **83**, 4045-4048, (1999).
- [19] R. Gauderon, P. B. Lukins, C.J.R. Sheppard, “Optimization of second-harmonic generation microscopy”, *Micron*, **32**, 691-700, (2001).
- [20] E. Georgiou, T. Theodossiou, V. Hovhannisva, K. Politopoulos, G. S. Rapti, D. Yova, “Second and third optical harmonic generation in type I collagen, by nanosecond laser irradiation, over a broad spectral region”, *Opt. Commun.*, **176**, 253-260, (2000).
- [21] S. Roth, I. Freund, “Optical second-harmonic scattering in rat-tail tendon”, *Biopolymers*, **20**, 1271-1290, (1981).
- [22] Guy Cox, Eleanor Kable, Allan Jones, Ian Fraser, Frank Maconi, and Mark D. Gorrel, “3-Dimensional imaging of collagen using second harmonic generation”, *J. of Struct. Biol.*, **141**, 53-62, (2003).
- [23] William Mohler, Andrew C. Millard, and J. Campagnola, “Second harmonic generation imaging of endogenous structural proteins”, *Methods*, **29**, 97-109, (2003).
- [24] Paul J. Campagnola, Andrew C. Millard, Mark Terasaki, Pamela E. Hoppe, Christian J. Malone, and William A. Mohler, “Three-Dimensional High-Resolution Second-Harmonic Generation Imaging of Endogenous Structural Proteins in Biological Tissues”, *Biophys. J.*, **81**, 493-508, (2002).
- [25] L. Cassimeris, S. Inoue, E. D. Salmon, Cell Motil, “Microtubule dynamics in the chromosomal spindle fiber: analysis by fluorescence and high resolution polarization microscopy”, *Cell Motil, Cytoskeleton*, **10**, 185-196, (1988).
- [26] Chi-Kuang Sun, Shi-Wei Chu, Szu-Yu Chen, Tsung-Han Tsai, Tzu-Ming Liu, Chung-Yung Lin and Huai-Jen Tsai, “Higher harmonic generation microscopy for developmental biology”, *Journal of Structural Biology*, 147, 19-30 (2004)
- [27] M.Muller, J.Squier, K.R.Wilson & G. J. Brakenhoff, “3D microscopy of transparent objects using third-harmonic generation”, *Journal of Microscopy*, Vol.191, p:266-274 (1998) Y.Barad, H.Eisenberg, M.Horowitz and Y.Silberberg, “Nonlinear scanning laser microscopy by third harmonic generation”, *American Institute of Physics* (1997).
- [28] Nonlinear scanning laser microscopy by THG. Y. Barad, H. Eisenberg, M. Horowitz, and Y. Silberberg *Department of Physics of Complex Systems, The Weizmann Institute of Science, Rehovot 76100, Israel.*

- [29] Higher harmonic generation microscopy for developmental biology. Chi-Kuang Sun, Shi-Wei Chu, a Szu-Yu Chen, Tsung-Han Tsai, Tzu-Ming Liu, Chung-Yung Lin and Huai-Jen Tsai.
- [30] Enhancement of third-harmonic generation in absorbing media APPLIED PHYSICS LETTERS VOLUME 81, NUMBER 20, S. Matsumoto, Y. Nabekawa, and K. Midorikawa.
- [31] Barad et al(1997)& Boyd(1992)
- [32] A. Sievers, B. Buchen, D. Hodick, “Gravity sensing in tip-growing cells,” Trends in Plant Sci. **1**, 273-279 (1996).
- [33] Michiel Muller & G.J.Brakenhoff, J.Squier, K.R.Wilson, “Third harmonic generation microscopy”.
- [34] S. Brenner, “The genetics of *Caenorhabditis elegans*”, *Genetics*, **77**, 71-94, (1974).
- [35] J.G. White, E. Southgate, J.N. Thomson, S. Brenner, “The structure of the nervous system of *Caenorhabditis elegans*” R. Soc. London B: Biol. Sci., 314, 1–340 (1996).
- [36] M. Chalfie, *Photochem. Photobiol.* **62**, 651-656, (1995).
- [37] F. Yang, L. G. Moss, G. N. Jr. Phillips, *Nature Biotech.*, **14**, 1246-1251, (1996).
- [38] Mats Ormö, Andrew B. Cubitt, Karen Kallio, Larry A. Gross, Roger Y. Tsien, and S. James Remington, *Science*, **273**, 1392-1395, (1996).
- [39] Roger Y. Tsien, “The Green Fluorescent Protein”, *Annu. Rev. Biochem.*, **67**, 509-544, (1998).
- [40] Artium Khachatourians, Aaron Lewis, Zvi Rothman, Leslie Loew, and Millet Treinin, “GFP Is a Selective Non-Linear Optical Sensor of Electrophysiological Processes in *Caenorhabditis elegans*”, *Biophysical Journal*, **79**, 2345-2352, (2000).
- [41] Biochemistry, mutagenesis, and oligomerization of DsRed, a red fluorescent protein from coral. Geoffrey S. Baird , David A. Zacharias , and Roger Y. Tsien.
- [42] <http://www.olympusconfocal.com/applications/fpcolorpalette.html>.
- [43] The structural basis for red fluorescence in the tetrameric GFP homolog DsRed Mark A. Wall, Michael Socolich & Rama Ranganathan). (*Nature Structural Biology* **7**, 1133 – 1138 (2000).
- [44] <http://www.microscopyu.com/articles/livecellimaging/fpintro.html>

- [45] D. Debarre, W. Supatto, A.M. Pena, A. Fabre, T. Tordjmann, L. Combettes, M.C. Schanne-Klein, E. Beaurepaire, "Imaging lipid bodies in cells and tissues using third-harmonic generation microscopy" *Nature Methods*, 3 47-53 (2006)
- [46] S. V. Plotnikov, A. C. Millard, P. J. Campagnola, and W. A. Mohler, "Characterization of the myosin-based source for second-harmonic generation from muscle sarcomeres," *Biophys. J.* 90, 693-703 (2006).
- [47] A. C. Millard, P. W. Wiseman, D. N. Fittinghoff, K. R. Wilson, J. A. Squier, M. Muller "Third-harmonic generation microscopy by use of a compact, femtosecond fiber laser source", *App. Optics*, 38, 7393-7397 (1999)
- [48] G. Filippidis, C. Kouloumentas, G. Voglis, F. Zacharopoulou, T. G. Papazoglou, N. Tavernarakis "Imaging of *Caenorhabditis elegans* neurons by Second Harmonic Generation and Two-Photon Excitation Fluorescence." *J. Of Biom. Optics*, 10, 024015 (2005)
- [49] P. J. Campagnola, L. M. Loew, "Second-harmonic imaging microscopy for visualizing biomolecular arrays in cells, tissues and organisms", *Nature Biotechnology*, 21, 1356-1360, (2003).
- [50] D. A. Dombeck, M. Blanchard-Desce, W. W. Webb "Optical recording of action potentials with Second-Harmonic generation microscopy", *J. of Neuroscience*, 24 999-1003 (2004).
- [51] <http://www-celanphy.sci.kun.nl/jenks.htm>
- [52] J. Burris, Ph. D., dissertation (Department of Physics, University of Maryland, College Park, Md., 1982)
- [53] O. Shimomura, F. H. Johnson, Y. Saiga, "Extraction, purification and properties of aequorin, a bioluminescent protein from the luminous hydromedusan, *Aequorea*", *J. Cell Comp. Physiol.*, **59**, 223-239, (1962).
- [54] Neurodegenerative conditions associated with ageing: a molecular interplay? Kostoula Troulinaki, Nektarios Tavernarakis. Institute of Molecular Biology and Biotechnology, Foundation for Research and Technology, Vassilika Vouton, Available online 20 October 2004)
- [55] <http://alzheimersolutions.stores.yahoo.net/geneticfactors.html#app>

- [56] Transgenic *C. elegans* as a Model in Alzheimer's Research
Yanjue Wu and Yuan Luo, *Laboratory of cellular and Molecular Neuroscience, Department of Biological Sciences, The University of Southern Mississippi, Hattiesburg, MS 39406, USA*)
- [57] eIF4E function in somatic cells modulates ageing in *Caenorhabditis elegans*
Popi Syntichaki, Kostoula Troulinaki & Nektarios Tavernarakis
- [58] *Caenorhabditis elegans* as a model system for Parkinson's disease. Schmidt E, Seifert M, Baumeister R.
- [59] *C. Elegans 2*: Donald L.Riddle, Thomas Blumenthal, Barbara J.Meyer, James R.Priess
- [60] (8.M. Müller, J. Squier, R. Wolleschensky, U. Simon, G. J. Brakenhoff, "Dispersion pre- compensation of 15 femtosecond optical pulses for high-numerical-aperture objectives," *J. Microsc.* **191**, 141-150 (1998).)
- [61] Principles of two-photon excitation fluorescence microscopy and other nonlinear imaging approaches. Martin Oheim, Darren J. Michael, Matthias Geisbauer, Dorte Madsen, Robert H. Chow.
- [62] *In vivo* imaging of anatomical features of the nematode *Caenorhabditis elegans* using non-linear (TPEF-SHG-THG) microscopy.
E. J. Gualda, G. Filippidis, G. Voglis, M. Maria, C. Fotakis and N. Tavernarakis
- [63] *In vivo* imaging of cellular structures in *Caenorhabditis elegans* by combined TPEF, SHG and THG microscopy (**SPIE** July2007)
E. J. Gualda, G. Filippidis, G. Voglis, M. Mari, C. Fotakis and N. Tavernarakis
- [64] 3D microscopy of transparent objects using third-harmonic generation.
M.Müller, J.Squier, K.R.Wilson&G.J.Brakenhoff
- [65] Third Harmonic microscopy with a titanium- sapphire laser.
D. yelin, D. oron, E. korkotian, M. segal, Y. Silberberg.
- [66] Multiphoton laser scanning microscopy for four-dimensional analysis of *Caenorhabditis elegans* embryonic development.
William A. Mohler, John G.White
- [67] Multimodal nonlinear spectral microscopy based on a femtosecond Cr:forsterite laser
Shi-Wei Chu, I-Hsiu Chen, Tzu-Ming Liu, Ping Chin Chen, and Chi-Kuang Sun, Bai-Ling Lin.